Dissertation

VTT PUBLICATIONS 772

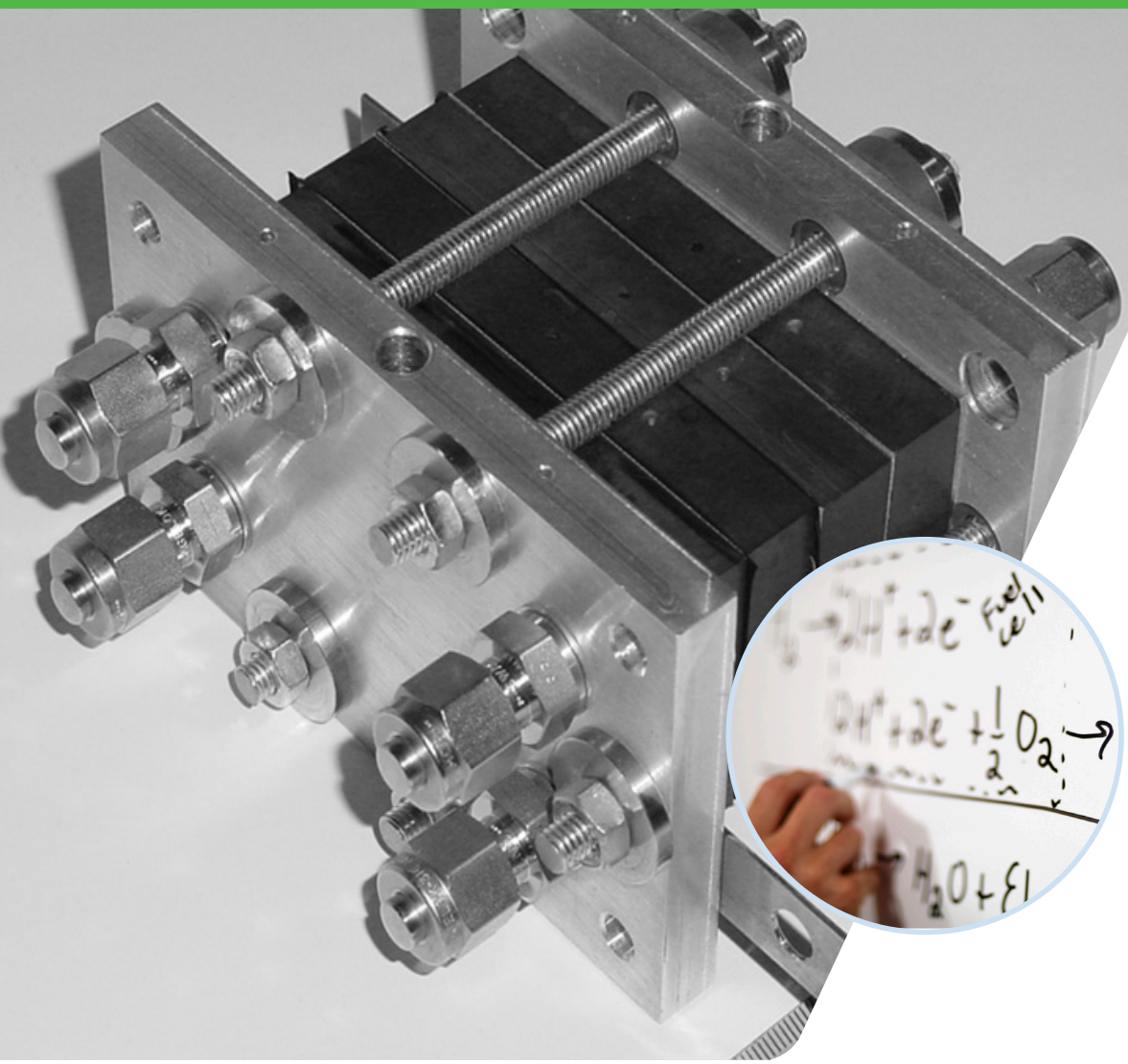

Suvi Karvonen

Modelling approaches to mass transfer and compression effects in polymer electrolyte fuel cells

VTT PUBLICATIONS 772

Modelling approaches to mass transfer and compression effects in polymer electrolyte fuel cells

Suvi Karvonen

Doctoral dissertation for the degree of Doctor of Science in Technology (Doctor of Philosophy) to be presented with due permission of the School of Science for public examination and debate in Auditorium K216 (Otakaari 4) at the Aalto University School of Science (Espoo, Finland) on the 25th of November 2011 at 12 noon.

ISBN 978-951-38-7754-5 (soft back ed.)
ISSN 1235-0621 (soft back ed.)

ISBN 978-951-38-7755-2 (URL: http://www.vtt.fi/publications/index.jsp)
ISSN 1455-0849 (URL: http://www.vtt.fi/publications/index.jsp)

JULKAISIJA – UTGIVARE – PUBLISHER

VTT, Vuorimiehentie 5, PL 1000, 02044 VTT
puh. vaihde 020 722 111, faksi 020 722 4374

VTT, Bergsmansvägen 5, PB 1000, 02044 VTT
tel. växel 020 722 111, fax 020 722 4374

VTT Technical Research Centre of Finland, Vuorimiehentie 5, P.O. Box 1000, FI-02044 VTT, Finland
phone internat. +358 20 722 111, fax + 358 20 722 4374

Kopijyvä Oy, Kuopio 2011

Suvi Karvonen. Modelling approaches to mass transfer and compression effects in polymer electrolyte fuel cells [Polymeerielektrolyyttipolttokennojen massansiirron ja puristuspaineen vaikutusten mallintaminen]. Espoo 2011. VTT Publications 772. 73 p. + app. 66 p.

Keywords PEMFC, fuel cell, modelling

Abstract

The subject of this thesis is modelling polymer electrolyte membrane fuel cells (PEMFCs) locally and on a cell scale. The modelling was done using software based on the finite element method and focused on mass transfer issues and compression pressure distribution and its effects on local phenomena.

Mass transfer, more specifically the flow distribution in the flow field system, was studied on the cathode. The velocity distribution was improved by changing the geometry of the channel system. This improvement was also observed experimentally. Mass transport problems of free-breathing fuel cells were also studied. These cells rely on free convection to provide reactants and remove reaction products. In this thesis, the aim was to develop an accurate model that is also computationally light.

The compression distribution in a stack was modelled based on an existing stack design. The results showed poor internal pressure distribution, with most of the cell experiencing insufficient compression. The modelling was then used to find a better end plate structure and suitable torques for the nut and bolt assemblies. The results were validated experimentally.

The effect of compression was studied on a local scale on which compression variations caused by the channel structure had been seen to affect the gas diffusion layer properties and contact resistances between components. According to the modelling results, there are strong local transversal electric currents in the cell. This phenomenon can affect the cell performance and lifetime negatively.

Suvi Karvonen .Modelling approaches to mass transfer and compression effects in polymer electrolyte fuel cells [Polymeerielektrolyyttipolttokennojen massansiirron ja puristuspaineen vaikutusten mallintaminen]. Espoo 2011. VTT Publications 772. 73 s. + liitt. 66 s.

Avainsanat PEMFC, fuel cell, modelling

Tiivistelmä

Väitöskirja käsittelee polymeerielektrolyyttipolttokennon (PEMFC) toiminnan mallinnusta paikallisesti ja kennotasolla. Tutkimuksen työkaluna käytettiin mallinnusta elementtimenetelmään perustuvalla ohjelmistolla. Mallinnuksen painopisteinä olivat erityisesti aineensiirron ongelmat ja puristuspaineen jakautuminen ja vaikutus kennon paikalliseen toimintaan.

Aineensiirtoa eli virtauskanaviston toimintaa tarkasteltiin kennon katodilla mallintamalla kanavistoon syntyvää virtausprofiilia. Kanaviston geometriaa muuttamalla pystyttiin parantamaan virtausprofiilia, ja tämä mallinnuksen avulla suoritettu optimointi havaittiin myös kokeellisesti. Aineensiirron kysymyksiä tutkittiin myös vapaasti hengittävien polttokennojen kohdalla. Näissä kennoissa aineensiirto perustuu vapaaseen konvektioon. Työssä pyrittiin kehittämään yhtä aikaa luotettava ja laskennallisesti kevyt malli. Lopputuloksena syntyi kolmiulotteinen malli vapaasti hengittävästä kennosta, jolla tutkittiin kennon koon ja asennon vaikutusta toimintaan.

Kennostossa vallitsevaa puristuspainetta mallinnettiin olemassa olevaan kennostoon perustuvan mekaanisen mallin avulla. Tuloksena saatiin epätasainen painejakauma. Mallinnuksen avulla etsittiin parempi rakenne kennoston päätylevyille sekä muutettiin pulttien vääntömomentteja, jolloin kennolla vallitseva painejakauma saatiin pysymään toivotuissa rajoissa. Samalla päätylevyn painoa saatiin vähennettyä. Tulokset verifioitiin kokeellisesti.

Puristuspaineen vaikutusta tutkittiin paikallisella tasolla, jossa virtauskanaviston rakenteen aiheuttamien painevaihteluiden oli todettu vaikuttavan merkittävästi kaasudiffuusiokerrosten ominaisuuksiin ja komponenttien välisiin resistansseihin. Mallinnuksen tulosten mukaan kennossa syntyy paikallisesti merkittävästi poikittaissuuntaista sähkövirtaa, joka aiheuttaa virrantiheyteen vaihteluja. Ilmiö voi vaikuttaa negatiivisesti kennon toimintaan ja elinikään.

Preface

This thesis was written in the Applied Physics department of the Helsinki University of Technology, in the New Energy Sciences Group, supervised by Professor Peter Lund. However, at the time of publication, this university has ceased to exist and is now a part of Aalto University.

The majority of funding came from the National Technology Agency of Finland (Tekes), the Wihuri Foundation and the National Graduate School for Energy Technology, all of which I thank for their support.

I want to thank all the people I had the pleasure to work with, especially Tero Hottinen, Mikko Mikkola, Olli Himanen and Iwao Nitta. The work you did gave me the basis to build on. The fuel cell group had some great people in it, and I enjoyed working with all of you.

Thank you to my friends, for our teamwork throughout student times, for keeping me sane and in touch with other people during the baby year and for easing my return to work. You were surely the best support group ever.

My thanks to family: my husband, who put up with me not having a real job, so to say, for the years of making this thesis and never would have even thought to complain. My parents, who made sure I had everything I needed when it was time to choose what I wanted to do with my life. And finally, my son, who is the most important thing to come out of these years of my life. Maybe one day you will read this and know better than we now do what became of fuel cells.

Contents

List of Publications

1. **Modeling of flow field in polymer electrolyte membrane fuel cell**
   Karvonen, S., Hottinen, T., Saarinen, J., Himanen, O.
   Journal of Power Sources 161(2), pp. 876–884 (2006)

2. **Inhomogeneous compression of PEMFC gas diffusion layer. Part II. Modeling the effect**
   Hottinen, T., Himanen, O., Karvonen, S., Nitta, I.
   Journal of Power Sources 171(1), pp. 113–121 (2007)

3. **Modelling the effect of inhomogeneous compression of GDL on local transport phenomena in a PEM fuel cell**
   Nitta, I., Karvonen, S., Himanen, O., Mikkola, M.
   Fuel Cells 8(6), pp. 410–421 (2008)

4. **Modeling of polymer electrolyte membrane fuel stack end plates**
   Karvonen, S., Hottinen, T., Ihonen, J., Uusalo, H.
   Journal of Fuel Cell Science and Technology 5(4), art. no. 041009-1 (2008)

5. **Modeling free convective mass and heat transfer in fuel cells**
   Karvonen, S. Submitted to Journal of Fuel Cell Science and Technology (2011)

Author's Contributions

For Publication 1, the author was mainly responsible for building the model, conducting the experiments, analysing the data and writing the article.

For Publication 2, the author participated in the modelling and made a minor contribution to writing the article.

For Publication 3, the author participated in building the model, analysing the data and writing the article.

For Publication 4, the author was mainly responsible for designing and building the model and analysing the modelling data. The author participated in planning the experimental part and analysed the experimental results. The author was mainly responsible for writing the article.

For Publication 5, the author was mainly responsible for designing and building the model as well as analysing the data and writing the article.

List of Symbols

Symbol	Quantity	value/unit
A	area	m^2
c	concentration	mol/m^3
c_p	thermal capacity	J/kgK
D	binary diffusion coefficient	m^2/s
$\tilde{D}$	Maxwell–Stefan diffusion coefficient	m^2/s
E	energy	J
E_{theor}	theoretical fuel cell open circuit voltage	V
F	Faraday constant	96485 C/mol
$\mathbf{g}$	gravity vector	m/s^2
G	Gibbs' energy	J/mol
H	enthalpy	J/mol
$\mathbf{i}$	unit vector, x-direction	-
$\mathbf{J}$	molar flux vector	mol/m^2s
$\mathbf{j}$	unit vector, y-direction	-
j	current density	A/m^2
$\mathbf{k}$	unit vector, z-direction	-
k	heat conductivity	J/m^2
M	molar mass	kg/mol
$\mathbf{n}$	normal vector	-
$\dot{\mathbf{N}}$	molar flux on electrode boundary	kg/m^2s
p	pressure	Pa
R	gas constant	8.314 J/molK
S	source term	-
$S_{a,c}$	entropy at cathode or anode	J/K
T	temperature	K
$\mathbf{t}$	tangential vector	-
q	thermal flux	W/m^2
$\mathbf{u}$	velocity vector	m/s
u	x-directional velocity	m/s
V	volume	m^3

v	y-directional velocity	m/s
w	z-directional velocity	m/s
x	molar fraction	-
z	number of electrons involved in a reaction	-

Greek symbols

α	reaction symmetry factor	-
γ	strain (tensor)	-
Δ	change	-
ε	porosity	-
η	dynamic viscosity	Pa s
η_{theor}	theoretical efficiency	-
κ	permeability	m^2
σ	electrical/ionic conductivity	Sm^{-1}
σ_{str}	stress (tensor)	Pa
φ, Φ	potential	V
ρ	density	kg/m^3
ω	mass fraction	-

Subscripts and superscripts

0	reference state
A	reducing component
B	oxidizing component
ch	channel system
CL	catalyst layer
con	mass conservation equation
D	Darcy's Law
eff	effective
GDL	gas diffusion layer
H2	hydrogen
H2O	water
i	species
m	ionic potential
mass	mass-averaged formation of Maxwell–Stefan equations

mem	membrane
molar	molar-averaged formation of Maxwell–Stefan equations
NS	Navier–Stokes equation
O2	oxygen
ref	reference concentration
s	electronic potential
theor	theoretical

Acronyms

1D	one-dimensional
2D	two-dimensional
3D	three-dimensional
AFC	alkali fuel cell
BP	bipolar plate
BMW	Bayerische Motoren Werke AG
CHP	combined heat and power production
DMFC	direct methanol fuel cell
FC	fuel cell
FEM	finite element method
GDL	gas diffusion layer
GE	General Electric
MCFC	molten carbonate fuel cell
NASA	National Aeronautics and Space Administration
PAFC	phosphoric acid fuel cell
PEMFC	polymer electrolyte membrane fuel cell
PEM	polymer electrolyte membrane
PFSA	perfluorosulfonic acid
SOFC	solid oxide fuel cell

1. Introduction

Energy production often has a negative impact on the environment. In historical times, small populations and the nature of the available energy sources ensured that energy production was sustainable or, at least, that any harmful effects such as deforestation were local, not global. However, with the rapidly increasing global population and improving standard of living, the problem of providing clean energy for everyone has become one of the main challenges of the 21st century. Currently, there does not appear to be any single solution that can be used universally to produce clean, inexpensive energy. Instead, we face multiple choices that all have their advantages and disadvantages.

One proposed solution to the problem of environmentally sustainable energy production is the so-called hydrogen economy in which one of the main energy carriers is hydrogen (as opposed to, e.g., oil and electricity). Hydrogen can be produced by various methods and used in, for example, fuel cells. The use of hydrogen production processes, which do not produce greenhouse gases, would, in theory, allow the hydrogen economy to function with a minimal negative effect on the climate. Moving to a hydrogen economy would be expensive, however, and require much political will and time. Several technical issues concerning hydrogen production, storage, delivery and use in fuel cells would also need to be solved before a hydrogen economy could be considered a realistic alternative. As a consequence of these difficulties, the hydrogen economy is currently a relatively utopian scenario that may never be realized. Hydrogen and fuel cells could be part of the solution, however, even if the road of the hydrogen economy is never taken.

A fuel cell is a device that produces electrical and thermal energy from various fuels such as hydrogen, methanol or natural gas. A fuel cell can convert the chemical energy of its fuel and oxidant into electricity without combustion or conversion through thermal energy, which, at least in theory, gives it high effi-

ciency. If hydrogen is used as the fuel, the only reaction product is water, so there are no harmful exhaust compounds, at least not on site. Fuel cells also have high power density, are silent, require little maintenance and, on a small power scale, usually have high efficiencies compared with many traditional technologies such as the internal combustion engine.

Different types of fuel cells are suitable for applications ranging from milliwatts to megawatts and from portable to stationary. The different types of fuel cells are usually categorized by their operating temperature or materials. Fuel cells can potentially be used in everything from portable electronics and automobiles to small-scale power plants. The fuel cell type of interest in this thesis is the polymer electrolyte membrane fuel cell (PEMFC), which is best suited to portable electronics, transportation and other small-scale applications.

Unlike internal combustion engines, fuel cells retain their good efficiency at partial loads. However, for each application, fuel cells must first be proven superior to existing technologies such as batteries, internal combustion engines and the electrical network. Fuel production, storage and distribution issues also have to be solved. Currently, fuel cell performance, life-time and price are not viable for anything but small niche applications, and wide-scale commercialization is yet to come.

In principle, fuel cell performance can be improved either by using new, superior materials and innovations or by improving the cell design and operational conditions. In the case of PEMFC materials, the research includes finding new electrolyte membranes that can operate at a higher temperature without the need for liquid water, researching catalysts in order to decrease price and increase efficiency and lifetime, improving gas diffusion layer properties and finding more corrosion-resistant materials for the support structures. Cell design can be improved by, for example, optimizing flow field geometry, improving the compression distribution in a stack or finding new, innovative solutions. Finding the optimal operating conditions, i.e., the temperature, current, gas flow stoichiometry, etc., is also crucial to cell performance.

The subject of this thesis consists of finding ways to improve the performance of the PEM fuel cell through modelling. Many fuel cell phenomena are difficult or almost impossible to experiment on and cannot be deduced from the overall cell performance. In these cases, modelling is an invaluable tool. Modelling can also speed up the process of improving cell design, as simulation is often less expensive and less time-consuming than experimentation. In this thesis, modelling is used for studying cell phenomena and for improving cell design. The

results provide new insight into local phenomena and demonstrate that certain changes in design parameters can improve cell performance significantly.

The distribution of reactants on a fuel cell cathode is studied in Publication 1 and discussed in Chapter 4. This study focused on the geometrical design of the flow field plate structure and demonstrated that small changes in geometry can improve flow distribution significantly, i.e., make it more even in the cell. This is important in terms of overall cell performance, as an uneven flow distribution will cause problems such as reactant starvation and accumulation of liquid water in the cell. Modelling is a natural way to approach a problem for which in-situ experiments, though possible, are complicated and time-consuming. The modelling results obtained in Publication 1 were verified experimentally and are in agreement on a qualitative level.

Publications 2 and 3 focus on the local phenomena caused by uneven compression in the cell. A fuel cell is usually compressed by a nut and bolt assembly so that the cell does not leak gases and the components have good electrical contact. The pressure deforms the soft gas diffusion layers used in fuel cells, however, crushing their pores, and excessive compression thus leads to mass transport problems. Furthermore, the internal structure of a PEMFC, i.e., the channel system of the bipolar plates, leads to large local variations in compression pressure as there is practically no compression on the gas diffusion layers underneath the channels. This causes large variations in many key parameters such as the electronic conductivity, the mass transport properties of the gas diffusion layers and the contact resistance between different components. This phenomenon has been largely neglected in previous studies.

A basic model for studying the effects of uneven compression was developed in Publication 2. The results showed that local effects are significant, especially in terms of current density. Some of the parameters used were inaccurate however. These parameters were studied experimentally in order to improve the reliability of the model. The new improved model was reported in Publication 3. The results show that due to uneven compression and thus varying contact resistances and uneven deformation of the gas diffusion layer, the current density in the electrodes has a large transversal component and a local maximum. In earlier modelling studies, the compression effects were excluded and the current was mostly seen to travel straight from the electrodes to the current collectors. The local variations discovered here are significant as they can have a negative effect on the overall performance as well as the lifetime of the cell.

Publication 4 focuses on studying the compression in the cells on a larger scale. The pressure distribution in a stack was studied by making a mechanical model of an existing PEMFC stack. The results showed that the pressure on the gas diffusion layers of the individual cells was far from in the optimal range. The model was then used to find an improved end plate structure that was both lighter and more rigid than the original in order to improve the internal pressure distribution. The torque on the nut and bolt assemblies was also optimized. As a result of these changes, it was possible to limit the internal pressure in the cell to an optimal range. The modelling results were validated experimentally on a qualitative level.

Publication 5 focuses on the mass transfer of a free-breathing fuel cell, i.e., a fuel cell that relies on natural convection instead of auxiliary equipment such as pumps to take care of its mass transport. The model built in this study focused on the cathode and its surrounding air zone. 2D and 3D models were used to find the best way to model the problem accurately and with computational efficiency. The resulting model was then used to study the performance of a small, free breathing fuel cell. The results show, e.g., that the tilt angle of the cell has a large impact on the performance.

The subjects of these studies thus cover cell and local-scale phenomena, mass transport issues and compression effects. The uniting factor is the aim to gain a better understanding of the way PEMFC operates beyond a few variables like current and voltage, which are easily measured externally but do not say much about the complex phenomena occurring internally. The modelling has much room for improvement in future work, as PEMFC operation is based on many different, interdependent and complicated phenomena for which the correct parameters and correlations are often not well known. Nevertheless, the modelling in this study has offered new scientific information on various cell phenomena, and the models can be used as tools to optimize cell performance.

2. Fuel Cells

2.1 History

Fuel cells are often thought of as modern technology that is not yet ready for commercialization. The concept of the fuel cell dates back to 1838–1839 when Christian Schönbein published the principle of the fuel cell [1]. In 1845, the first functional fuel cell was built by Sir William Grove [2]. At the time, not much practical value was attached to this phenomenon and fuel cell development did not advance for decades.

The term “fuel cell” was first proposed by Ludwig Mond and Charles Langer, who built a fuel cell operating on air and industrial coal gas in 1889 [3]. After Mond and Langer, no significant advancement was made before the 1950s, when Francis T. Bacon and his group replaced the previously used platinum electrodes and acid bath electrolyte with less expensive nickel electrodes and alkaline electrolyte. After almost twenty years of research, Bacon developed a five kilowatt fuel cell [4]. In the 1950s, fuel cells were also being developed at the General Electric (GE) Company. The results achieved by Bacon and GE showed that fuel cells, although expensive, were not limited to the laboratory but had potential for real applications. GE was also the company that built the first polymer electrolyte membrane fuel cells in the 1960s [5]. Not surprisingly, the first instance of adoption of the new technology was by the National Aeronautics and Space Administration (NASA), whose spacecraft required a source of electricity [6]. Nuclear power was considered too hazardous while a combination of solar power and batteries would have been too bulky. As a consequence, fuel cells were used in the Gemini, Apollo and Space Shuttle missions. During this time, fuel cells were considered for many different applications, an example of which is the Allis-Chalmers fuel cell tractor in Figure 1.

Figure 1. An experimental Allis-Chalmers fuel cell tractor in 1959 [7].

For the past few decades, increasing awareness of the limited fossil fuel resources and the environmental effects of their use have given ample motivation for research into new energy technologies, one of which is fuel cell technology. Consequently, during the last twenty years, fuel cell research has boomed. This is partly due to the development of new materials that were not available earlier, such as improved electrode materials.

Traditionally, the greatest interest in fuel cell technology has perhaps come from the automotive industry, though fuel cells can also be used in portable electronics and for stationary power production. In transportation, the first demonstration fuel cell bus was built by Ballard in 1993, after which demonstration fuel cell buses have been in use in many cities. Demonstration fuel cell cars by companies such as Ford, Toyota and BMW have been presented since the late 1990s. Demonstration projects are still going on, and a fuel cell bus fleet of 20 buses was operational during and after the 2010 Winter Olympics [8].

On a smaller scale, fuel cells can be used in portable applications such as laptops and cell phones. These devices require increasing amounts of power, and providing this for long periods is challenging with current battery technologies. The operating conditions in these applications vary greatly, as does the size of the fuel cell system, and the auxiliary equipment, in particular, has to be minimized. One candidate for these systems is a so-called free-breathing fuel cell that takes its oxygen from the surrounding air through passive mechanisms.

Current fuel cell research aims to lower the cost and improve the performance and lifetime of the cells, thus making fuel cells a viable alternative to competing technologies. The European Union has a programme called the Fuel Cells and Hydrogen Joint Technology Initiative. The strategic research agenda, written in 2005, cites 4000 €/kW as the current price and 100 €/kW as the goal price for FC systems in transportation [9].

2.2 Basics of Fuel Cells

A fuel cell is an electrochemical apparatus that uses the chemical energy of its fuel and oxidant. There is no combustion in the process. The advantage over internal combustion engines is that the efficiency of the fuel cell is not bound by Carnot efficiency. This conversion is accomplished by separating the fuel and oxidant by an electrically insulating but ionically conductive electrolyte. Fuel is fed to the anode and oxidant to the cathode. The fuel, driven by the chemical potential, is oxidized on the anode, while the oxidant is reduced on the cathode. The resulting ions pass through the electrolyte from the cathode to the anode or vice versa depending on the fuel cell type. The electrons travel via an external circuit, thus producing electric current that can be used as desired.

Fuel cells are typically categorized according to the electrolyte material, though some cell types are named after their fuel. In general, fuel cells can be divided into two main categories: high or intermediate temperature cells, such as the Solid Oxide Fuel Cell (SOFC), and low temperature cells, such as the Polymer Electrolyte Membrane Fuel Cell (PEMFC). Potential fuels include, e.g., hydrogen, methanol and methane, and the range of suitable fuels depends on the cell type. In general, high temperature fuel cells can use a wider range of fuels, especially hydrocarbons, than low temperature fuel cells. The oxidant is oxygen, either as a pure gas or obtained from the air. The basic structure of the cell is independent of the cell type and consists of two electrodes separated by an electrolyte layer. The most common electrolyte materials are polymer membranes with sulfonic acid groups, ceramic materials, acids and molten salts. The most common fuel cell types and their characteristics are listed in Table 1.

High temperature cells are suitable for stationary power production and operate at 700–900 °C. Intermediate temperature SOFCs that operate at 500–700 °C are also being researched. Low temperature FCs such as PEMFCs operate in the temperature range of liquid water and can be employed in a variety of applications from portable electronics to transportation, small-scale residential heat and

power production and many niche applications [2]. In recent years, the lines have become blurred, however, as low temperature SOFCs (500–700 °C) and high temperature PEMFCs (over 100 °C) have been researched. The ultimate goal of fuel cell technology, the fuel cell car, would probably employ a PEMFC, although there has also been research into SOFCs.

Table 1. Fuel cell types, their operating temperatures and electrolyte materials.

Fuel cell type	**Abbreviation**	**Operating temperature**	**Electrolyte material**
Polymer Electrolyte Membrane	PEMFC	20–90 °C	Proton-conducting polymer film
Direct Methanol	DMFC	20–90 °C	Proton-conducting polymer film
Alkaline	AFC	100–250 °C	OH^--conducting alkaline solution
Phosphoric Acid	PAFC	200 °C	Proton-conducting phosphoric acid
Solid Oxide	SOFC	700–1100 °C	O^{2-}-conducting ceramic oxide[1]
Molten carbonate	MCFC	600–700 °C	CO_3^{2-}-conducting molten carbonate

For portable applications, the main competition is batteries, whose efficiency is very high and price low. Despite rapid improvement, the energy storage capacity of batteries is not sufficiently high for many applications. Laptops, in particular, are seen as a potential application for fuel cells, as their batteries can currently only provide energy for a few hours of use, and the power consumption of these devices is continually increasing. With fuel cells, this period could perhaps be extended as the energy capacity would depend only on the size of the fuel supply not the cells themselves. In a fuel cell, the power and energy capacities can be sized separately whereas in batteries they are interdependent. A fuel cell laptop does not require recharging, though it does need refuelling. If it is necessary to use a laptop for a long period with no external source of electricity, it is easy to have several fuel containers ready.

In transportation, the competing technologies are the traditional internal combustion engine running on ever-decreasing reservoirs of fossil fuels (or biofuels) and the yet to be commercialized electric car running on batteries. Fuel cells

[1] There are also some ceramic materials that exhibit proton conductivity, see, e.g. [10].

would be ideal for transportation applications, but the necessary fuel distribution infrastructure does not yet exist. The operating conditions are also harsh on the cells, for instance, the ambient temperature can be as low as -30 °C. In a true hydrogen economy, fuel cells could also be used to produce combined heat and power (CHP) for distributed energy production. On a smaller scale, fuel cells could be used to produce CHP from natural gas at the end of a gas line, or using landfill gas or biogas.

Currently, fuel cells are mostly used for demonstrations and military applications. There are some niche applications for which fuel cells could be used in the near future however. These include telecommunications link stations and other off-grid applications. Ships and boats may benefit from a fuel cell system that produces electricity while the engines are off and the battery capacity is insufficient.

2.3 Polymer Electrolyte Membrane Fuel Cell

The PEMFC is a low temperature fuel cell that has a solid polymer membrane with sulfonic acid groups as an electrolyte. The PEM fuel cell uses hydrogen as fuel and oxygen (typically in the air) as the oxidant. The electrode and cell reactions are:

Anode: $H_2 \rightarrow 2H^+ + 2e^-$ (1)

Cathode: $\frac{1}{2}O_2 + 2H^+ \rightarrow H_2O$ (2)

Full cell: $H_2 + \frac{1}{2}O_2 \rightarrow H_2O$ (3)

Thus, in a PEMFC fuel cell, the only reaction product is water. Combined with its other attributes, low operating temperature, fast start-up and shutdown, high efficiency and the possibility of scaling the stack according to power requirements, the PEMFC is suitable for a wide range of applications.

The heart of each PEMFC is composed of the electrolyte, electrodes, gas diffusion layers and flow field plate. In a stack, i.e., multiple cells connected in series, the flow field plates of adjacent cells are typically combined and the result is known as a bipolar plate. The electrodes are usually coated on a polymer electrolyte film. This structure is known as the membrane electrode assembly (MEA). As a single cell usually gives a voltage of less than 1 V, it is usual to connect many cells in series to form a fuel cell stack. In addition to the cells themselves, stacks usually have components known as end plates, which provide

mechanical support for the cells. These components are described briefly in the following sections. It should be noted that in addition to these components, a fuel cell system also requires support structures such as gaskets, nuts and bolts, fuel and exhaust lines, flow controllers, electrical components, etc.

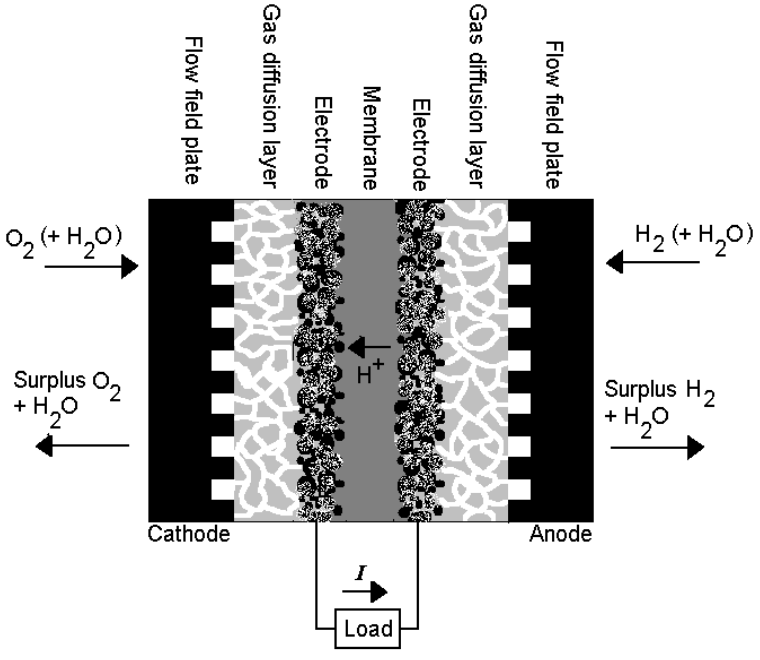

Figure 2. A schematic of a PEMFC. Picture is not to scale.

2.3.1 Membrane Electrode Assembly (MEA)

The most commonly used electrolyte of the PEMFCs is the Nafion® membrane, a solid ion-conducting perfluorosulfonic acid (PFSA) material. It consists of sulfonic acid groups attached to a polymer matrix, the former providing proton conduction and the latter structural support. There are many ion transport mechanisms through which the membrane conducts protons from the anode to the cathode and they are all dependent on the presence of water molecules in the membrane. Thus, a dry membrane does not conduct ions. The membrane drying out not only lowers the fuel cell performance but can also lead to actual membrane damage and thus to shorter lifetimes. The requirement for liquid water also limits the temperature range of the cell.

The electrodes are composed of carbon black, ion-conducting polymer and catalyst particles. The use of catalysts, usually platinum, is necessary in all low temperature cells, as the reaction kinetics in this temperature range are too slow to achieve good enough cell performance otherwise. The electrode is porous in order to maximize the amount of active surface area. Porosity is also required in order to provide transportation for the reactants and reaction products. The catalyst particles are very sensitive to many impurities in the air or fuel, especially sulphur and carbon monoxide, and usually degrade or agglomerate even in normal operation, thus lowering the cell lifetime.

The dependence on the presence of liquid water everywhere in the membrane is a challenge for mass transportation, as excess water tends to block oxygen transport to the reaction sites, thus reducing the cell reactions. This phenomenon is known as flooding. There is thus a fine balance between too much and too little water in the cell. Water management is one of the most important and challenging aspects of PEMFC operation. It has been studied by many groups, and a good review on this subject was published in, e.g., [11].

The lifetime and durability of the MEA have been studied by many groups, as MEAs have been observed to degrade relatively quickly. There are several mechanisms of MEA degradation, e.g., membrane thinning or cracking, contamination, electrode layer delamination and catalyst particle agglomeration, dissolution and migration as well as chemical reactions of the catalyst particles, see, e.g., [12–17]. These mechanisms may be enhanced by inadequate temperature or water management, impurities, severe operating conditions and voltage cycling, see, e.g., [18, 19]. Thus, it is crucial that the cell operating parameters and structures are designed so that these issues can be avoided as far as possible. Compression, flow and temperature distributions across the cell are not only important to the performance of the cell but also to its lifetime. Thus, the modelling of these issues, such as described later in this work, also has ramifications in terms of MEA durability and consequently cell lifetime.

2.3.2 Gas Diffusion Layers

Gas diffusion layers (GDLs) provide transportation for reactants and reaction products between the flow channels and MEA. They are also electrically conductive, provide mechanical support for the fragile MEA and have to be chemically inert in the fuel cell environment. GDLs have conflicting requirements for optimal performance: they have to be porous to allow for mass transport while at

the same time being mechanically durable and good electrical conductors. These properties also depend on the compression, as the soft porous material is deformed under mechanical stress. When a fuel cell is assembled, the GDL is compressed under the flow field plate ribs while the part under the channel remains almost uncompressed, leading to significant local variations in porosity and electrical conductivity.

GDLs also have to be able to transport water, i.e., the liquid water required in the MEA and created in the cathode reaction. GDLs are typically made of carbon paper or cloth, with a hydrophobic component such as polytetrafluoroethylene (PTFE, commonly known as Teflon®). It is also usual to add a so-called microporous layer of PTFE and carbon black on the electrode side of the GDL in order to improve its water transport properties, see, e.g., [20, 21].

2.3.3 Bipolar Plates

Bipolar plates envelop the GDLs and MEA. They are typically much thicker and mechanically more rigid than the thin GDL and MEA layers and thus constitute the mechanical support for the cell. Bipolar plates are good electrical conductors and are part of the route electrons travel on their way to the external circuit. They also have to be impermeable to gas. Bipolar plates are traditionally made of metal, typically stainless steel, or graphite. Of these, graphite has been widely used in laboratory experiments but is unsuitable for wide-scale commercialization because it is expensive and hard to machine or shape. Metal plates would otherwise be ideal due to their high conductivity, ready availability and ease of manufacturing, but in the corrosive fuel cell environment they do not remain chemically inert and the resulting dissolved particles can damage the MEA. Thus, alternative materials such as polymer composites, see, e.g., [22, 23], which will not corrode in the fuel cell environment and have the added advantage of being lighter than metal, have been studied by many groups. An alternative solution is to coat the metal with a thin corrosion-protective layer, see, e.g., [24–26].

Bipolar plates should have good electrical contact with the GDLs while also being able to transport the reactants and reaction products to and from the GDL. In order to accomplish this, the plates have channels grooved on their faces to direct the mass flows in the desired directions. The design of the channel system or flow field governs how the reactants are distributed on the GDLs and thus on the electrode surfaces, as well as affecting the removal of excess water from the cell.

As the channels may be set in any geometrical arrangement imaginable, there are various possible flow field configurations. It is also possible to fill the channels with porous media, partially or completely, in order to improve flow distribution and liquid water management, see, e.g., [27, 28]. Four different types or a combination of them are usually used in fuel cells: the parallel, serpentine, interdigitated and spiral flow fields, see, e.g., [29–31]. The width, depth and cross-sectional shape of the channels as well as the distance between two channels (a.k.a. land or rib width) are all adjustable and have a significant effect on the cell performance, see, e.g., [32–34]. Serpentine and spiral flow fields have long channels, which usually give a relatively even reactant distribution but cause a larger pressure drop thus requiring more from auxiliary equipment (pumps). The interdigitated flow field has short, discontinuous channels, which force the reactant flow into the GDL and cause a large pressure drop. Of these four alternative configurations, the parallel flow field is the only one that does not cause a large pressure drop across the cell. If, however, the flow field design is not planned with care, the resulting flow distribution can be very uneven. This has caused many to dismiss the parallel flow field. An uneven flow distribution causes reactant starvation on some parts of the electrode, which decreases the overall performance of the cell. The flow distribution in a parallel flow field system and its optimization was studied in this thesis and is discussed in Chapter 4 and Publication 1.

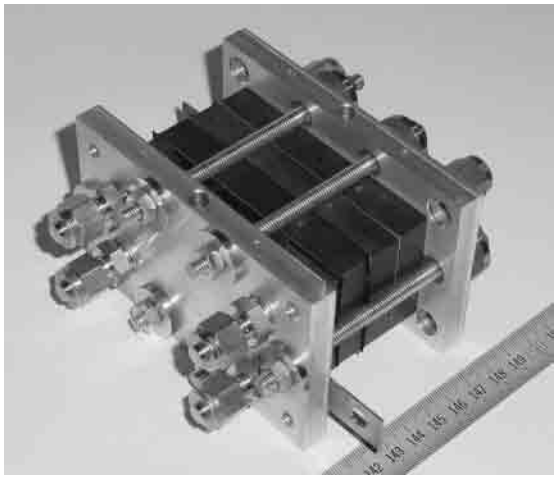

Figure 3. A small PEMFC stack used in the Laboratory of Advanced Energy Systems in ca. 2001 (Photo courtesy of Mikko Mikkola).

2.4 Free-Breathing Fuel Cells

It is possible to build a fuel cell that takes its required oxygen from ambient air without auxiliary equipment. This kind of fuel cell is known as a free-breathing fuel cell. It relies on the temperature difference between the cell and ambient air created by the heat produced in the cell operation to drive oxygen to the cell by natural convection. Free-breathing fuel cells are typically suited to small-scale applications requiring little power such as transportable electronics. They need less auxiliary equipment than fuel cells, depending on forced convection and so require less space and cost less.

The performance of a free-breathing fuel cell depends on the natural convection, which, in turn, is affected by the geometrical design, size and orientation of the fuel cell. The cathode usually requires a cover structure to avoid mechanical damage, the design of which is also important in terms of natural convection. The effectiveness of natural convection on the cathode of a free-breathing fuel cell has been studied in Publication 5 and is discussed in Chapter 7. The aim was to develop a model capable of describing this phenomenon and giving predictions on how the size and position of the cell affect its performance.

2.5 PEMFC Performance

The theoretical open circuit voltage E_{theor} of a PEMFC is calculated from the Gibbs energy ΔG of the chemical reaction of hydrogen and oxygen combining to produce water [2]:

$$E_{theor} = -\frac{\Delta G}{zF} \tag{4}$$

Here, z is the number of electrons that participate in the reaction, two in the case of the PEMFC. F is the Faraday constant that gives the magnitude of the electric charge per mole of electrons, approximately 96,485 C/mol. At 25 °C ΔG is -237.2 kJ/mol and the open circuit voltage of the cell is 1.23 V.

The open circuit voltage depends on the temperature of the cell as well as the partial pressures of the reactants. This correlation is given by the Nernst equation:

$$E = E_{theor} + \frac{RT}{zF} \ln\left(\frac{p_{H_2} p_{O_2}^{1/2}}{p_{H_2O}} \right) \tag{5}$$

Here, E is the open circuit voltage, R the universal gas constant, T the temperature and p_i the partial pressure of species i.

The theoretical maximum efficiency of a fuel cell can be calculated from

$$\eta_{theor} = \frac{\Delta G}{\Delta H} \tag{6}$$

where ΔH is the enthalpy of the cell reaction. At 25 °C ΔH = -285.84 kJ/mol. Thus, the theoretical maximum efficiency of a PEMFC is 83%. This efficiency is, of course, never reached as other factors such as the degree of fuel utilization and internal resistances affect the efficiency. However, the efficiency of a PEM fuel cell is usually in the range 30–60% [2].

In reality, due to impurities and hydrogen cross-over causing mixed potentials, the open circuit voltage is usually slightly lower than E, see, e.g., [35]. In an operating fuel cell, the voltage is lower still, as drawing current from the cell causes overpotentials to occur. There are three main loss mechanisms present in an operating fuel cell: the activation overpotential, ohmic losses and the diffusion overpotential. These loss mechanisms are discussed briefly in the following paragraphs.

The activation overpotential is determined by the cell reaction kinetics, especially the slow cathode reaction. The activation overpotential is typically the largest loss factor. It can be somewhat mitigated by using catalysts and raising the cell temperature. The activation overpotential is almost solely responsible for performance losses in low current densities.

Ohmic losses are caused by the resistance of the cell materials and contact resistances between the components to ionic (membrane) and electric (GDL, flow field plates, etc.) currents. The magnitude of ohmic losses is directly proportional to the amount of current drawn from the cell. Ohmic losses can be reduced by improving the electrical conductivity of the cell materials, especially the membrane, and ensuring good electrical contact between the cell components (especially the electrodes and the GDL, and the GLD and the flow field plates). The former depends on the materials used and the humidity of the membrane, while the latter also correlates to the compression directed at the cell or stack (discussed in more detail in Chapter 5). Ohmic losses determine the shape of the current-voltage curve in middle current densities.

The diffusion overpotential is caused by the mass transportation limitations. As an increasing amount of current is drawn from the cell, the reactant concentration becomes low at the electrodes and the reaction product water starts to

block the reaction sites. Thus, the diffusion overpotential is large at high current densities. It can be reduced by employing more powerful pumps, optimizing the channel system in the flow field plates and improving mass transfer in the GDLs (e.g., by making them more porous or hydrophobic).

In addition to these mechanisms, performance losses may be caused by impurities in the cell, either mixed in the air or fuel, or dissolved from the cell components; hydrogen leaking through the membrane in molecular form to the cathode, etc. When all these mechanisms are taken into account, the voltage of an operating fuel cell is typically around 0.6–0.7 V. Connecting multiple cells in series gives more practical voltages. It is of course possible to operate the cell at any voltage between the open circuit voltage and zero, but this does not usually give optimal power or efficiency.

The current density j of the cell and the overpotential φ correlate according to the following equation [2]:

$$j = j_0 \frac{c_A}{c_{A,ref}} \exp\left(-\frac{\alpha z F \varphi}{RT}\right) - j_0 \frac{c_B}{c_{B,ref}} \exp\left(\frac{(1-\alpha) z F \varphi}{RT}\right) \tag{7}$$

This equation applies to both electrodes. Here, j is the current density, φ the overpotential, c_A and $c_{A,ref}$ the concentration and reference concentration of the reducing component and c_B and $c_{B,ref}$ of the oxidating component. j_0 is the so-called exchange current density that represents the current at the open circuit voltage when no net current is drawn from the cell, and α is the reaction symmetry factor. A simplified form of this equation is known as the Butler-Volmer equation, and the name is often mistakenly applied when this equation is used.

3. PEMFC Modelling

A fundamental approach to developing any technology is to conduct experiments. Experimentation has some limitations, however, that often make studying a given aspect very difficult or even impossible. For example, local phenomena, i.e., small-scale differences in current density, are almost impossible to measure in any way but are important in terms of overall efficiency and cell lifetime. In general, it is easy to measure an IV-curve of a cell; it is much harder to ascertain which factors determined the shape of that curve and how. Modelling can also be used to investigate the effect of a wide range of parameter values, while experimentation is often limited to a few values at a time. In many cases, modelling can be an invaluable tool, but the results of and the assumptions made during the modelling must always be reviewed critically, and experimental validation should be done whenever possible.

PEMFC modelling is typically based on modelling one or more of the following phenomena:

- mass transfer, i.e., modelling fluid, species and two-phase behaviour of water
- heat transfer
- charge transfer
- electrochemistry of the cell reactions
- mechanical stress, i.e., internal compression pressure.

Although the principle is fairly simple – hydrogen and oxygen react to form water, heat and electricity – the modelling of the cell phenomena is quite complicated. The different length scales involved are one reason for this complexity as fuel cell phenomena. In short, the fuel cell phenomena occur in:

- the nanometre range, modelled by density-functional theory and molecular dynamics
- the micrometre range or the material structure level
- the millimetre – metre scale for flow dynamics, mass, heat and charge transfer by continuum mechanics.

The time scales are as diverse, as electrochemical phenomena occur very quickly, whereas the mass and heat transport phenomena are slower[2]. These different time and length scales cannot be handled by a single model; instead each model usually focuses on one of these.

It is practically impossible to create a fuel cell model that takes into account all of the complex phenomena occurring in the cell. In a sense, this is true of all modelling beyond a few simple systems – the underlying physics of quantum mechanics cannot be used in its exact formulation for modelling on a macroscopic level. Even when considering classical physics, however, the various phenomena occurring in a fuel cell translate into a complex, nonlinear differential equation system. In addition to the list in the previous paragraph, the contact pressure distribution, thermal expansion of the cell, and other mechanical stresses also affect cell performance. A full model should include a time dimension in order to account for changes in operating conditions and current drawn from the cell, even the degradation of the cell should be accounted for. Solving this system in three dimensions, under dynamic conditions and handling the different length scales, ranging from nanosized catalyst particles to a macroscopic stack structure, is not possible even with modern computers.

Thus, by necessity, any fuel cell model focuses on studying a few effects in certain simplified conditions. Typical examples are modelling the electrochemistry of the cell and studying mass transport with different flow field configurations. Early models were 1D or even 0D and often studied only parts of the cell (the cathode electrode and GDL, for example), but as computers have developed, 3D models have become common and it is possible to model the whole cell geometry, see, e.g., [32]. It is still necessary, to make many assumptions and simplifications to obtain a solvable model however. For example, the anode mass transfer is often excluded in modelling, as the performance limitations

[2] A more in-depth discussion on the time and length scales can be found in [36]. The focus of this study is SOFCs, but the same principles apply to modelling PEMFCs.

(slow reaction kinetics, flooding) are usually derived from the cathode. A brief review of fuel cell modelling can be found in Section 3.1.

Another complication is that some parameter values are chosen almost arbitrarily in the absence of experimental data or theoretically derived values. For example, the exchange current density in Eq. (D) is a necessary parameter in the electrochemical equations that form the basis of a fuel cell model. This parameter depends on various factors such as the amount of catalyst on the electrodes and the cell temperature. As a result, it is different for each fuel cell and very difficult to measure. It is very common simply to use parameter fitting so that the model outcome looks reasonable and is physically sensible. The values used for the exchange of current density between different publications can differ by as much as a factor of 10^4, see, e.g., [37], for a good comparison of values used in various studies. Thus, the results may seem correct but can be unreliable. Mistakes in the modelling (simple numerical errors or more profound problems) could have been concealed by choosing parameters so that good-looking results are obtained. Thus, there is no guarantee that predictions given for other parameters will correspond to reality, i.e., the results cannot be extrapolated.

The exchange of current density is only one example; many other problematic parameters exist, for example, in two-phase modelling (condensation and evaporation rates, capillary pressure equations). Most of the two-phase parameters used are derived from experiments on sand or soil, which makes using these correlations for the fibrous, partially hydrophobic GDL media questionable (see, e.g., [38]). It is usually also necessary to average many material properties that in reality are not isotropic, such as GDL porosity or the contact resistances between different layers in the cell, in the absence of more detailed data. The results obtained from these models may be accurate in terms of the whole cell but, at worst, grossly inaccurate at describing local phenomena.

All these difficulties do not rule out the fact that modelling is very useful when used correctly however. It is simply one of several tools and has its limitations just like everything else. Modelling results should simply never be taken at face value but approached critically. It should also be remembered that even though a given model may oversimplify or exclude one aspect of the fuel cell phenomena it may still give valuable data on other aspects. Models can be developed further as more experimental data on various parameters become available.

3.1 A Short Review of PEMFC Models

This section provides a brief review of how fuel cell modelling has evolved from the first 0D analytic models to the complex 3D models used today. The modelling studies discussed in this section have been divided according to the method, dimension and aim of the modelling. It is not easy to categorize fuel cell models, and many models do not fit into any of the categories discussed here, e.g., spherical agglomerate modelling, see, e.g., [39]. The following sections are intended to give the reader a general idea of FC modelling without going into detail, as it is not possible to include the whole spectrum of FC modelling within the scope of this thesis. More detailed reviews on FC modelling can be found in, e.g., [40, 41].

Analytical models

Fuel cell models typically use some computational tool such as the Finite Element Method (FEM). There are also models based on equations that are solved analytically. An analytical fuel cell model is always highly simplified and idealized. Typical simplifications include assuming a constant temperature and reactant concentration. The dimensions in which the model is solved are reduced to zero or one. The underlying physics is usually also simplified by linearizing equations that could not otherwise be solved analytically. The results are not very accurate, especially at larger current densities. Analytical models can be used to gain approximate current-voltage dependencies and performing short calculations on simple systems, see, e.g., [42, 43]. Analytical models give a basic view on the cell operation in ideal conditions. Although many early models were analytical, and numerical 3D modelling is now more common due to more powerful computers, analytical or semi-analytical modelling is still being performed, for example, in [44, 45].

Semi-empirical modelling

In many cases, the physics of the fuel cell phenomena is either not well understood or are difficult to incorporate into modelling for practical reasons. In order to solve or avoid these issues, researchers may resort to using empirically obtained differential or algebraic equations instead of more accurate, theoretically derived ones. Many fuel cell models employ some empirical correlations; a typical example is equations for calculating the conductivity of a partially humidified membrane. A widely used correlation for this parameter was suggested by

Springer et al. in [46]. Semi-empirical modelling is fairly common, examples of empirical cell models can be found in, e.g., [47–49]. Semi-empirical models are also used in stack modelling in which more detailed models would require too much computing capacity.

The use of semi-empirical relations is often necessary due to a lack of better alternatives, but it should be avoided when possible. Firstly, semi-empirical correlations usually apply to a certain parameter range outside of which they can be inaccurate. Failure to recognize this may lead to erroneous conclusions. Secondly, the use of empirical correlations does not further the cause of understanding the underlying physics of a fuel cell. Resorting to empirical correlations may prevent us from learning new mechanisms that could be manipulated in order to improve fuel cell performance. Semi-empirical models may be fairly accurate in modelling designs and materials that are already in use, but they cannot give predictions on how new, alternative materials or new innovative design could affect cell operation.

One-dimensional models

1D models can be analytical, but if the equations are not linearized they are usually solved by discretization and numerical algorithms. This has the benefit of making the results slightly more reliable. However, 1D models are still limited to the overall correlations for current and voltage and other fuel cell characteristics. The study of many local phenomena is beyond 1D models, which assume that the cell is identical in each direction and thus cannot take into account the difference between flow field plate ribs or channels. The early fuel cell models such as presented in [50, 51] were typically 1D with many simplifying assumptions. They focused on mass transport, water management and cathode flooding.

Two-dimensional cell models

2D models are typically either channel models or channel cross-section models. The former can be used to study how the reactant and reaction product concentrations vary along the channel as the reactants are consumed. The latter gives information on, e.g., how electrical current is conducted to the flow field plates. All 2D models share the assumption of an infinite planar cell. Flow fields and other 3D phenomena cannot be studied with 2D models. A typical 2D model consists of the MEA and GDLs, and symmetry boundaries are employed. According to the aim of the study, some cell components can be excluded, for in-

stance, if the aim is to study cathode mass transport, the anode side and even the membrane may be excluded. 2D models can be very useful in cases in which the computational power is not sufficient for making a 3D model. This is often the case if small geometrical details such as the thin electrode layers are included as a modelling domain. In such cases, the computational grid or mesh will be very fine, making the model heavier to solve. 2D models can give new information on local phenomena.

2D models are still widely used, as 3D models are either unnecessary or impractical for studying many fuel cell phenomena. Some examples can be seen in, e.g., [52, 53]. A typical 2D model focuses on transport phenomena in the membrane and GDLs or local current distribution.

Three-dimensional cell models

3D models are often the most realistic ones as the cell geometry can be modelled more or less exactly as it is, although many other simplifications still have to be made. However, this also means that solving these models takes more computer capacity and time. 3D models are at their best when studying phenomena that cannot adequately be modelled in 2D such as reactant flow and distribution. A 3D model can be used to gain information on whether the reactants are distributed evenly across the whole cell or the current distribution of the cell is uniform.

Many 3D models such as the early examples presented in [54–56] exclude the MEA or the electrodes, as these are very thin layers and greatly increase the size of the computational grid in a 3D model. It is also typical not to study the whole cell or flow field but only part of it, such as one turn of a serpentine channel, i.e., to take advantage of possible repeating units and symmetry. There are also models that cover the whole active area of a small cell such as, e.g., [57], in which a 4×4 cm fuel cell was modelled to study the effects of different channel cross-sections on the performance of the cell. It is problematic that even the so-called large-scale models are models of relatively small cells, e.g., 7×7 cm^2 in [32]. Apart from the smallest applications, most real world cells will have much larger active areas to produce the necessary amount of power. The problem lies in the fact that flow field behaviour is not scalable and channel geometry that works well in small cells may therefore not perform as well in a larger cell, as the Reynolds number does not remain constant when the cell size changes. Thus, more effort should be made to model cells that could actually be used in stacks instead of those that are only used in laboratories, especially as the modelling

work done so far has shown that the flow field design is crucial to good cell performance.

Dynamic models

A dynamic model is one that includes the time dimension, i.e., in which cell operation is not constant but has a time dependency. Thus, dynamic models can be used to predict responses at the cell, stack or system level to changes or disturbances in operating conditions. Dynamic modelling is a good tool for studying performance during start-up, shutdown and voltage cycling, see, e.g., [58].

Dynamic models are typically dependent on empirical correlations (see, e.g., [59]), as including the time dimension requires significantly more computing capacity and time than is necessary for solving a steady-state model as, for example, the cell may be modelled using an equivalent circuit (such as presented in, e.g., [60]) that consists of a few electrical components such as resistors and capacitors connected so that the circuit behaves similarly to a fuel cell. This makes the models considerably simpler. Thus, in many cases the cell itself is not the point of the study, as the model focuses on the system, such as in [61]. Dynamic models that use physical and electrochemical correlations can give estimations of, e.g., how quickly the cell reaches steady-state operation after changes in operating conditions, see, e.g., [62, 63].

Two-phase models

One of the most challenging aspects of PEMFCs, both in terms of modelling and operating the cell, is water management. As discussed in Section 2.3, liquid water is necessary for the ionic conductivity of the membrane, but when too much of it accumulates in the electrodes, it obstructs mass transport to and from the reaction sites. Thus, water management is crucial in terms of cell performance.

There are two usual methods for modelling two-phase mass transport. One is known as the multiphase mixture model. In it, the two phases are considered a mixture for which the equations are solved, see, e.g., [64–66]. The data for each phase can then be calculated from the mixture solution. In the second approach, the multifluid model, both phases have a set of equations and both sets are solved simultaneously, see, e.g., [67, 68]. The latter method requires more computational capacity and a more efficient solver, as convergence is relatively difficult to attain, but it also gives more accurate results and predictions on phenomena that are unachievable using the other method. Both models work only

with porous media flow, i.e., when Darcy's law applies, and thus should not be used for modelling the two-phase behaviour in gas channels. This is problematic because water accumulation is a process that should definitely also be studied in 3D and across the whole flow field, not just as a cross section of the GDLs and MEA.

There are some experimental techniques, such as neutron imaging technology, see, e.g., [69], to study water transport and accumulation in the cell, but accurate two-phase models would be a great help in understanding and improving PEMFC water management. Many parameters for two-phase models are chosen almost arbitrarily or are derived from results of experiments performed with soil. Perhaps the most significant of these is capillary pressure for which various relations that differ significantly[3] have been used. It should also be mentioned that many two-phase models use inaccurate boundary conditions such as that at the boundary between the channel and the GDL, there is no liquid water (i.e., all water is gaseous), see, e.g., [54, 70]. This is clearly inaccurate, as many experiments have shown droplet formation in channels, see, e.g., [71]. Some studies suggest novel boundary conditions as a solution to this problem, for example, by using a basic model for droplet formation on the boundary, see, e.g., [72, 73]. However, liquid water transport in the channels, which affects the evaporation from this boundary, has never been modelled accurately, as Darcy's law does not apply in the channels and thus neither do the two-phase models presented in the fuel cell literature. Considering these issues, it is clear that two-phase modelling requires many improvements before the results can be trusted.

3.2 Modelling in This Thesis

The modelling done in this thesis focuses on gaining a better understanding of the following subjects:

- mass transport phenomena on the cathode (in Publications 1 and 5)
- the effect of thermal and electric contact resistances on local cell phenomena (in Publications 2 and 3)
- compression distribution in a stack (in Publication 4) that strongly affects the contact resistances.

[3] As an example, compare the formulations for capillary pressure used in [57] and [59].

These studies are described in the following sections. The subject under study varies between the models, but all the modelling work shares the common aim of trying to see beyond the IV-curve, i.e., studying local or cell-scale phenomena in an operating fuel cell that normally remain invisible.

Using the categories of the FC model presented in the previous section, the models made as a part of this thesis can be divided into 2D and 3D models. Two of the 2D models are cross-sectional for studying the effect of compression, contact resistances and GDL deformation discussed in Chapter 5 and Publications 2 and 3. These models study the local effects that the uneven compression resulting from the cell structure causes to the current density distribution and other variables. Another 2D model focuses on the cathode of a free-breathing fuel cell. It differs slightly from typical 2D FC models in that it includes the ambient air zone. This model was used to study the optimal way to model such a cell and, based on the results, a computationally light 3D model of a free-breathing cell was built. The 3D model was then used to study the effect of cell size and orientation on the effectiveness of the natural convection phenomenon. The free-breathing call model is presented in Publication 5 and Chapter 7.

A 3D model was built to study the flow distribution in a parallel flow field, i.e., a flow field in which continuous parallel channels cross the active area of the cell (Chapter 4 and Publication 1). This model was used to optimize the flow field geometry so that a more even flow distribution was attained. Another 3D model focused on the compression distribution in a stack (Chapter 6 and Publication 4) and was used to improve the end plate structures so that the compression distribution in the cell was limited to a suitable range.

COMSOL Multiphysics, the commercial differential equation solver software, was used in the modelling. It is based on the finite element method (FEM) in which the modelling domain is discretized to finite elements and the equations are solved in each element using piecewise continuous polynomials. A more detailed description of FEM can be found in, e.g., [74]. COMSOL is sophisticated software that is capable of creating the mesh for complex geometries and offers various solver algorithms for different types of problems.

3.3 Modelling Principles

The purpose of this section is to present the physics and electrochemistry employed in this thesis. Each of the models presented in the later sections includes only the equations essential to the subject of study. However, the underlying

physics is always the same. A general view of the physics used in the models is given in this section, and the details of each model are explained in the corresponding chapter. The modelled FC phenomena consist of mass, heat and charge transfer, electrochemical reactions, compression effects and pressure distribution. These are modelled with suitable partial differential equations and boundary conditions, depending on the model. The coupled partial differential equations are presented in the following sections.

3.3.1 Mass Transfer

The modelling of mass transfer consists of modelling the transport of reactants, reaction products and inert substances in the fuel cell. In a PEMFC, the reactants are hydrogen on the anode and oxygen on the cathode, and the reaction product is water. The inert phase is nitrogen, or a mixture of nitrogen and argon. Both these gases are present in air and thus in the cathode of a fuel cell operating on air. They do not participate in reactions but do affect the mass transport inside the cell. In this thesis, water is assumed to be in the vapour phase, as two-phase modelling, due to its complexity and inaccuracies as discussed in Section 3.1, was beyond the scope of this work. Anode mass transport is excluded from the models, however, as performance-limiting phenomena usually occur on the cathode due to the slower reaction kinetics and increased risk of flooding. In this thesis, mass transport modelling focuses on the distribution of reactants on the electrode, on the one hand studying the flow field on the scale of the entire cell, and, on the other hand locally on the scale of individual ribs and channels.

Species are transported on the cathode through convection and diffusion. An externally supplied pressure difference across the cell creates a flow through the cell, or, in the case of free convection, the lift produced by density variations in air, in turn, caused by temperature and concentration differences. On the electrode, the reactants are consumed and reaction products generated, which creates concentration gradients in addition to the density gradient. The fluid flow passes through the channels, the porous gas diffusion layer and the electrode. The membrane is impermeable to gases but can transport water. Membrane water transport is not the focus of this thesis, however, and has been modelled with a simple empirical correlation.

In the channels, the fluid flow is modelled with the Navier–Stokes and continuity equations (8) and (9). These are standard equations for modelling laminar, incompressible flow. There is no exact limit for the change from laminar to tur-

bulent flow, but fluid flow can usually be considered laminar if the Reynolds number for that flow is below 2300. This condition is met in the fuel cell environment in which the flows are relatively slow. In the porous gas diffusion layer and the electrode, however, Darcy's Law (10) is used instead.

$$-\rho\mathbf{u}\cdot\nabla\mathbf{u}+\rho\mathbf{g}-\nabla p+\nabla\cdot\left(\eta(\nabla\mathbf{u}+\nabla\mathbf{u}^{\mathrm{T}})\right)=\mathbf{S}_{NS} \tag{8}$$

$$\nabla\cdot(\rho\mathbf{u})=S_{con} \tag{9}$$

$$\nabla\cdot\left(\rho\frac{\eta}{\kappa}\nabla p\right)=S_D \tag{10}$$

Here, ρ is the average density of the fluid, $\mathbf{u}(u,v,w)$ the (mass average) velocity vector, p the pressure, κ the permeability of the porous medium, S the source term of each equation and η the average viscosity of the fluid.

Equations (8–10) model the behaviour of the fluid in terms of pressure and velocity in a centre of mass frame. In order to take into account the effect of concentration-driven flow, diffusion must also be modelled. The use of the simple diffusion equation (i.e., Fick's Law) is incorrect in a fuel cell cathode, however, as the fluid has three components (oxygen, water and nitrogen) that all have different sources, sinks and diffusion constants. Thus, multicomponent diffusion equations, or Maxwell–Stefan diffusion equations (11) and (12), must be employed. It should be noted that although the Maxwell–Stefan equations can be written for each component, they only need to be solved for two, as the third component can always be calculated from the other two, as the mass fractions must add up to one. Thus, the mass fraction of nitrogen is calculated from those of water and oxygen.

$$\nabla\cdot\left(-\rho\omega_i\sum_{j=O_2,H_2O,N_2}\tilde{D}_{ij}\left(\nabla x_j\right)+\rho\omega_i\mathbf{u}\right)=S_i^{mass},\qquad i=\mathrm{O_2},\mathrm{H_2O},\mathrm{N_2} \tag{11}$$

$$\nabla x_j=\frac{M^2}{M_j}\sum_{\substack{k=O_2,H_2O,N_2\\k\neq j}}\left(\frac{1}{M}+\omega_k\left(\frac{1}{M_k}-\frac{1}{M_j}\right)\right)\nabla\omega_k \tag{12}$$

Here, ω_i is the mass fraction of species i, $\tilde{D}_{\mathrm{ij}}$ the Maxwell–Stefan diffusion coefficient, M_i the molar mass and x_i the molar fraction of species i. Maxwell–Stefan equations can also be written for molar fractions (as opposed to mass fractions):

$$\nabla \cdot (c x_i \mathbf{u}) - \nabla \cdot \left(c \tilde{D}_{eff} \nabla x_i \right) = S_i^{molar}, \qquad i = \mathrm{O_2}, \mathrm{H_2O}, \mathrm{N_2} \tag{13}$$

The formulations (11) and (13) are equivalent. More information on the Maxwell–Stefan equations can be found in, e.g., [75]. Both forms have been used in this thesis.

The source terms S in equations (8–11) and (13) arise from the cell reactions, which consume oxygen and produce water. Thus, they only exist in the electrodes and are zero elsewhere. The exceptions to this are the source terms in the Navier–Stokes and continuity equations that are only used in the flow field model discussed in Chapter 4 and Publication 1, in which the only modelled cell component was the flow field and thus the effect of the reactions modelled as though the reactions occurred in the channels.

$$\mathbf{S}_{NS} = -\frac{jA}{zFV_{ch}} M_{O2} \mathbf{u} \qquad \text{(for Navier–Stokes eq.)} \tag{14}$$

$$S_D = \frac{j}{4F} \left(M_{H2O} - M_{O2} \right) \qquad \text{(for Darcy's Law)} \tag{15}$$

$$S_{con} = \frac{jA}{zFV_{ch}} \left(\alpha M_{H2O} - M_{O2} \right) \qquad \text{(for continuity eq.)} \tag{16}$$

$$S_i^{mass} = \begin{cases} -\frac{j}{4F} M_{O2}, & i = \mathrm{O_2} \\ \frac{j}{2F} M_{H2O}, & i = \mathrm{H_2O} \end{cases} \quad \text{and} \quad S_i^{molar} = \begin{cases} -\frac{j}{4F}, & i = \mathrm{O_2} \\ \frac{j}{2F}, & i = \mathrm{H_2O} \end{cases}$$

(for Maxwell–Stefan diffusion equation) (17)

Here, j is the reaction current density at the electrode, A the active area of the cell, z the number of electrons participating in the reaction, F the Faraday number, α the portion of reaction product water leaving the cell through the anode[4] and V_{ch} the volume of the channels.

[4] A portion of the reaction product water can be driven from the anode to the cathode by diffusion.

3.3.2 Heat and Charge Transfer

PEMFCs operate at a lower temperature than other fuel cells such as SOFCs, but heat transfer is nevertheless an essential factor for cell performance. In this thesis, the focus is not on cell or stack thermal management but on local differences in temperature. For example, local temperature variations, i.e., often called hot spots, may be formed due to the rib/channel structures and uneven current density. These do not affect the cell performance very much but can cause premature membrane degradation and thus shorten the lifetime of the cell.

The modelling of heat transfer is fairly straightforward. There are two mechanisms of heat transfer in the cell: convection and conduction. Heat transfer by radiation is usually not significant within a PEM fuel cell as the temperature and the thermal bulk and contact resistances are relatively low. Heat transfer is modelled using equation (18):

$$\nabla \cdot (k \nabla T) = \sum_i c_{p,i} \rho_i \mathbf{u} \cdot \nabla T + S_T \tag{18}$$

Heat is produced by the cell reactions and ohmic heating by electronic and ionic current. Thus the thermal source term S_T in each region is

$$S_T = \begin{cases} \sigma^s_{GDL} \left(\nabla \Phi_s\right)^2, \text{in the GDLs} \\ \sigma^m_{mem} \left(\nabla \Phi_m\right)^2, \text{in the membrane} \\ \sigma^s_{CL} \left(\nabla \Phi_s\right)^2 + \sigma^m_{CL} \left(\nabla \Phi_m\right)^2 + j_a \eta_a + \dfrac{j_a T \Delta S_a}{2F}, \text{ in the anode} \\ \sigma^s_{CL} \left(\nabla \Phi_s\right)^2 + \sigma^m_{CL} \left(\nabla \Phi_m\right)^2 - j_c \eta_c - \dfrac{j_c T \Delta S_c}{4F}, \text{ in the cathode} \end{cases} \tag{19}$$

Here, σ is the electronic or ionic conductivity of the GDL for membrane (*mem*) and catalyst (*CL*), Φ_m and Φ_s the ionic and electronic potential, η_a and η_c the overpotentials of the anode and cathode, j_a and j_c the reaction current densities at the anode and cathode, T the temperature and ΔS the change in entropy of the reaction. Note that as j_c is negative, the cathode side source terms have negative signs before the source terms.

The charge transfer in a PEMFC comprises the movement of both electrons and ions. Thus, it is necessary to model both ionic and electronic potential separately. The former exists only in the membrane and electrodes while the latter

exists in the electrodes and GDLs. The charge transfer, ionic or electronic, is modelled by

$$-\nabla \cdot \left(\sigma_{mem,GDL} \nabla \Phi_{m,s}\right) = S_{m,s} \tag{20}$$

The conductivity $\sigma_{mem,GDL}$ is a function of membrane humidity. The source terms, S_m for the ionic potential and S_s for the electronic potential, are non-zero in the electrodes:

$$S_m = \begin{cases} j_a \text{ , anode} \\ -j_c \text{ , cathode} \end{cases} \text{ and } S_s = \begin{cases} -j_a \text{ , anode} \\ j_c \text{ , cathode} \end{cases} \tag{21}$$

The reaction current densities j_a and j_c at the electrodes are calculated according to equation (D) presented in Section 2.5.

An interesting aspect of heat and charge transfer in a fuel cell is that these variables are, in reality, not continuous between different cell components. This is due to contact resistances between the components, e.g., between the GDL and the electrodes. These contact resistances have spatial variation, as the compression applied to these components varies on the scale of the whole active area and locally under the ribs and channels. The differences in thermal and electric contact resistances can have a significant effect on cell performance and lifetime, which is discussed in Chapter 5 and Publications 2 and 3.

3.3.3 Mechanical Modelling

The equations presented in the last two sections are all transfer equations and are used in similar models. This thesis also includes a study of the compression distribution in a stack, which is discussed in more detail in Chapter 6 and Publication 4. Compression is modelled by solving equation (22) in the whole modelling domain with appropriate boundary settings.

$$\nabla \cdot \sigma_{str} = 0. \tag{22}$$

Here, $\sigma_{str} = (\sigma_x, \sigma_y, \sigma_z, \tau_{xy}, \tau_{yz}, \tau_{xz})^T$ is a stress tensor in which normal stresses are marked with σ_i and shear stresses with τ_{ij}. The stress tensor is related to the strain tensor $\gamma = (\gamma_x, \gamma_y, \gamma_z, \gamma_{xy}, \gamma_{yz}, \gamma_{xz})^T$ by Hooke's law:

$$\sigma_{str} = D\gamma \tag{23}$$

where D is the elasticity matrix calculated using Young's modulus and Poisson's ratio:

$$D = \frac{E}{(1+\upsilon)(1-2\upsilon)} \begin{bmatrix} 1-\upsilon & \upsilon & \upsilon & 0 & 0 & 0 \\ \upsilon & 1-\upsilon & \upsilon & 0 & 0 & 0 \\ \upsilon & \upsilon & 1-\upsilon & 0 & 0 & 0 \\ 0 & 0 & 0 & \frac{1}{2}-\upsilon & 0 & 0 \\ 0 & 0 & 0 & 0 & \frac{1}{2}-\upsilon & 0 \\ 0 & 0 & 0 & 0 & 0 & \frac{1}{2}-\upsilon \end{bmatrix} \tag{24}$$

The strain ε is a measure of the material's deformation, i.e., the change in length at a certain point divided by the original length at that point. The components of the strain tensor ε are calculated by

$$\gamma_i = \frac{\partial \mathbf{u}_i}{\partial i}, \ \gamma_{ij} = \frac{\partial \mathbf{u}_j}{\partial i} + \frac{\partial \mathbf{u}_i}{\partial i}, \ i, j = x, y, z \tag{25}$$

where $\mathbf{u} = u\mathbf{i} + v\mathbf{j} + w\mathbf{k}$ is the deformation vector.

Using these equations, the following differential equation can be written for the deformation:

$$\nabla \cdot (D\nabla \mathbf{u}) = 0, \tag{26}$$

which is the differential equation solved. This model assumes that all materials are isotropic, homogeneous and elastic. The boundary conditions are simple: an inward force is applied to areas corresponding to the locations where nut and bolt assemblies are in the stack. The stack geometry was symmetric, so only one eighth of the structure had to be modelled. Thus, there are some symmetry boundaries at which the material is assumed to be immobile in the normal direction. Other boundaries may move freely.

4. Flow Field Modelling

Here, the aim of flow field modelling is to study the velocity profile, reactant and reaction product distribution in a fuel cell and thus determine which kind of flow field is optimal for a given fuel cell structure. As discussed in Section 2.3.3, there are a number of different flow field typologies as well as many changeable parameters, such as the channel dimensions and cross-sectional shape. Flow field behaviour does not scale with size, and thus a small fuel cell requires a different flow field design to a large one. Operating conditions, especially humidity and operating current, affect the water management of the cell and thus set their own requirements for the flow field. As a consequence, it is not possible to have a universally optimal flow field. Instead, the flow field should be designed separately for each application.

The most common problems of flow fields (in addition to the cost and weight of the bipolar plate) are uneven reactant distribution and insufficient liquid water removal. The former is typically due to poor flow field design and is common with the parallel channel configuration. The latter results from low flow velocities or generally poor flow field design and is harder to model, as two-phase modelling, in general, is not very exact and droplet formation and behaviour are difficult to predict. There have been experimental as well as modelling efforts concerning liquid water removal in the bipolar plate, see, e.g., [76–78], but in this thesis the focus is on improving the reactant distribution.

There are three common approaches to designing a channel system for a PEMFC. The first is to have several parallel channels across the active area. The second is to have a few channels, or just one long channel, that cover the active area by twisting and turning (serpentine channels). The third is to have dead-end channels that force the flow into the GDL (interdigitated channels). For a more in-depth explanation of these three and other flow field types, see, e.g., [79]. The parallel channel system, the focus of this thesis, has often been criticized for

unequal flow velocities in the channels, thus causing uneven reactant distribution. It also has a low pressure drop across the cell, however, which means that less capacity is required from auxiliary equipment such as pumps, though this may also make water removal less effective. With serpentine (or interdigitated) channels, it is easy to accomplish an even flow distribution as there are only a few channels, which has led many to prefer these configurations over the parallel one.

This thesis focused on studying the parallel channel configuration and thus showing that it can be used effectively as long as the flow field design is optimized. By modelling the cathode of a PEMFC, it was demonstrated that the crucial detail is the way the flow is distributed into the channels. In order to illustrate this concept, a basic parallel channel system is presented in Figure 4.

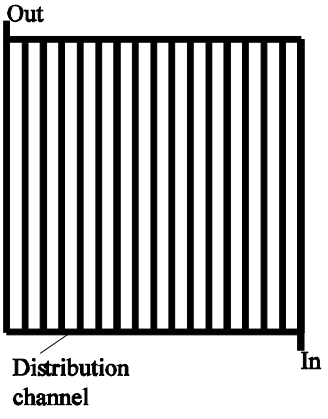

Figure 4. A schematic of a typical parallel flow field design.

Here, the distribution channel has the same width as the other channels. This is not an optimal solution, however, as the resulting flow distribution tends to be uneven. In order to study the effect of the distribution channel shape or, more accurately, its hydraulic resistance to the flow distribution, the existing cell geometry was taken as a starting point. This geometry is illustrated in Figure 5. This is a channel system in which the channels form groups of five in a 3D structure and the distributor channel has a slightly more complex geometry, but the parallel channel principle is the same as in Figure 4.

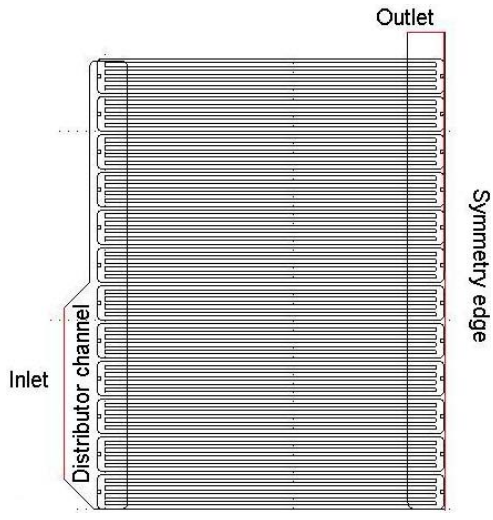

Figure 5. Starting point geometry for flow field modelling. As the structure is symmetrical, one half of the channel system is modelled with one boundary functioning as a symmetry boundary.

The flow field of this geometry was modelled using the Navier–Stokes equations (8) and the continuity equation (9). At the inlet, velocity was set to correspond to a stoichiometry of 1.2 and, at the outlet, the pressure relative to the inlet was set to zero. Thus the real pressure can be calculated by adding atmospheric pressure. The reason for not using atmospheric pressure as a boundary condition is that it is several orders of magnitude larger than the pressure variations within the model, and thus using it may create unnecessary numerical problems in the solution process. Due to the symmetry condition, one boundary had the symmetry boundary condition, i.e., the normal velocity and viscous stress at that boundary were set to zero. The remaining boundaries had the so-called no-slip condition, i.e., the velocity was set to zero.

The effect of the cell reactions to the fluid composition was taken into account by adding source terms to equations (8) and (9) according to equations (14) and (15). The density and viscosity of the fluid were calculated from the composition of the gas mixture and thus vary within the modelling domain. Equations (14) and (15) are based on the assumption that the momentum of the reactants consumed in the reactions is lost to the porous media. This may not be completely correct, and thus alternative source terms for which the momentum was conserved in the flow were also modelled. The results showed that the relative dif-

ference in flow velocities between the models using these source terms was negligible at 0.1%.

It should be noted that all water was assumed to be in gaseous form. The relative humidity of the gas mixture was calculated from the solution and had a maximum value below 100% if the relative humidity of the inlet flow was a maximum of 64%. Thus, there is no water condensation with the boundary conditions used here (21% inlet relative humidity corresponding to typical operating conditions). However, this does not hold true for all PEMFC operating conditions, and thus the model could be developed further if two-phase phenomena could be modelled accurately. In this case, two-phase modelling is more complicated than usual as the widely used relations are developed for porous media and do not apply to channels.

The modelling of the geometry presented in Figure 5 showed that the flow distribution in the channels was uneven, with the flow velocity in the fastest channel being 16% higher than in the slowest channel. The flow field geometry was altered with a trial and error method. The key to improving the flow distribution proved to be changing the flow resistance of the inlet distributor channel. This was done by narrowing the end of the distributor channel, as the highest channel velocities had been formed at the channels starting from the end of the distributor channel. The changes made to the distributor channel are illustrated in Figure 6.

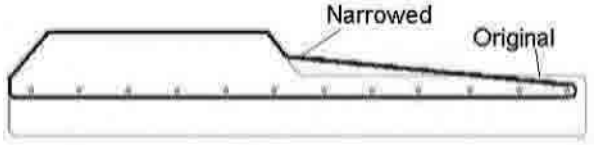

Figure 6. The original and modified distributor channel geometries.

The relative channel velocities of the original and modified geometries are illustrated in Figure 7. Although the original distribution was quite good, it was further improved by the changes made to the distributor channel.

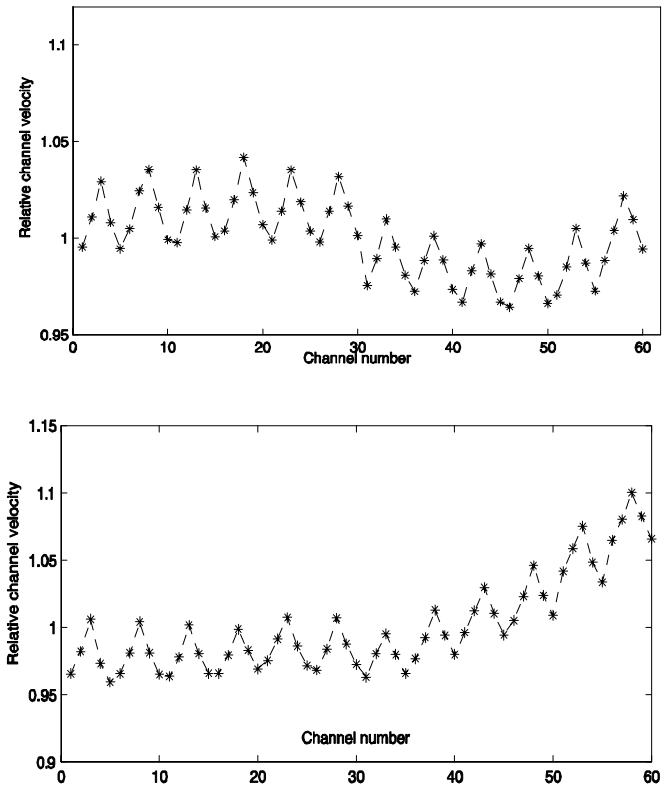

Figure 7. Flow velocities in the channels with the original (left) and modified (right) distributor channel.

The modelling results were validated experimentally by observing the progress of ink dispersed in water in the channels. Flow velocity was calculated from video images by working out the time an ink pulse required to traverse each channel. The flow field size and flow velocity were scaled in order to reach a corresponding Reynolds number. The fluid was changed from gaseous to liquid for practical reasons. The measurement accuracy was not sufficient for quantitative results, but qualitatively the experimental results were in agreement with the modelling results and confirmed that the improved geometry gives a more even flow distribution. Originally, the purpose was to employ the improved geometry in a stack and see if performance improvement could be perceived. This was never done, however, as the research project of which this work was part abandoned the stack development in favour of using a commercial stack, and to perform the experiment just to validate the model would have been too expensive.

The main result from the flow field modelling was that parallel flow fields can have sufficiently even flow distribution, contrary to some claims. The flow field design can be significantly improved by fairly simple modelling, and excluding thin components such as GDL and MEA makes it possible to model larger channel systems such as would be used in a real stack. The inlet distributor channel should be designed individually for each flow field using modelling as an optimizing tool in order to improve performance.

5. Contact Resistance Modelling

A significant part of the ohmic losses in a fuel cell arises from the contact resistances between different components, most importantly between the gas diffusion layer and its adjacent components: the electrodes and the bipolar plate ribs. By reducing these contact resistances, the cell performance can be improved. The subject of the GDL contact resistance has been studied in, e.g., [80, 81], but two factors are not included in their studies. Firstly, compression affects the bulk conductivity as well as the porosity, thermal conductivity, permeability and water transport properties of the GDL. Thus, finding the optimal compression is not a straightforward matter but requires finding the compromise that best suits these conflicting factors. Secondly, the compression within a fuel cell is not constant. On the one hand, the compression is applied to the cell or stack through end plates using a nut and bolt assembly. The variations in compression due to this mechanism are discussed in the following chapter, but here it is sufficient to note that the size of these variations can be large, if the cell design is not optimal. On the other hand, there are notable local variations in the GDL compression due to the alternating rib/channel structure of the flow field plates.

The study of the effect of local variations was the point of interest in Publications 2 and 3 and is discussed in this chapter. The model developed for this purpose consisted of a cross-section of the cell, one half of it beneath a channel and the other half beneath a rib. As little data were available on the dependencies, parameters such as the GDL thermal and electrical conductivity and the contact resistance between the GDL and the electrodes under compression were experimentally measured by others in the laboratory and the results were published in [82]. Based on these results, a model using compression-dependent parameters for permeability, porosity and electrical conduction was built and presented in Publication 2. This model gave some interesting results, especially with regard to local current distribution, for which the model predicted a sharp peak in the catalyst layer beneath the rib/channel edge. Such a peak could lead to the creation of a hot spot and thus membrane damage.

The model presented in Publication 2 was isothermal, however, and thus could not give data on the temperature distribution. The contact resistance between the GDL and the catalyst layer had been assumed to have a simple correlation with the contact resistance between the current collector and the GDL. In reality, the GDL is free to deform under the gas channel. Thus, the compression distribution between the GDL and electrode may not be equal to the one between the GDL and the bipolar plate. Furthermore, the correlation between compression and contact resistance is not necessarily the same for these pairs as the solid and smooth surface of the BP is quite different to that of the microporous electrode. Consequently, new experiments were conducted and the results published in [83]. These results were incorporated into the model in Publication 3 along with the heat conduction equation (18). With these more accurate parameters, the current density peak was lower though still in existence. The modelling domain is illustrated in Figure 8, along with the model that is typically used, which assumes the GDL is a uniform block of constant thickness and was used as a base case for comparison in this study.

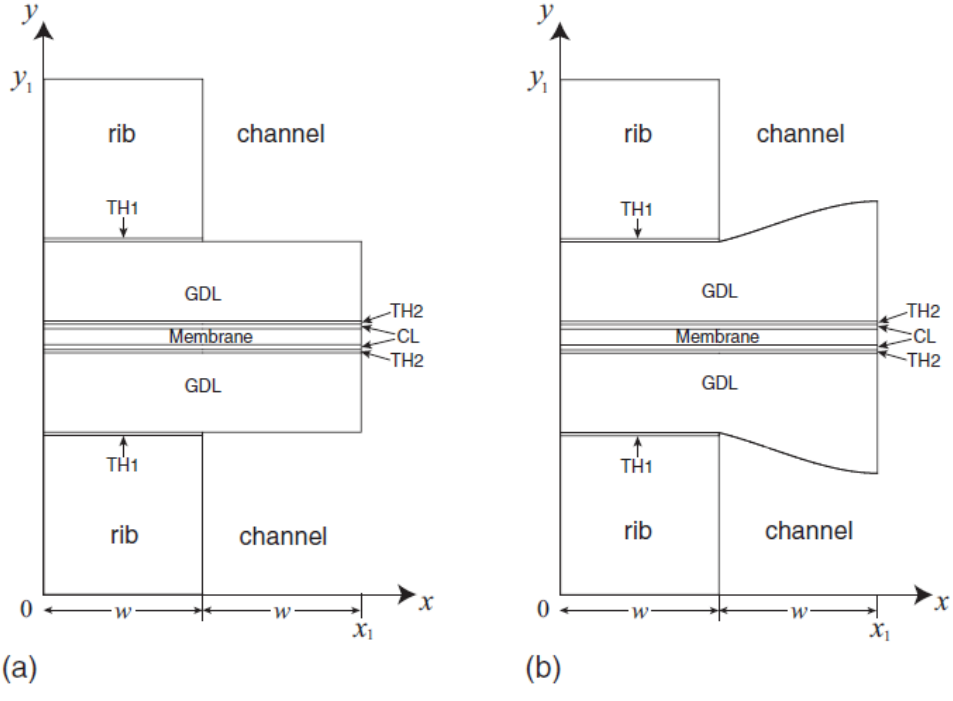

Figure 8. The base case (a) and the contact resistance variation model (b) (pictures by Iwao Nitta, Publication 2).

Current density distributions of the variable contact resistance model and the base case model are illustrated in Figure 9. The perpendicular current density at the GDL/electrode boundary is illustrated further in Figure 10. Here, it is easy to see the increase in current density beneath the rib/channel boundary. The current density distribution is clearly not constant locally, as has been assumed in many earlier models, but can have large local variations. The variation in current density is due to the large amount of lateral current density. The current generated in the reactions under the channel is conducted to the BP through the portion of electrode under the rib, as the contact resistance between the electrode and the GDL is much lower under the rib, and the current is always conducted through the path of least resistance. The current density peak effect is, in practice, impossible to discern from the overall cell performance. However, it can cause lifetime issues if the electrodes and MEA are damaged by the resulting temperature variation. Furthermore, if the poor contact resistance under the channel could be improved, the overall performance of the cell could also show improvement.

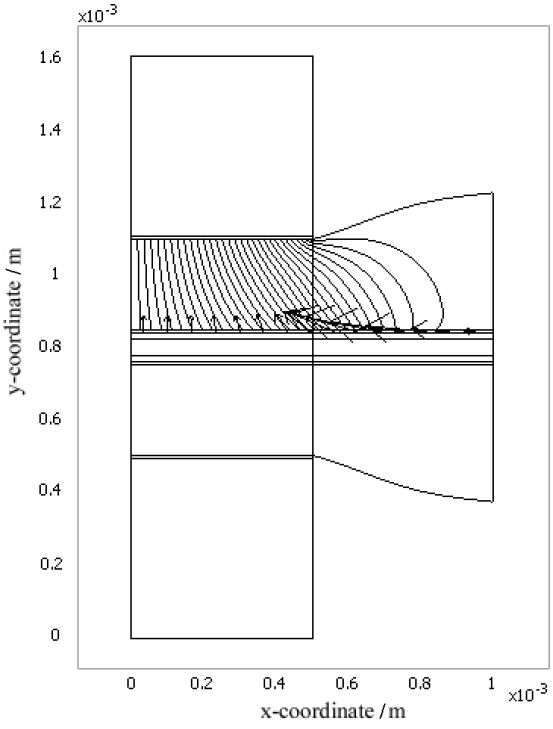

Figure 9. The model geometry of the contact resistance model and the current density in the cathode. The arrows show the direction of the current while the lines are potential level curves. There is a large lateral current in the catalyst layer beneath the channel where the contact resistance between the GDL and the electrode is high. (Picture by Iwao Nitta, Publication 3.)

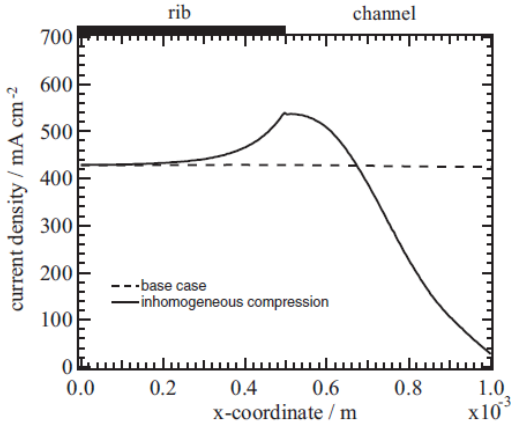

Figure 10. The perpendicular current distribution at the GDL/electrode boundary (picture by Iwao Nitta, Publication 3).

The main result of the contact resistance modelling was that local changes in compression that result in contact resistance variation can have a significant effect on the local current density distribution. Large current density variations can cause damage in the long term through ohmic heating and temperature variation. The large contact resistances under the channels that force the current to travel within the electrodes can also result in ohmic losses.

6. Modelling the Compression Distribution in a Stack

The previous chapter discussed the effect of compression in a fuel cell on a small scale. This chapter focuses on a related matter, i.e., studying how compression is distributed throughout the stack and the individual cells in the stack. The motivation is obvious: the contact resistance experiments indicate that many critical parameters such as the contact resistances and the GDL bulk transport properties are very sensitive to compression. Based on literature, the ideal compression range seems to be approximately 10–30 bar depending on the materials [84–86], with 10–15 bar being optimal for a typical cell.

The distribution of compression in a stack was studied by taking an existing stack as a starting point. The stack was modelled with five unit cells, a number that was decided as large enough to simulate a real stack but small enough that the model could be solved with the available computing capacity. Symmetry boundaries were used to further decrease the heaviness of the model. The end plate geometry is illustrated in Figure 11. The modelling domain consisted of end plates, bipolar plates, gaskets and an averaged layer representing the GDLs and MEA, which could not be modelled as separate layers as they are thin layers and would thus require a very fine mesh. The compression was directed to the end plates via circular boundaries corresponding to the nut and bolt assembly. The end plates were steel plates of constant thickness.

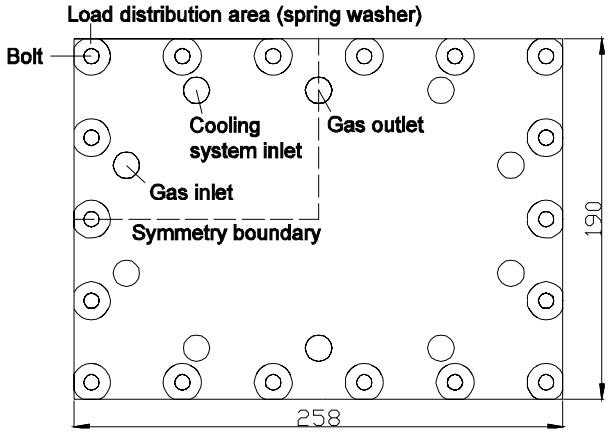

Figure 11. The end plate geometry and symmetry boundaries. The dimensions are in millimetres.

The results showed that, in this case, the compression distribution is quite far from optimal, as can be seen in Figure 12, which displays the pressure on the GDLs of the middle cell in the stack. Most the active area experiences pressure below 10 bars and the centre parts even lower than 2 bars. In an operating fuel cell, this pressure distribution can be expected to lead to problems with contact resistances, thus lowering the performance.

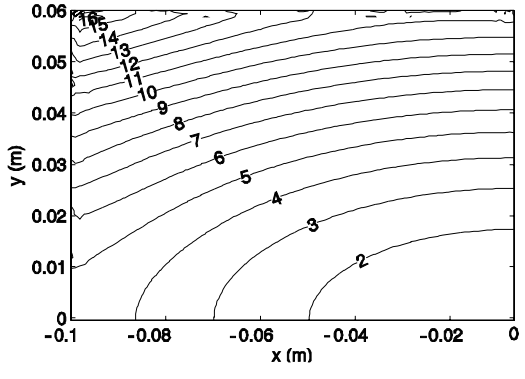

Figure 12. The clamping pressure isobars on the GDL surface of the original flat plate (1 kN load at each bolt). The pressure values are in bars. The origin (lower right corner) is situated at the centre of the cell.

The problem is due to two main factors. Firstly, the force applied to the nuts and bolts was equal at each bolt, and due to their placement (see Publication 4) the corners of the plate experienced more pressure than the rest of the edges. Secondly, the uniformly thick steel plate is not rigid enough to distribute the pressure evenly and deforms slightly. Most of the pressure is directed to the gaskets. The end result is that while the corners of the active area are nearly crushed under almost 20 bar pressure, the centre areas of the cell experience only slight pressure at 2 bar or less.

Both factors were addressed in order to improve the pressure distribution. Different torques were applied to the bolts until a suitable configuration was found. The end plate structure was changed from a uniformly thick plate to a ribbed structure that also made the plate lighter. Further weight was lost by changing the end plate material to aluminium. While less rigid than steel, aluminium has other beneficial qualities, such as lower density. Aluminium is also easier to machine, which is important for future commercial applications. Figure 13 shows the compression distribution for different end plate configurations and materials. The best one is an aluminium plate with 7-cm-high aluminium ribs. Here, the pressure distribution remains within the ideal range of 10–15 bar.

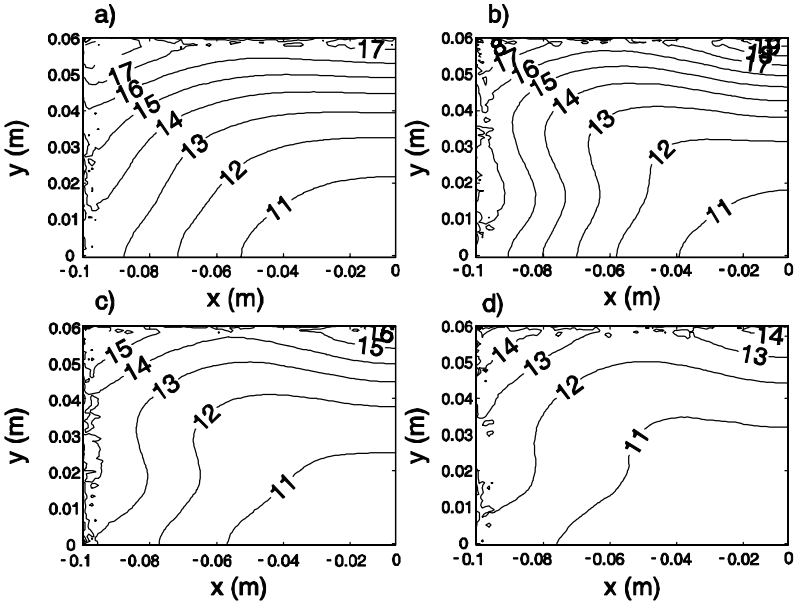

Figure 13. Pressure isobars on the GDL: a) 4 cm steel ribs, b) 5 cm aluminium ribs, c) 6 cm aluminium ribs and c) 7 cm aluminium ribs. The pressure values are in bars.

The experiments were also validated experimentally using a pressure-sensitive film. The accuracy and range of the film combined with rather large manufacturing tolerances in the stack components made the results more qualitative than quantitative however. Using the five cells in the stack resulted in mostly noise being measured, but using a single stack showed a clear correlation with the modelling results.

The main result of the stack compression modelling is that the compression distribution in a stack can be unacceptable if the stack has not been designed with care. The compression distribution can be significantly improved with fairly simple alterations however. Single cell units are more likely to suffer from uneven compression distribution as, in a large stack, the manufacturing tolerances, i.e., variations in the thickness of the components, can dominate the resulting compression distribution. These results should also be considered in the context of the previous chapter, i.e., the effect of compression on a local scale where noticeable effects on local current density distribution were observed. Large variations in cell compression may lead to surprising local effects, such as very high electrical and thermal contact resistances or greatly reduced mass transport capabilities that affect cell performance and lifetime.

The compression model created in this work was further developed by others in the laboratory, see, [87, 88]. The improvements there include adding a compression equalizing layer made of a flexible material and including the effect of thermal stresses in the model.

7. Modelling a Free-breathing Fuel Cell

This chapter and Publication 5 focus on modelling the mass transfer on the cathode of a free-breathing PEMFC. The objective was to create a computationally light but valid 3D model. This was done in two steps, first a 2D model was built for testing different approaches to the modelling and then a 3D model was built according to these results. The 3D model was then used to study briefly the effect of size and position on cell performance.

Models of free-breathing fuel cells have been built before, see, e.g., [89, 90]. As these studies do not describe in detail how they chose their model boundary settings and other such details, it was decided to start the model building by trying out different choices to see their effects on the result. The two main issues to be solved with the 2D model were the type of boundary setting that should be used and how large the ambient air zone, a.k.a. free convection zone of the model (see Figure 14), should be.

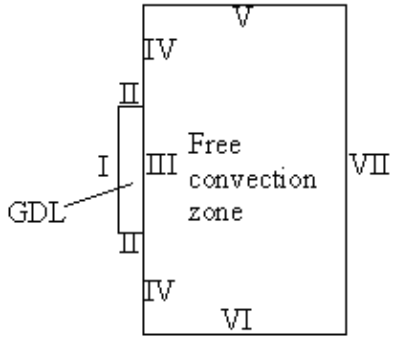

Figure 14. A schematic of the modelling domain in 2D. Note that the picture is not to scale.

The issue of boundary setting stems from the fact that there are two ways to model a free convection problem such as this one: the closed and the open boundary settings approaches, see, e.g., [91] for open and [92] for closed.

Mathematical formulation for the open boundary conditions:

$$\mathbf{t} \cdot \mathbf{u} = 0$$
Boundaries V, VI and VII: free convection zone boundaries (27)

$$\mathbf{n} \cdot (\mathbf{J}_i + \rho\omega_i\mathbf{u}) = \mathbf{n} \cdot \mathbf{u}\rho\omega_i \quad \text{(Boundary V)} \tag{28}$$

$$\omega_{O_2} = \omega_{O_2}^0 \,,\ \omega_{H_2O} = \omega_{H_2O}^0 \quad \text{(Boundaries VI and VII)} \tag{29}$$

$$T = T_0 \quad \text{(Boundary VII)} \tag{30}$$

For the closed boundary conditions:

$$\mathbf{u} = 0$$
Boundaries V, VI and VII: free convection zone boundaries (31)

$$\omega_{O_2} = \omega_{O_2}^0 \,,\ \omega_{H_2O} = \omega_{H_2O}^0 \quad \text{(Boundaries VI and VII)} \tag{32}$$

$$T = T_0 \quad \text{(Boundary VII)} \tag{33}$$

The other boundary conditions can be found in Publication 5. The difference here is that the open mode allows for mass and momentum transport through the boundaries whereas the closed version does not. Species and thermal energy transport are allowed in both models. Earlier fuel cell models such as [89] have used the previous one, but the latter has typically not been used in free-breathing PEMFC models and there are usually no arguments as to why this particular choice has been made.

The sizes of the ambient air zones were selected so that enlarging them further had no significant effect on the solution. It is clear that the closed boundary setting model requires a much larger modelling domain due to the fact that the closed boundaries force a vortex-like flow to form, which requires more space to model. Thus, the open boundary setting model is much smaller. The modelling of both situations revealed that the results are equivalent in the area they share, i.e., the domain of the open boundary conditions model. The open boundary settings model is smaller and requires a smaller mesh, and it is thus easier to solve. It would also appear that solving the closed boundary settings model, in

addition to requiring a larger mesh, is also otherwise more time-consuming, as the vortex shape of the flow forces the solution algorithm to advance more slowly due to the higher complexity. Taking these observations into account, it is clear that the superior choice is the open boundary setting models, even if the one used in previous PEMFC models was the closed boundary settings model.

The 3D model was built using the open boundary conditions. The modelling domain of the 3D model is illustrated in Figure 15.

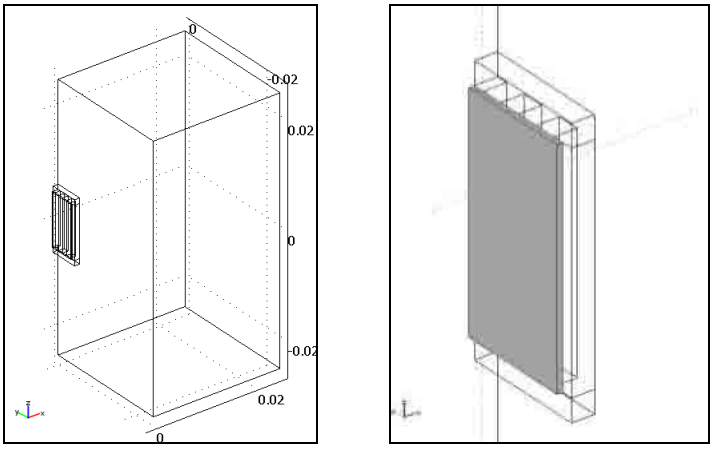

Figure 15. A schematic of the modelling domain in 3D with the cathode GDL and current collector ribs enlarged on the right. The shaded area represents the cathode GDL.

The results of the 3D model were compared with those of the 2D model and there were significant differences. The 2D model overestimates the mass transport by natural convection as it does not include the current collector ribs that obstruct the flow. This difference, less than 1%, is not significant for oxygen concentration on the electrode, but for water concentration it is approximately 10%. The 2D model also underestimates the heat transport as the current collector ribs are good heat conductors and increase the surface area of the cell and thus overestimates the temperature in the cell. The temperature difference between the models on the electrode is 6–8 K. The 3D model has a current density that is approximately 4% higher than that of the 2D model.

In this study, a 3D model that could later be used with experiments to optimize free-breathing fuel cell performance was created. However, the optimization is outside the scope of the work done here. This is largely due to the fact that before reliable results can be obtained with this type of modelling, two-

phase equations should be included, which in turn require some experimental work on various parameters. A few brief tests were performed with the model, however, to see the effect of cell size and positioning, i.e., the tilt angle on the performance. The modelled cell area (1 cm^2) was doubled and the current-voltage curves compared. The result was that there was no significant difference in the cell performance, indicating that in this small size range, natural convection is sufficient to provide the cell with reactants and remove reaction products. It was not possible to increase the cell size further with the available computing resources. Different tilt angles were also tested to determine the optimal positioning of the cell. Other related studies such as [85] have indicated that the cell performs best when it is positioned vertically, and this study confirmed these results.

8. Summary and Conclusions

This thesis focused on studying different aspects of PEMFC performance by modelling. These aspects include the dependence of contact resistances on compression and its effect on local cell performance, flow field behaviour in forced convection and free-breathing fuel cells as well as compression distribution in a stack. The modelling was done with Comsol Multiphysics, which uses the finite element method to solve partial differential equations. The results were experimentally validated when possible, although due to the nature of the modelling in this work and the practical limitations, the accuracy of the experimental results was mostly qualitative.

The flow field of the fuel cell cathode was studied by building a model of the cathode channel system. Other cell components such as the GDLs and MEA were excluded as they are very thin layers and would thus have increased the computational requirements too much. Crucially, these components also do not affect the flow field formation, although, in reality, the GDLs that extrude into the channels do affect the flow resistance. The flow field geometry was copied from an existing fuel cell and was a parallel channel system. The parallel channel system has often been seen as an inferior choice due to its tendency to cause uneven flow distribution, resulting in uneven reactant distribution on the electrodes and unsatisfactory cell performance.

In this work, it was shown that a correctly designed parallel channel system can have relatively even flow distributions. The key is to design the distributor channel so that it offers the necessary amount of hydraulic resistance. The distributor channel should be designed individually for each cell or stack depending on the operating conditions and cell size, as flow field behaviour is not scalable. The experiments were qualitatively validated by observing the progress of ink pulses in water flowing through the channel system, which allowed a flow velocity profile to be calculated. The experimental results were in agreement with the

modelling results, but the accuracy of the experiments was not sufficient for quantitative verification.

The effect of contact resistance on cell performance was studied using experimentally derived correlations for the dependency of contact resistance on compression. The compression in a cell varies on the scale of the whole cell and locally. This study focused on local phenomena. There are significant local variations in the compression that GDLs experience due to the alternating ribs and channels of the bipolar plates. Experimental results showed that the contact resistance between the GDL and electrode was especially dependent on the compression. This effect was modelled using a cross-sectional 2D model consisting of one symmetry unit, which was the width of one rib and one channel. This model was built in two phases, published separately, as the original results showed that there was a need for more accurate parameters, which were then acquired from experiments.

The results of contact resistance modelling show that the local current density is far from uniform, as there is a strong lateral current in the electrode layer. This is due to the fact that the contact resistance between the GDL and the electrode is large under the channel, and thus the current created in the electrodes, seeking the path of least resistance, travels through the electrodes until it reaches the portion of the contact boundary under the ribs where the contact resistance is smaller. The most important result is that there is a clear increase in current density in the electrode under the rib/channel boundary, which has not been observed or predicted in fuel cells before. This phenomenon can cause lifetime issues for the cell, although the model does not show a significant effect on the temperature distribution in the cell.

The experimental validation of this model was not performed, as an in-situ experiment to measure local current density would be very difficult to conduct and was not possible within the scope of this thesis. If, however, a way could be devised to perform these measurements, the results have the potential to be very interesting. It is known that membranes can develop small punctures, especially under high compression, temperature or current density, and it is possible that this lateral current mechanism and the ohmic heating it causes have an effect on this failure type. If so, the effect could possibly be mitigated by studying different rib profiles and GDL properties by modelling in order to decrease the lateral current density in the electrodes. It is possible that altering the cross-sectional shape of the rib from a square edge to a more rounded shape would have a beneficial effect, and this should be investigated.

The compression distribution in a stack was also studied. A model of a 5-cell stack was built based on an existing design. According to the model, the compression directed at the cells was highly uneven, with the corners of the active area under high compression and the centre parts experiencing less than 2 bars of compression pressure. This can be considered less than optimal as, according to other studies, good cell performance requires 10–15 bars of compression, though this value depends on the GDL material. Thus, the stack end plates were redesigned using a ribbed structure that allowed the mass of the end plates to be decreased while simultaneously increasing their rigidity. A further mass decrease was accomplished by changing the end plate material from steel to aluminium. The force applied to the nuts and bolts of the end plates was varied so that the corners had less torque, which also helped to even the compression distribution. The end result was that the new end plate and the bolt-specific forces produced the desired compression distribution in the 10–15 bar range. The model was experimentally validated by ex-situ measurements using a pressure-sensitive film. The measurement accuracy of the experiments suffered from high manufacturing tolerance of the cell components, but qualitatively the results are in agreement.

The results of the compression distribution study demonstrate that stack endplates need to be designed with care or the compression on the cells can be far from optimal, thus affecting the cell performance negatively. Modelling is an effective tool for determining an acceptable end plate structure. The compression modelling in this work has been continued by others. The model has been developed further employing thin, perforated flexible layers to even out the compression further. Thermal stresses were also included, although these were found to be insignificant. In the future, this model could be improved by adding more geometrical details and increasing the number of cells as the available computing capacity is increased.

The flow field of a free-breathing fuel cell was also modelled in this work. The performance of a free-breathing fuel cell depends strongly on the effectiveness of the natural convection in transferring oxygen to the cell and removing the reaction product water. This problem has been modelled using various assumptions and simplifications. In this work, the aim was to develop a computationally light yet reliable 3D model of a free-breathing fuel cell and then to use it to demonstrate the potential of such a model. Modelling the flow field of a free-breathing fuel cell is different to making the usual cell model, as the ambient air zone has to be included. This increases the size of the model and thus requires

more computing power. In order to find out how large the modelled ambient air zone should be, different sized zones with different types of boundary conditions were tested in 2D. These results were used in the building of a 3D model of a small 1 cm^2 cell. This model was then used to test how the position, i.e., tilt angle, of the cell and doubling the cell size affected performance. The results were that, as experiments have shown, a vertical alignment works best and increasing the cell size has no significant effect on its performance in this size range, though it can be expected that, at some point, increasing the cell size will create mass transport problems when the natural convection is no longer sufficient.

Mass transport was also modelled in the case of a free-breathing fuel cell. The model consisted of the cathode GDL and current collectors of the cell and the ambient air zone surrounding the cell. The model was 3D, but suitable boundary conditions and the correct size of the ambient air zone were first studied using a 2D model. The 3D model, built using the data from the 2D model, is computationally lighter than the free-breathing PEMFC models typically used but no less accurate. This model was used to perform some preliminary tests on the effect of the size and positioning of the cell on its performance. The result was that when the size of the cell is in the range of a few square centimetres, natural convection is effective in supplying the cell with reactants, and increasing the cell size does not have a strong effect on the cell behaviour.

The flow field and the model of the free-breathing fuel cell require the inclusion of two-phase phenomena to give good predictions however. At the time of writing this thesis, there simply are no reliable parameters for modelling two-phase phenomena in fuel cells. Even if the parameters widely used in fuel cell modelling were to be incorporated into this model, there would still be a problem of how to model the two-phase phenomena on the GDL/ambient air zone boundary where evaporation takes place. Excess water can also form droplets on this surface. In order to develop free-breathing fuel cell models or fuel cell models in general, further, reliable two-phase parameters should be derived either experimentally or theoretically, and suitable boundary conditions, semi-empirical correlations if necessary, should be developed.

This thesis is a study of different aspects of fuel cell operation connected together by the method of using modelling as a tool. As always in modelling, each model could have been developed further, but the line must be drawn somewhere and the length and depth of this work were determined by the practical constraints of each project of which the studies were made a part. In terms of future work, the most important improvements would be to add geometrical

details and complexity to the stack models and two-phase phenomena to the cell models. If computing capacity continues to increase, as it has done in the past, it will be possible one day to develop a model that combines most of the models in this study. This model would consist of the GDLs, MEA and flow channels of an entire cell and include contact resistance effects combined with flow field simulation and the results of a stack compression model. This model could show what kind of current density or thermal distribution the combined effect of local cell phenomena and cell-scale variations in reactant concentration and compression would cause in a fuel cell.

References

[1] http://www.epsomandewellhistoryexplorer.org.uk/Schonbein.html, last referred to on 16.11.2010

[2] F. Barbir, PEM Fuel Cells: Theory and Practise, Elsevier (2005)

[3] http://aboutfuelcells.wordpress.com/2007/06/04/ludwig-mond-and-charles-langer, last referred to on 16.11.2010

[4] http://www.ieeeghn.org/wiki/index.php/Bacon's_Fuel_Cell, last referred to on 16.11.2010

[5] http://www.fctec.com/fctec_history.asp, last referred to on 16.11.2010

[6] http://en.wikipedia.org/wiki/Gemini_V, last referred to on 16.11.2010

[7] Smithsonian institute http://scienceservice.si.edu/pages/059026.htm, last referred to on 4.12.2009

[8] http://www.hydrogencarsnow.com/blog2/index.php/hydrogenbus es/bc-transit-fuel-cell-buses-in-operation-for-2010-winter-olympics/, last referred to on 14.4.2011

[9] European Union, Fuel Cells and Hydrogen Joint Technology Initiative, http://ec.europa.eu/research/fch/index_en.cfm?pg=back, last referred to on 1.2.2010

[10] G. Meng, G. Ma, Q. Ma, R. Peng and X. Liu, Ceramic membrane fuel cells based on solid proton electrolytes, *Solid State Ionics* 178, pp. 697–703 (2007)

[11] W. Dai, H. Wang, X. Yuan, J.J. Martin, D. Yang, J. Qiao and J. Ma, A review on water balance in the membrane electrode assembly of proton exchange membrane fuel cells, *Int. J. Hydrogen Energy* 34, pp. 9461–9478 (2009)

[12] M.S. Wilson, F.H. Garzon, K.E. Sickafus and S. Gottesfeld, Surface area loss of supported platinum in polymer electrolyte fuel cells, *J. Electrochem. Soc.* 140, pp. 2872–2877 (1993)

[13] X. Cheng, L. Chen, C. Peng, Z. Chen, Y. Zhang and Q. Fan, Catalyst microstructure examination of PEMFC membrane electrode assemblies vs. time, *J. Electrochem. Soc.* 151, pp. A48–A52 (2004)

[14] D.A. Stevens and J.R. Dahn, Thermal degradation of the support in carbon-supported platinum electrocatalysts for PEM fuel cells, *Carbon* 43, p. 179 (2005)

[15] A. Collier, H. Wang, X.Z. Yuan, J. Zhang and D.P. Wilkinson, Degradation of polymer electrolyte membranes, *Int. J. Hydrogen Energy* 31, p. 1838 (2006)

[16] J. Xie, D.L. Wood, D.M. Wayne, T.A. Zawodzinski, P. Atanassov and R.L. Borup, Durability of PEFCs at high humidity conditions, *J. Electrochem. Soc.* 152, p. A104 (2005)

[17] C. Chung, L. Kim, Y.W. Sung, J. Lee and J.S. Chung, Degradation mechanism of electrocatalyst during long-term operation of PEMFC, *Int. J. Hydrogen Energy* 34, pp. 8974–8981 (2009)

[18] E. Endoh, S. Terazono, H. Widjaja and Y. Takimoto, Degradation study of MEA for PEMFCs under low humidity conditions, *Electrochem. Solid-State Lett.* 7, pp. A209–A211 (2004)

[19] J. Xie, D.L. Wood, III, K.L. More, P. Atanassov and R.L. Borup, Microstructural Changes of Membrane Electrode Assemblies during PEFC durability testing at high humidity conditions, *J. Electrochem. Soc.* 152, pp. A1011–A1020 (2005)

[20] X.L. Wang, H.M. Zhanga, J.L. Zhang, H.F. Xu, Z.Q. Tian, J. Chen, H.X. Zhong, Y.M. Liang and B.L. Yi, Micro-porous layer with composite carbon black for PEM fuel cells, *Electrochimica Acta* 51, pp. 4909–4915 (2006)

[21] H. K. Atiyeh, K. Karan, B. Peppley, A. Phoenix, E. Halliop and J. Pharoah, Experimental investigation of the role of a microporous layer on the water transport and performance of a PEM fuel cell, *J. Power Sources* 170, pp. 111–121 (2007)

[22] M.H. Oha, Y.S. Yoon and S.G. Park, The electrical and physical properties of alternative material bipolar plate for PEM fuel cell system, *Electrochimica Acta* 50, Pp. 777–780 (2004)

[23] C. Hui, L. Hong-bo, Y. Li, L. Jian-xin and Y. Li, Study on the preparation and properties of novolac epoxy/graphite composite bipolar plate for PEMFC *Int. J. Hydrogen Energy* 35, pp. 3105–3109 (2010)

[24] E.A. Cho, U.-S. Jeon, S.-A. Hong, I-H. Oh and S.-G. Kang, Performance of a 1 kW-class PEMFC stack using TiN-coated 316 stainless steel bipolar plates, *J. Power Sources* 142, pp. 177–183 (2005)

[25] K. Lee, S. Lee, J. Kim, Y. Lee, Y. Kim, M. Kim and D. Wee, Effects of thermal oxi-nitridation on the corrosion resistance and electrical conductivity of 446M stainless steel for PEMFC bipolar plates, *Int. J. Hydrogen Energy* 34, pp. 1515–1521 (2009)

[26] S. Joseph, J.C. McClure, R. Chianelli, P. Pich and P.J. Sebastian, Conducting polymer-coated stainless steel bipolar plates for proton exchange membrane fuel cells (PEMFC), *Int. J. Hydrogen Energy* 30, pp. 1339–1344 (2005)

[27] J. Chen, Experimental study on the two phase flow behavior in PEM fuel cell parallel channels with porous media inserts, *J. Power Sources* 195, pp. 1122–1129 (2010)

[28] D.G. Strickland and J.G. Santiago, In situ polymerized wicks for passive water management in PEM fuel cells, *J. Power Sources* 195, pp. 1667–1675 (2010)

[29] J.S. Yi and T.V. Nguyen, Multicomponent transport in porous electrodes of proton exchange membrane fuel cells using the interdigitated gas distributors, *J. Electrochem. Soc.* 146, pp. 38–45 (1999)

[30] A. Kazim, H.T. Liu and P. Forges, Modelling of performance of PEM fuel cells with conventional and interdigitated flow fields, *J. Appl. Electrochem.* 29, pp. 1409–1416 (1999)

[31] A. Kumar and R.G. Reddy, Effect of channel dimensions and shape in the flow-field distributor on the performance of polymer electrolyte membrane fuel cells, *J. Power Sources* 113, pp. 11–18 (2003)

[32] H. Meng and C.Y. Wang, Large-scale simulation of polymer electrolyte fuel cells by parallel computing, *Chem Eng Sci* 59, pp. 3331–3343 (2004)

[33] Y. Yoon, W. Lee, G. Park, T. Yang and C. Kim, Effects of channel configurations of flow field plates on the performance of a PEMFC, *Electrochimica Acta* 50, pp. 709–712 (2004)

[34] S. Shimpalee and J.W. Van Zee, Numerical studies on rib & channel dimension of flow-field on PEMFC performance, *Int. J. Hydrogen Energy* 32, pp. 842–856 (2007)

[35] S.A. Vilekar and R. Datta, The effect of hydrogen crossover on open-circuit voltage (OCV) in PEM fuel cells, *J. Power Sources*, Accepted Manuscript (2009)

[36] M. Andersson, J. Yuan and B. Sundén, Review on modeling development for multiscale chemical reactions coupled transport phenomena in solid oxide fuel cells, *Applied Energy* 87, pp. 1461–1476 (2010)

[37] M.G. Santarelli, M.F. Torchio and P. Cochis, Parameters estimation of a PEM fuel cell polarization curve and analysis of their behavior with temperature, *J. Power Sources* 159, pp. 824–835 (2006)

[38] N. Djilali, Computational modelling of polymer electrolyte membrane (PEM) fuel cells, Challenges and opportunities, *Energy* 32, pp. 269–280 (2007)

[39] R. Madhusudana Rao and R. Rengaswamy, Dynamic characteristics of spherical agglomerate for study of cathode catalyst layers in proton exchange membrane fuel cells (PEMFC), *J. Power Sources* 158, pp. 110–123 (2006)

[40] D. Cheddie and N. Munroe, Review and comparison of approaches to proton exchange membrane fuel cell modelling, *J. Power Sources* 147, pp. 72–84 (2005)

[41] C. Siegel, Review of computational heat and mass transfer modeling in polymer-electrolyte-membrane (PEM) fuel cells, *Energy* 33, pp. 1331–1352 (2008)

[42] F. Standaert, K. Hemmes and N. Woudstra, Analytical fuel cell modeling, *J. Power Sources* 63, pp. 221–234 (1996)

[43] D. Bernardi and M. Verbrugge, A mathematical model of the solid polymer electrolyte fuel cell, *J. Electrochem. Soc.* (1992)

[44] M. Khakpour and K. Vafai, Analysis of transport phenomena within PEM fuel cells – An analytical solution, *Int. J. Heat and Mass Transfer* 51, pp. 3712–3723 (2008)

[45] D.F. Cheddie and N.D.H. Munroe, Semi-analytical proton exchange membrane fuel cell modelling, *J. Power Sources* 183, pp. 164–173 (2008)

[46] T.E. Springer, T.A. Zawodzinski and S. Gottesfeld, Polymer electrolyte fuel cell model, *J. Electrochem. Soc.* 138, pp. 2334–2342 (1991)

[47] H. Huisseune, A. Willockx and M. De Pepe, Semi-empirical along-the-channel model for a proton exchange membrane fuel cell, *Int. J. Hydrogen Energy* 33, pp. 6270–6280 (2008)

[48] L. Pisani, G. Murgia, M. Valentini and B. D'Aguanno, A new semi-empirical approach to performance curves of polymer electrolyte fuel cells, *J. Power Sources* 108, pp. 192–203 (2002)

[49] M.A.R. Sadiq Al-Baghdadi, Modelling of proton exchange membrane fuel cell performance based on semi-empirical equations, *Renewable Energy* 30, pp. 1587–1599 (2005)

[50] T.E. Springer, T.A. Zawodzinski and S. Gottesfeld, Polymer electrolyte fuel cell model, *J Electrochem Soc* 138, pp. 2334–2342 (1991)

[51] D.M. Bernardi and M.W. Verbrugge, Mathematical model of a gas diffusion electrode bonded to a polymer electrolyte, *AIChE J.* 37, pp. 1151–1163 (1991)

[52] D. Singh, D. Lu and N. Djilali, A two-dimensional analysis of mass transport in proton exchange membrane fuel cells, *Int. J. Eng. Sci* 37, pp. 431–452 (1999)

[53] T.V. Nguyen and R.E. White, A water and heat management model for proton-exchange-membrane fuel cells. *J. Electrochem. Soc.* 140, pp. 2178–2186 (1993)

[54] S. Dutta, S. Shimpalee and J.W. van Zee, Three-dimensional numerical simulation of straight channel PEM fuel cells, *J Appl Electrochem* 30, pp. 135–146 (2000)

[55] S. Dutta, S. Shimpalee and J.W. van Zee, Numerical prediction of mass-exchange between cathode and anode channels in a PEM fuel cell, *Int J Heat Mass Transfer* 44, pp. 2029–2042 (2001)

[56] T. Berning, D.M. Lu and N. Djilali, Three-dimensional computational analysis of transport phenomena in PEM fuel cells, *J Power Sources* 106, pp. 284–294 (2002)

[57] A. Kumar and R.G. Reddy, Effect of the channel dimensions and shape in the flow field distributor on the performance of polymer electrolyte membrane fuel cells, *J Power Sources* 113, pp. 11–18 (2003)

[58] G. Mmaranzana, C. Moyne, J. Dillet, S. Didierjean and O. Lottin, About internal currents during start-up in PEMFC, *J. Power Sources* 195, pp. 5990–5995 (2010)

[59] P.R. Pathapati, X. Xue and J. Tang, A new dynamic model for predicting transient phenomena in a PEM fuel cell system, *Renewable Energy* 30, pp. 1–22 (2005)

[60] N. Wagner, Characterization of membrane electrode assemblies in polymer electrolyte fuel cells using a.c. impedance spectroscopy, *J. App. Electrochem.* 32, pp. 859–863 (2002)

[61] T.-W. Lee, J. Hur, B.-K. Lee and C.-Y. Won, Design of a fuel cell generation system using a PEMFC simulator, *Electric Power Systems Research* 77, pp. 1257–1264 (2007)

[62] M. Ceraolo, C. Miuli and A. Pozio, Modelling static and dynamic behaviour of proton exchange membrane fuel cells on the basis of the electro-chemical description, *J. Power Sources* 113, pp. 131–144 (2003)

[63] S. Yerramalla, A. Davari, A. Feliachi and T. Biswas, Modeling and simulation of the dynamic behavior of a polymer electrolyte membrane fuel cell, *J. Power Sources* 124, pp. 104–113 (2003)

[64] Z.H. Wang, C.Y. Wang and K.S. Chen, Two-phase flow and transport in the air cathode of proton exchange membrane fuel cells, *J. Power Sources* 94, 15, pp. 40–50 (2001)

[65] L. You and H. Liu, A two-phase flow and transport model for the cathode of PEM fuel cells, *Int. J. Heat and Mass Transfer* 45, pp. 2277–2287 (2002)

[66] U. Pasaogullari and C. Wang, Two-phase modeling and flooding prediction of polymer electrolyte fuel cells, *J. Electrochem. Soc.* 152, pp. A380–A390 (2005)

[67] D. Natarajan and T.V. Nguyen, A two-dimensional, two-phase, multicomponent, transient model for the cathode of a proton exchange membrane fuel cell using conventional gas distributors, *J. Electrochem. Soc.* 148, pp. A1324–A1335 (2001)

[68] T. Berning, D.M. Lu and N. Djilali, Three-Dimensional Computational Analysis of Transport Phenomena in a PEM Fuel Cell, *J. Power Sources* 106, pp. 284–294 (2002)

[69] T. Kim, J. Kim, C. Sim, S. Lee, M. Kaviany, S. Young Son and M. Kim, Experimental approaches for distribution and behavior of water in PEMFC under flow direction and differential pressure using neutron imaging technique, *Nuclear Instruments and Methods in Physics Research Section A: Accelerators, Spectrometers, Detectors and Associated Equipment* 600. Pp. 325–327 (2009)

[70] C. Min, A novel three-dimensional, two-phase and non-isothermal numerical model for proton exchange membrane fuel cell, *J. Power Sources* 195, pp. 1880–1887 (2009)

[71] T. Ous and C. Arcoumanis, Visualisation of water droplets during the operation of PEM fuel cells, *J. Power Sources* 173, pp. 137–148 (2007)

[72] T. Berning, M. Odgaard and S.K. Kær1, A Computational Analysis of Multiphase Flow Through PEMFC Cathode Porous Media Using the Multifluid Approach, *J. Electrochem. Soc.* 156, pp. B1301–B1311 (2009)

[73] V. Gurau, T.A. Zawodzinski Jr., J.A. Mann Jr., Two-phase transport in PEM fuel cell cathodes, *J. Fuel Cell Sci. Technol.* 5, (2008)

[74] S. Larsson and V. Thomée, Partial Differential Equations with Numerical Methods, Springer (2005)

[75] R. Taylor and R. Krishna, Multicomponent mass transfer, Wiley (1993)

[76] N. Akhtar, A. Qureshi, J. Scholta, C. Hartnig, M.S. Messerschmidt and W. Lehnert, Investigation of water droplet kinetics and optimization of channel geometry for PEM fuel cell cathodes, *Int. J. of Hydrogen Energy* 34, pp. 3104–3111 (2009)

[77] J. Scholta, G. Escher, W. Zhang, L. Küppers, L. Jörissen and W. Lehnert, Investigation on the influence of channel geometries on PEMFC performance, *J. Power Sources* 155, pp. 66–71 (2006)

[78] G. He, Y. Yamazaki, and A. Abudula, A droplet size dependent multiphase mixture model for two phase flow in PEMFCs, *J. Power Sources* 194, pp. 190–198 (2009)

[79] X. Li and I. Sabir, Review of bipolar plates in PEM fuel cells: Flow-field designs, *Int. J. Hydrogen Energy* 30, pp. 359–371 (2005)

[80] J. Ihonen, F. Jaouen, G. Lindbergh and G. Sundholm, A novel polymer electrolyte fuel cell for laboratory investigations and in-situ contact resistance measurements, *Electrochim. Acta* 46, pp. 2899–2911 (2001)

[81] V. Mishra, F. Yang and R. Pitchumani, Measurement and prediction of electrical contact resistance between gas diffusion layers and bipolar plate for applications to PEM fuel cells, *J. Fuel Cell Sci. Technol.* 1, pp. 2–9 (2004)

[82] I. Nitta, T. Hottinen, O. Himanen and M. Mikkola, Inhomogeneous compression of PEMFC gas diffusion layer. Part I. Experimental, *J. Power Sources* 171, pp. 26–36 (2007)

[83] I. Nitta, O. Himanen and M. Mikkola, Contact resistance between gas diffusion layer and catalyst layer of PEM fuel cell, *Electrochem. Comm.* 10, pp. 47–51 (2008)

[84] J. Ihonen, M. Mikkola and G. Lindbergh, Flooding of Gas Diffusion Backing in PEFCs, *J. Electrochem. Soc.* 151, pp. A1152–A1161 (2004)

[85] S. Escribano, J.-F. Blachot, J. Ethève, A. Morin and R. Mosdale, Characterization of PEMFCs gas diffusion layers properties, *J. Power Sources* 156, pp. 8–13 (2006)

[86] W. Lee, C.-H. Ho, J.W. Van Zee and M. Murthy, The effects of compression and gas diffusion layers on the performance of a PEM fuel cell, *J. Power Sources* 84, pp. 45–51 (1999)

[87] M. Mikkola, T. Tingelöf and J. Ihonen, Modelling compression pressure distribution in fuel cell stacks, *J. Power Sources* 193, pp. 269–275 (2009)

[88] M. Mikkola and P. Koski, Modeling the internal pressure distribution of a fuel cell, *COMSOL Conference 2009, Milan, Italy, October 14–16, 2009*, Proceedings of the Comsol Conference (2009)

[89] S. Litster, J.G. Pharoah, G. McLeana and N. Djilali, Computational analysis of heat and mass transfer in micro-structured PEMFC cathode, *J. Power Sources* 156, pp. 334–344 (2006)

[90] P. Manoj Kumar and A.K. Kolar, Effect of cathode design on the performance of an air-breathing PEM fuel cell, *J. Power Sources* 35, pp. 671–681 (2010)

[91] M. Havet and D. Blay, Natural convection over a non-isothermal vertical plate, *Int. J. Heat and Mass Transfer* 42, pp. 3103–3112 (1999)

[92] S. Pretot, B. Zeghmati and G. Le Palec, Theoretical and experimental study of natural convection on a horizontal plate, *Applied Thermal Engineering* 20, pp. 873–891 (2000)

Appendix A: Parameter Correlations and Constants

Parameter Correlations

Parameter name	Equation	Publi-cation
Heat production rate	$q_0 = i\left(\eta + \frac{326T}{4F}\right)\cdot 0.8$	5
Water production rate	$\dot{\mathbf{N}}_{H2O} = -\frac{i}{2F} M_{H2O}$	1,2,3,5
Oxygen consumption rate	$\dot{\mathbf{N}}_{O2} = \frac{i}{4F} M_{O2}$	1,2,3,5
Reynold's number	$\mathrm{Re} = \frac{\rho u D_h}{\eta}$	1
Effective diffusion coefficient	$D^{\mathrm{eff}} = D(\varepsilon(1-s))^{1.5}$	2,3,5
Average density of air	$\rho(s) = \frac{(p_{\mathrm{atm}} + p)(M_{\mathrm{H_2O}} x_{\mathrm{H_2O}}(s) + M_{\mathrm{O_2}} x_{\mathrm{O_2}}(s) + M_{\mathrm{N_2}} x_{\mathrm{N_2}} + M_{\mathrm{Ar}} x_{\mathrm{Ar}})}{RT}$	1,2,3,5
Average viscosity of air	$\eta_{air}(s) = \left(\frac{x_{\mathrm{H_2O}}(s)}{\eta_{\mathrm{H_2O}}} + \frac{x_{\mathrm{O_2}}(s)}{\eta_{\mathrm{O_2}}} + \frac{x_{\mathrm{N_2}}}{\eta_{\mathrm{N_2}}} + \frac{x_{\mathrm{Ar}}}{\eta_{\mathrm{Ar}}}\right)^{-1} \cdot \frac{\rho(s)}{\rho_{\mathrm{in}}}$	1,2,3,5
Binary diffusion coefficients	$D_{ij} = C\frac{T^{1.75}\sqrt{1/M_i + 1/M_j}}{p\left((v_i)^{1.3} + (v_j)^{1.3}\right)^2}$ or alternatively $D_{i,j} = \frac{p_0}{p}\left(\frac{T}{T_0}\right)^{1.5} D_{i,j}(p_0, T_0)$	1,2,3,5

Heat production in the cell	$q_0 = i\left(\eta_c + \frac{326T}{4F}\right)\cdot 0.8$	5
Exchange current density on the cathode	$i_0(T) = i_0(T_0)\exp\left(-\frac{\Delta E}{R}\left(\frac{1}{T}-\frac{1}{T_0}\right)\right)$	5
Saturation molar fraction	$X_{sat} = \frac{p_{sat}}{p}$	1,2,3
Saturation pressure	$\log(p_{sat}) = 28.59051 - 8.2\log(T+0{,}01) + 0.0024804(T+0.01) - 3142.31/(T+0.01)$	1,2,3
Maxwell–Stefan diffusion coefficients	$D_{11} = D_{O_2,N_2}\frac{X_{O_2}D_{H_2O,N_2} + (1-X_{O_2})D_{O_2,H_2O}}{S}$ $D_{12} = X_{O_2}D_{H_2O,N_2}\frac{D_{O_2,N_2} - D_{O_2,H_2O}}{S}$ $D_{21} = X_{H_2O}D_{O_2,N_2}\frac{D_{H_2O,N_2} - D_{O_2,H_2O}}{S}$ $D_{22} = D_{H_2O,N_2}\frac{X_{H_2O}D_{O_2,N_2} + (1-X_{H_2O})D_{O_2,H_2O}}{S}$ $S = X_{O_2}D_{H_2O,N_2} + X_{H_2O}D_{O_2,N_2} + X_{N_2}D_{O_2,H_2O}$	1,2,3,5

Constants

The properties of dry standard air used in Publications 1, 2, 3 and 5

Component	*Molar mass* ($gmol^{-1}$)	*Molar fraction in air*	*Viscosity η at 343 K (Pas)*	*Density ρ at 343 (K kgm^{-3})*	*Diffusion volume v (m^3mol^{-1})*
Nitrogen	28	0.78	$1.97\cdot10^{-5}$	0.995	$12.7\cdot10^{-6}$
Oxygen	32	0.21	$2.29\cdot10^{-5}$	1.137	$16.6\cdot10^{-6}$
Argon	40	0.1	$2.60\cdot10^{-5}$	1.421	-
Water	18	0	$1.15\cdot10^{-5}$	0.64	$17.9\cdot10^{-6}$

The mechanical properties of materials used in Publication 4

Component	*E (GPa)*	*υ*
Flow field plate (graph/epoxy)	10	0.25
Gas diffusion layer	0.06	0.33
Grafoil	1.4	0.25
Steel	200	0.33
Aluminium	70	0.33
Rubber	0.1	0.4
Steel net	110	0.33

Various constants used in the models

Constant	*Explanation*	*Value*
$a_v j_a^{ref}$	Exchange current density × ratio of reaction surface to CL volume, anode (2D)	1.7×10^9 A m^{-3}
$a_v j_c^{ref}(T_0)$	Exchange current density × ratio of reaction surface to CL volume, cathode (2D)	2×10^4 A m^{-3}
$\alpha_a^a + \alpha_c^a$	Anodic and cathodic transfer coefficients	1
α	Water transfer coefficient	0.5
C_{p,O_2}	Heat capacity of oxygen	923 J kg^{-1} K^{-1}
C_{p,H_2O}	Heat capacity of water	1996 J kg^{-1} K^{-1}
c_p	Heat capacity of air	1005.38007 J/kg K
c_{cc}	Heat capacity of the current collector	1000 J/kg K
C	Diffusion coefficient constant	$3.16 \cdot 10^{-8}$
$c_{O2,0}$	Oxygen concentration in ambient air	8.39128 mol/m^3
c_{H2O0}	Water concentration in ambient air	0.403621 mol/m^3
$D_{O_2,H_2O}(p_0,T_0)$	Binary diffusion coefficient O_2,H_2O	3.98×10^{-5} m^2 s$^-$
$D_{O_2,N_2}(p_0,T_0)$	Binary diffusion coefficient O_2,N_2	2.95×10^{-5} m^2 s^{-1}
$D_{H_2O,N_2}(p_0,T_0)$	Binary diffusion coefficient H_2O,N_2	4.16×10^{-5} m^2 s^{-1}

E_0	Open circuit voltage	1.23 V
ΔE_{exc}	Activation energy	($E_{cell} \geq 0.8V$) 76.5 kJ mol^{-1} ($E_{cell} < 0.8V$) 27.7 kJ mol^{-1}
ε_0	Porosity of uncompressed GDL	0.83
ε_{CL}	Porosity of CL	0.4
η_c	Activation overpotential	0.6 V
F	Faraday's constant	96485 C/mol
g	Gravitational acceleration	9.81 m/s^2
$i_0(T_0)$	Exchange current density	0.01 A/m^2
k	Heat conductivity of air	0.026044 J/m^2
k_{GDL}	Effective heat conductivity of the GDL	0.3 W/m
κ_{CL}	CL thermal conductivity	0.476 W m^{-1} K^{-1}
κ_{GDL}	GDL thermal conductivity	1.18
k_{cc}	Thermal conductivity of the current collector	14 J/m^2
κ	GDL permeability	$2.06 \cdot 10^{-12}$ m^2
σ_{GR}	Graphite plate electric conductivity	69700 S m^{-1}
κ_{GR}	Graphite plate thermal conductivity	128 W m^{-1} K^{-1}
σ_m	Membrane ionic conductivity	5.09 S m^{-1}
κ_m	Membrane thermal conductivity	0.12 W m^{-1} K^{-1}
κ_h	Heat transfer coefficient from GDL to air	5 W m^{-2} K^{-1}
k_{CL}	Permeability of CL	1.26×10^{-13} m^2
p_0	Ambient pressure	10^5 Pa
R	Universal gas constant	8.314 J/mol K
ΔS_c	Entropy change of cathode	326.36 J mol^{-1} K^{-1}
ΔS_a	Entropy change of anode	0.104 J mol^{-1} K^{-1}
σ_s^{CL}	CL electric conductivity	320 S m^{-1}
σ_m^{CL}	CL ionic conductivity	5.09 S m^{-1}
T_0	Reference temperature	273 K

Appendix B: Publications 1–5

PUBLICATION 1

Modeling of flow field in polymer electrolyte membrane fuel cell

In: Journal of Power Sources 161(2), pp. 876–884.

Available online at www.sciencedirect.com
ScienceDirect
Journal of Power Sources 161 (2006) 876–884
JOURNAL OF POWER SOURCES
www.elsevier.com/locate/jpowsour

Modeling of flow field in polymer electrolyte membrane fuel cell

Suvi Karvonen [a] *, Tero Hottinen [a], Jaakko Saarinen [b], Olli Himanen [a]

[a] *Helsinki University of Technology, Laboratory of Advanced Energy Systems, P.O. Box 2200, FIN-02015 TKK, Finland*
[b] *VTT Technical Research Centre of Finland, P.O. Box 1601, FI-02044 VTT, Finland*

Received 8 November 2005; received in revised form 7 March 2006; accepted 30 April 2006
Available online 23 June 2006

Abstract

Isothermal two- and three-dimensional polymer electrolyte membrane (PEM) fuel cell cathode flow field models were implemented to study the behavior of reactant and reaction product gas flow in a parallel channel flow field. The focus was on the flow distribution across the channels and the total pressure drop across the flow field. The effect of the density and viscosity variation in the gas resulting from the composition change due to cell reactions was studied and the models were solved with governing equations based on three different approximations. The focus was on showing how a uniform flow profile can be achieved by improving an existing channel design. The modeling results were verified experimentally. A close to uniform flow distribution was achieved in a parallel channel system.

Keywords: PEM fuel cell; PEMFC; Modeling; Flow field plate; Parallel channel; Flow visualization

1. Introduction

Fuel cell is an electrochemical device that converts the chemical energy of reactants into electricity and heat. Fuel cells typically have comparatively high efficiencies and energy densities, in addition to which they have potential as economically friendly power sources. Their properties make them alternative power sources for many applications ranging from portable electronics and vehicles to distributed energy production and power plants. In this study the focus is on the polymer electrolyte membrane fuel cell (PEMFC), but the results can also be applied to other fuel cell types. The PEM fuel cell operates in the temperature range of liquid water, though higher temperature PEM fuel cells are also being developed. PEMFC is in particular suitable for small-scale applications ranging from less than a watt to several kilowatts.

One of the requirements for good cell performance is that the reactants must be distributed as uniformly as possible across the active area of the cell. This is especially important on the cathode side, where the reaction kinetics is comparatively slow and thus forms one of the major performance limiting factors in a PEMFC, the cathode mass transfer overpotential. A non-uniform flow distribution results in a non-uniform reactant distribution, leading to insufficient amounts of reactants on some areas and inhomogeneous current production. In addition to having an adverse effect on cell performance, this can lead to temperature gradients across the active area of the cell, a phenomenon that in an extreme case may damage the membrane. The flow distribution properties also affect the water removal from the cell, and thus a non-uniform flow distribution can cause flooding in the cell.

In a fuel cell stack, the reactant flow is typically directed to each unit cell with a component known as the flow field plate, which also functions as a mechanical support structure and an electrical contact. The flow field plate directs the gas flow into the gas diffusion layer through a channel system, usually molded, etched or machined on the surface of the plate. The flow distribution in the channel system is determined by the relative hydraulic resistances of the channel system. The most common channel configurations are the parallel, serpentine and interdigitated configurations and their combinations, studied in, e.g. [1–9]. The channel system can also be replaced with a porous metal net or foam plate, see, e.g. [10]. The parallel channel configuration, which was studied in this work, typically has a small hydraulic resistance and thus does not generate a large pressure drop across the cell. On the other hand, the parallel channel flow field often has a non-uniform flow distribution and is thus more susceptible to flooding, as many authors have concluded; see, e.g. [5,6,9].

* Corresponding author. Tel.: +358 9 451 3209; fax: +358 9 451 3195.
E-mail address: Suvi.Karvonen@hut.fi (S. Karvonen).

0378-7753/$ – see front matter © 2006 Elsevier B.V. All rights reserved.
doi:10.1016/j.jpowsour.2006.04.145

Nomenclature

A	area (m^2)
D	diffusion coefficient ($m^2\ s^{-1}$)
D_h	hydraulic diameter (m)
e	unit charge (1.6022×10^{-19} C)
F	Faraday's constant ($96485\ C\ mol^{-1}$)
g	gravitational acceleration ($9.8067\ m\ s^{-2}$)
i	current density ($A\ m^{-2}$)
L	characteristic length (m)
M	molar mass ($kg\ mol^{-1}$)
n	surface normal vector
N	number
N_A	Avogadro's constant ($6.022169 \times 10^{23}\ mol^{-1}$)
p	pressure (Pa)
p_0	atmospheric pressure (101.315 kPa)
R	molar gas constant ($8.315\ J\ mol^{---1}\ K^{-1)}$
Re	Reynolds number
s	distance (m)
S_{con}	source term for continuity equation ($kg\ m^{-3}\ s^{-1}$)
$\mathbf{S}_{NS}$	source term for Navier–Stokes equation ($kg\ m^{-2}\ s^{-2}$)
Sh	Sherwood number
t	surface tangential vector
T	temperature (K)
u	total velocity of the fluid ($m\ s^{-1}$)
u	fluid velocity vector ($m\ s^{-1}$)
u_0	inlet velocity ($m\ s^{-1}$)
U	characteristic velocity ($m\ s^{-1}$)
V	volume (m^3)
V_m	molar volume in 343 K ($0.0278\ m^3\ mol^{-1}$)
x	molar fraction
z	number of electrons involved in a reaction

Greek symbols

α	water transport coefficient
Δ	surface roughness (m)
ε	porosity
η	dynamic viscosity (Pas)
λ	stoichiometric constant, 2
ρ	density ($kg\ m^{-3}$)

Subscripts and superscripts

act	active area
air	air
atm	atmospheric
ave	average
Ar	argon
ch	channel
cath	cathode
eff	effective
H_2O	water
in	inlet
lim	limiting
max	maximum
N_2	nitrogen
O_2	oxygen
react	reaction participant
sat	saturated vapor
tot	total
v	vapor

However, these problems can at least partially be avoided with careful design of the flow field system. A uniform flow distribution achieved with the parallel channel system is presented in this work. Consequently, the main result of this work is to show by example that uniform flow distributions can be achieved with parallel channel flow fields with relatively slight changes in the flow field design.

The flow distributions and pressure losses across the channel systems were studied with both two- and three-dimensional one-phase models based on the Navier–Stokes and continuity equations. The changes in the gas density and viscosity along the channels that result from the cell reactions were taken into account in the modeling. The cathode distribution was studied according to three different approximations and the corresponding results were compared in order to find out the error induced by each approximation.

The modeling data and experimental results showed the flow distribution of the original three-dimensional parallel channel system to be polarized. Based on the results, the local hydraulic resistances of the channel system were adjusted through modification of the gas distributor channel. As a result, the modeled polarization was reduced and a close to uniform flow profile was achieved. The modeling results were also experimentally verified and the experimental results were in agreement with the modeling data.

2. Modeling

2.1. Navier–Stokes and continuity equations

The modeling domains consisted of the volume in 3D and cross-sectional area in 2D of the modeled channel systems. Other fuel cell components such as the gas diffusion layer and the membrane electrode assembly were excluded from the model since the focus in this work was on the flow distribution in the flow channels.

The incompressible fluid flow is governed by the time-independent Navier–Stokes and continuity equations:

$$-\rho\mathbf{u}\cdot\nabla\mathbf{u} \quad \rho\mathbf{g} - \nabla p \quad \nabla\cdot(\eta(\nabla\mathbf{u} \quad \nabla\mathbf{u}^{T})) \quad \mathbf{S}_{NS} \tag{1}$$

$$\nabla\cdot(\rho\mathbf{u}) \quad S_{con} \tag{2}$$

which apply to a laminar flow. The flow region, laminar or turbulent, is defined by the Reynolds number, Re:

$$Re \quad \frac{\rho u D_h}{\eta} \tag{3}$$

A flow is laminar when $Re < 2000$. In the studied flow field models the Reynolds number is below 160 and Eqs. (1) and (2) apply to the problem under study.

The source terms in Eqs. (1) and (2), S_{con} and $\mathbf{S}_{NS}$, are calculated from the change in gas composition caused by the cell reactions. The half and full cell reactions of the PEMFC are:

$$\text{anode}: \quad H_2 \rightarrow 2H \quad 2e^- \tag{4}$$

$$\text{cathode}: \quad \tfrac{1}{2}O_2 \quad 2H \quad 2e^- \rightarrow H_2O \tag{5}$$

$$\text{full cell}: \quad \tfrac{1}{2}O_2 \quad H_2 \rightarrow H_2O \tag{6}$$

The continuity equation source term S_{con} is calculated from the mass difference between the consumed oxygen and produced water molecules. The Navier–Stokes source term $\mathbf{S}_{NS}$ is calculated based on the assumption that the kinetic energy and momentum of the oxygen consumed in the reactions are lost into the gas diffusion layer so that the reaction product water has no initial velocity. Thus, the momentum and mass source terms can be written as

$$\mathbf{S}_{NS} \quad -\frac{iA_{act}}{zFV_{ch}} M_{O_2}\mathbf{u} \tag{7}$$

$$S_{con} \quad \frac{iA_{act}}{zFV_{ch}}(\alpha M_{H_2O} - M_{O_2}) \tag{8}$$

where V_{ch} is the volume of the channels crossing the active area of the cell. However, it is likely that some of the kinetic energy and momentum of the consumed oxygen is in fact transferred to the produced water molecules, but estimating the magnitude of this phenomenon is difficult. Therefore, for comparison, the models were also solved using an alternative Navier–Stokes source term calculated by assuming that the kinetic energy and momentum of the consumed oxygen molecules are transferred to the produced water molecules so that their initial velocity equals the average fluid velocity in the channel:

$$\mathbf{S}_{NS\,2} \quad \frac{iA_{act}}{zFV_{ch}}(\alpha M_{H_2O} - M_{O_2})\mathbf{u} \tag{9}$$

The solutions corresponding to the different Navier–Stokes source terms $\mathbf{S}_{NS}$ and $\mathbf{S}_{NS,2}$ gave close to equal results, as the relative differences in the flow velocities were in the order of 10^{-3}. Thus, the possible error made in approximating the Navier–Stokes source term by Eq. (7) should be negligible.

2.2. Approximations

Eq. (1) can be simplified for modeling purposes. According to dimensional analysis the gravity force term $\rho\mathbf{g}$ can be excluded, since its weight is approximately 10^{-3} times the weight of the inertial term:

$$\frac{\rho\mathbf{g}}{\rho\mathbf{u}\cdot\nabla\mathbf{u}} \approx \frac{\rho g}{\rho U^2 \; L} \quad \frac{gL}{U^2} \approx 10^{-3} \tag{10}$$

The channel walls in a flow system can be assumed smooth, if the surface roughness of the wall material is smaller than the limiting surface roughness characteristic to that system [11]:

$$\Delta_{lim} \quad 17\,85\, D_h Re^{-0\,875} \tag{11}$$

With the parameters of the 3D model, $D_h = 0.67$ mm and $Re^{max} = 160$, Eq. (8) gives $\Delta_{lim} = 210$ μm. This is clearly larger than the surface roughness of typical flow field plate materials such as graphite, polymer composite and steel, whose surface roughness is in the order of a few 10 μm or less, see, e.g. [12,13]. However, one of the channel walls is formed by the gas diffusion layer where there is mass transfer through the surface that should be taken into account. Nevertheless, including this effect would complicate the modeling and consequently was excluded here.

The effect of gas cross-over between channels can be neglected since the Sherwood number:

$$Sh \quad \frac{UL}{D^{eff}} \quad \text{where } D^{eff} \quad D\varepsilon^{1\,5} \tag{12}$$

is in the order of 10^3, i.e. the flux in the channels is three orders of magnitude larger than the diffusive flux in the gas diffusion layer. The effect of possible convective flow between the channels is also insignificant since the pressure differences between two parallel channels are very small, at largest a few pascals, which was determined from the solved models.

The current density and temperature in the cell are assumed to be constant across the active area. This is usually not the case in a real fuel cell, where the current density, temperature and flow distribution are all interconnected and also depend on external factors such as the cooling system of the cell. Taking all these issues into account would have made the models very complex and as a consequence required a lot of computing capacity, which was the reason why constant values for these parameters were assumed in this work.

The assumption of one-phase flow, i.e. no liquid water in the channels, is justified if the relative humidity remains lower than 100%. Taking into account the reaction product water of which half is assumed to leave the cell through the cathode side, this applies if the relative humidity of the inlet gases is below 64%, which was calculated assuming a stoichiometry of two and a constant cell temperature of 343 K. These values correspond to the parameter values used in the modeling. In many real fuel cells, the fluid may be in a two-phase flow, and the modeling results gained here do not necessarily apply in these cases. However, high-temperature and low-humidity membranes that function under one-phase flow operating conditions such as assumed in the modeling have been developed (see, e.g. [14–17]) and thus the assumption should be valid for several real fuel cells.

2.3. Model properties

A schematic of the 2D geometry is displayed in Fig. 1. The design of the 3D geometry is similar in principle, but here the distributor channel and the parallel channels crossing the cell are in different planes and the channels are divided into groups of five channels. A schematic of the 3D geometry is presented in Fig. 2. The height of the distributor channel is 1 mm and the height of the parallel channels is 0.5 mm. The cylinders that connect the distributor channel and the parallel channels have a radius of 0.5 mm and height of 2 mm. Each cylinder distributes the flow to five parallel channels and certain periodicity resulting

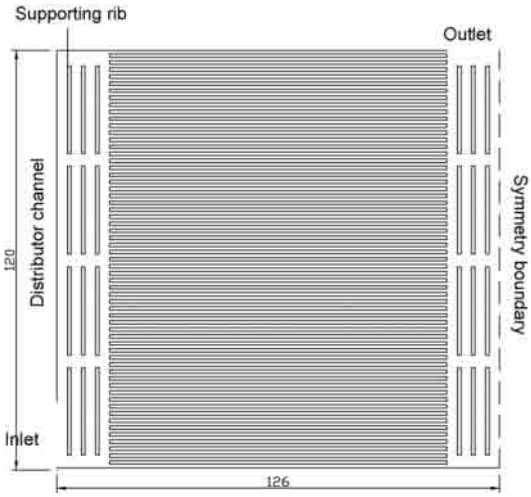

Fig. 1. A schematic of the 2D geometry.

from this can also be seen in the channel flow velocities as will be discussed later in Section 3.2. At the inlet boundaries marked in Figs. 1 and 2, the velocity is fixed: $\mathbf{u}(u\ \ v\ \ w)\quad(u_0\ \ 0\ \ 0)$. At the outlet boundaries also marked in Figs. 1 and 2, the pressure is fixed to zero, $p = 0$. The absolute value of the outlet pressure does not affect the fluid behavior since that is dependent only on the pressure gradients within the flow field, which can be determined from Eq. (1). Due to symmetric channel geometries, only one half of the cathode flow field was modeled. The symmetry boundaries were modeled with the symmetry boundary

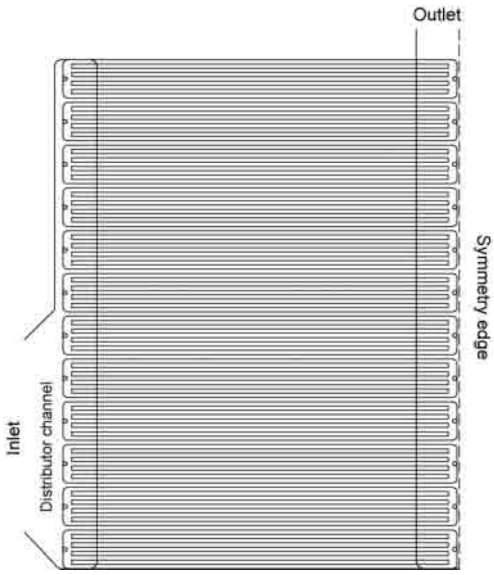

Fig. 2. A schematic of the 3D geometry.

condition:

$$\mathbf{u}\cdot\mathbf{n}\quad 0 \tag{13}$$

$$\mathbf{t}_1\cdot\eta(\nabla\mathbf{u}\quad\nabla\mathbf{u}^{\mathrm{T}})\mathbf{n}\quad 0 \tag{14}$$

and

$$\mathbf{t}_2\cdot\eta(\nabla\mathbf{u}\quad\nabla\mathbf{u}^{\mathrm{T}})\mathbf{n}\quad 0 \tag{15}$$

The majority of the boundaries, corresponding to impermeable channel walls, were governed with the no-slip condition $\mathbf{u} = 0$. It should be noted that the no-slip condition was applied also to the wall formed by the gas diffusion layer in order to avoid further complexity in the modeling, despite the fact that in a real fuel cell mass transfer exists through this boundary.

The inlet flow velocity is calculated from the current density i that was used as a solver parameter:

$$u_0\quad\frac{\dot{n}_{\mathrm{O_2}}}{x_{\mathrm{O_2\ in}}}\frac{RT}{p_0A_{\mathrm{in}}}\quad\frac{RT}{x_{\mathrm{O_2\ in}}p_0}\frac{\lambda A_{\mathrm{act}}}{ez_{\mathrm{cath}}N_{\mathrm{A}}A_{\mathrm{in}}}i \tag{16}$$

where A_{act} is the active area of the cell and A_{in} the cross-sectional area of the inlet. The change in the density and viscosity of the gas in the channels is calculated from the molar fractions of oxygen and water:

$$\begin{aligned}x_{\mathrm{O_2}}(s)\quad&\frac{\dot{n}_{\mathrm{O_2}}}{\dot{n}_{\mathrm{tot}}}\quad\left(\frac{u_{\mathrm{ch}}A_{\mathrm{act}}}{V_{\mathrm{m}}}x_{\mathrm{O_2\ in}}-\frac{iA_{\mathrm{act}}}{z_{\mathrm{cath}}F}\frac{s}{l}\right)\\&\times\left(\frac{u_{\mathrm{ch}}A_{\mathrm{act}}}{V_{\mathrm{m}}}-\frac{iA_{\mathrm{act}}}{z_{\mathrm{cath}}F}\frac{s}{l}\quad 2\alpha\frac{iA_{\mathrm{act}}}{z_{\mathrm{cath}}F}\frac{s}{l}\right)^{-1}\\&\left(x_{\mathrm{O_2\ in}}-\frac{iV_{\mathrm{m}}}{u_{\mathrm{ch}}z_{\mathrm{cath}}F}\frac{s}{l}\right)\\&\times\left(1-(2\alpha-1)\frac{iV_{\mathrm{m}}}{u_{\mathrm{ch}}z_{\mathrm{cath}}F}\frac{s}{l}\right)^{-1}\end{aligned} \tag{17}$$

$$\begin{aligned}x_{\mathrm{H_2O}}(s)\quad&\frac{\dot{n}_{\mathrm{H_2O}}}{\dot{n}_{\mathrm{tot}}}\quad\left(x_{\mathrm{H_2O\ in}}\quad 2\alpha\frac{iV_{\mathrm{m}}}{u_{\mathrm{ch}}z_{\mathrm{cath}}F}\frac{s}{l}\right)\\&\times\left(1-(2\alpha-1)\frac{iV_{\mathrm{m}}}{u_{\mathrm{ch}}z_{\mathrm{cath}}F}\frac{s}{l}\right)^{-1}\end{aligned} \tag{18}$$

The individual channel velocities u_{ch} were calculated by numerical integration across the channel volume separately for each channel:

$$u_{\mathrm{ch}}\quad\frac{1}{V_{\mathrm{ch}}}\sum_{i\ \ 1}^{N}u_iV_i \tag{19}$$

where V_{ch} is the volume (area in 2D) of the channel, N the number of calculation points, u_i and V_i are the velocity at point i and the weight factor at point i (volume in 3D and area in 2D of the space represented by point (i)), respectively. Thus, u_{ch} is the average velocity in the channel.

In the modeling, it was assumed that the water transport coefficient $\alpha = 0.5$, i.e. one half of the product water leaves through the anode side. Thus, the term $2\alpha - 1 = 0$ and the equations for

the molar fractions simplify to:

$$x_{O_2}(s) \quad x_{O_2\ \mathrm{in}} - \frac{iV_m}{u_{ch} z_{cath} F}\frac{s}{l} \tag{20}$$

$$x_{H_2O}(s) \quad x_{H_2O\ \mathrm{in}} \quad 2\alpha\frac{iV_m}{u_{ch} z_{cath} F}\frac{s}{l} \tag{21}$$

These equations were used in the models with the addition that the molar fraction of oxygen cannot be negative and the molar fraction of water has a maximum value corresponding to the situation where all oxygen has been consumed. No acceptable solution can exist outside these limits.

Using the ideal gas law and assuming that dry air is a mixture of oxygen, nitrogen and argon, the density of the gas is calculated from:

$$\rho(s) \quad \frac{(p_{atm} \quad p)(M_{H_2O} x_{H_2O}(s) \quad M_{O_2} x_{O_2}(s) \quad M_{N_2} x_{N_2} \quad M_{Ar} x_{Ar})}{RT} \tag{22}$$

where x_{N_2} and x_{Ar} are constant when $\alpha = 0.5$. The viscosity of the gas mixture is [11]:

$$\eta(s) \quad \left(\frac{x_{H_2O}(s)}{\eta_{H_2O}} \quad \frac{x_{O_2}(s)}{\eta_{O_2}} \quad \frac{x_{N_2}}{\eta_{N_2}} \quad \frac{x_{Ar}}{\eta_{Ar}}\right)^{-1}\frac{\rho(s)}{\rho_{in}} \tag{23}$$

where ρ_{in} is the density of the dry inlet air. The density and viscosity values of the relevant gases as well as their molar fractions in dry standard air are listed in Appendix A.

A non-uniform flow profile makes it easy to study the effect of different approximations on the solution since the differences are usually more prominent at the local minima and maxima. A non-uniform flow profile is easier to accomplish with a 2D geometry due to smaller hydraulic resistance, and thus the modeling was done both in two and three dimensions. In both dimensions, three different modeling schemes were employed to study the effect of the density and viscosity variation:

1. Constant density and viscosity: $\rho = \rho_{air}$ and $\eta = \eta_{air}$. Zero source terms. Continuity equation: $\nabla \cdot \mathbf{u} = 0$.
2. Varying density and viscosity: $\rho = \rho(s)$ and $\eta = \eta(s)$. Zero source terms. Continuity equation: $\nabla \cdot \mathbf{u} = 0$.
3. Varying density and viscosity: $\rho = \rho(s)$ and $\eta = \eta(s)$. Nonzero source terms: S_{con} and $\mathbf{S}_{NS}$. Continuity equation: $\nabla \cdot (\rho \mathbf{u}) = S_{con}$.

The models were solved with the commercially available partial differential equation software FEMLAB®. The calculations were performed over a 64-bit FEMLAB® client-server connection. The server computer was an AMD Athlon64 3500+ with 4GB RAM and 40GB of swap-space. The operating system was SuSe 9.1 AMD64 Linux. The 2D geometry was modeled with 28 000 mesh elements resulting in 160 000 degrees of freedom, whereas the 3D geometry had 180 000 elements and 1.2 million degrees of freedom. In each element, quadratic Lagrange polynomials were used as shape-functions for the components of the velocity field while linear polynomials were used for pressure. The models were solved to as high current densities as the FEMLAB® solver could reach, i.e. 0.35 A cm^{-2} for the 2D geometry and 0.4 A cm^{-2} for the 3D geometry. The experimental parameters corresponded to a 0.5 A cm^{-2} current density, which is the designed operating current for the studied cell and sufficiently close to the 0.4 A cm^{-2} current density of the 3D model for the flow field profiles to be comparable.

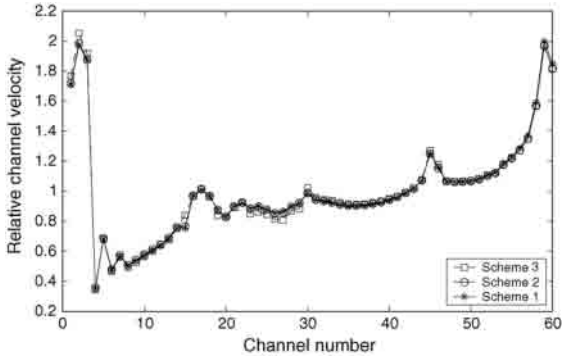

Fig. 3. The relative channel velocities in the 2D model.

3. Results

3.1. 2D geometry

The two-dimensional modeling domain consisted of the cross-sectional area of 60 straight parallel channels and distributor channels as illustrated in Fig. 1. The results discussed here correspond to the highest current density at which the model converged, 0.35 A cm^{-2}. The modeled 2D flow distribution is illustrated in Fig. 3. The channel velocities are taken as the average velocities in the channels integrated over the channel region where the flow is stabilized according to the principle that was presented in Eq. (19). The flow distribution is strongly polarized, as the velocities close to the edges of the flow field plate are more than two times larger than the smallest channel velocities. The lines corresponding to the different approximations are close to indistinguishable. Therefore, the differences in channel velocities predicted by Schemes 1–3 are illustrated in Fig. 4. Based on this data, the maximum differences in relative individ-

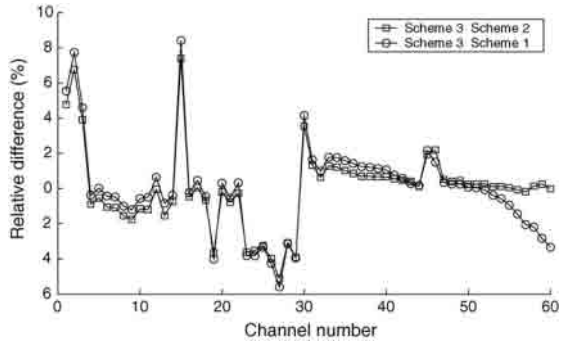

Fig. 4. The relative differences of the results given by the different approximations.

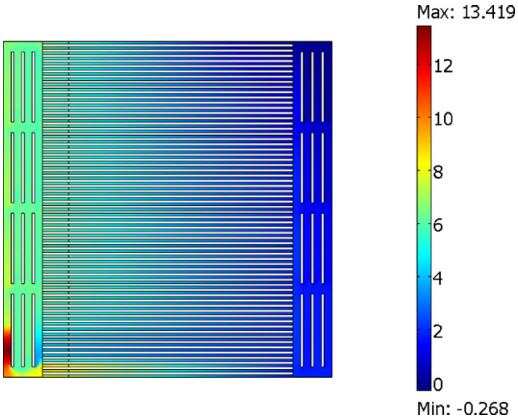

Fig. 5. The pressure distribution in the 2D model. The pressure dimension is pascal (Pa).

ual channel velocities between Schemes 2 and 3 were 7.4% and 8.4% for Schemes 3 and 1. The total pressure losses of Schemes 1 and 2 were 1.1% and 2.3% smaller than that of Scheme 3, respectively. For clarity, the pressure distribution across the 2D geometry corresponding to Scheme 3 with 0.35 A cm^{-2} current density is illustrated in Fig. 5.

3.2. 3D geometry

The three-dimensional model corresponded to an existing parallel channel flow field plate. The modeling results discussed here are the solutions corresponding to the highest current density at which the model converged, which was 0.4 A cm^{-2} for the 3D geometry. The velocity profiles for smaller current densities do not significantly differ from the ones presented here. However, these results do not apply to significantly higher current densities or stoichiometric ratios where the increased flow rate causes more turbulence. The 3D flow-field consisted of 60 channels divided into 12 five-channel groups and distributor channels such as illustrated in Fig. 2.

The relative channel velocities are presented in Fig. 6, where a distinctive five-channel periodicity that derives from the channel system design can be seen in the channel velocities. The flow profile of the 3D model is significantly more uniform than

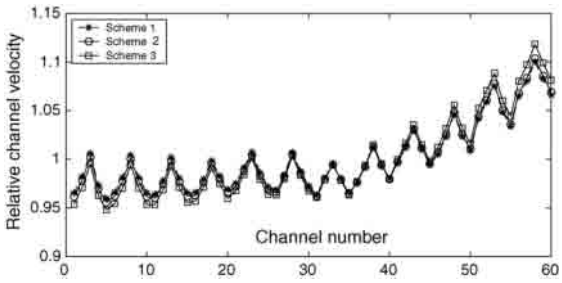

Fig. 6. The relative channel flow velocities of the 3D model.

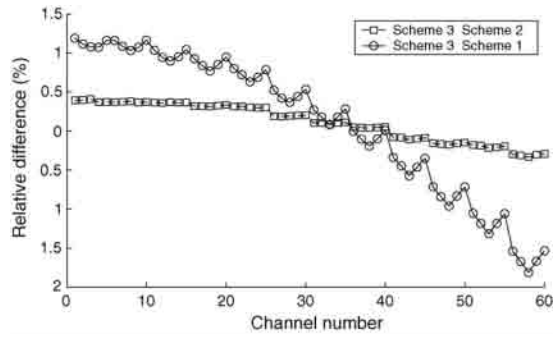

Fig. 7. The relative differences between the different modeling schemes of the original 3D geometry.

that of the 2D model discussed above. The largest individual channel velocity is 16% larger than the smallest. The difference between the largest and smallest five-channel averages is 12%. The differences in relative channel velocities between Schemes 1 and 3 are illustrated in Fig. 7. The maximum differences are 1.8% (Scheme 3 versus Scheme 1) and 0.4% (Scheme 3 versus Scheme 2), significantly smaller than those of the 2D geometry. The channel velocities in Scheme 3 differ more from the velocities in Schemes 1 and 2 in the channels close to the edges of the active area. This follows from the source terms in Scheme 3 that take into account the momentum that is lost into the gas diffusion layer. The total gas flow sees this phenomenon as an increase in the hydraulic resistance on the outlet side. Thus, the channel velocities are slightly larger on the outlet side in Scheme 3. In the 2D model, this effect is more difficult to see since the total differences between Schemes 1 and 3 are significantly larger. The total pressure losses of Schemes 1 and 2 were 9.0% and 7.3% larger than that of Scheme 3, respectively. The pressure distribution across the modified 3D geometry corresponding to Scheme 3 with 0.4 A cm^{-2} current density is illustrated in Fig. 8.

One of the objectives of this work was to achieve a parallel channel flow field, where the flow velocities in different channels

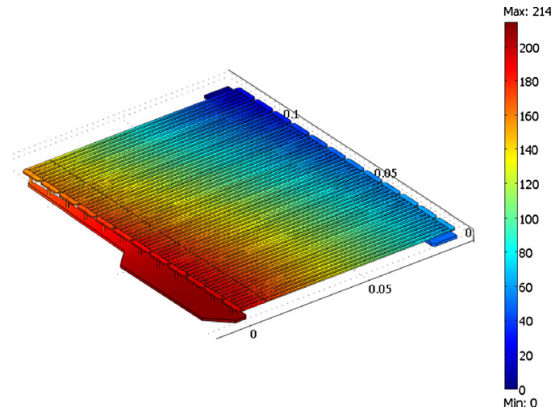

Fig. 8. The pressure distribution in the 3D model. The pressure dimension is pascal (Pa) and the length dimension is meter (m).

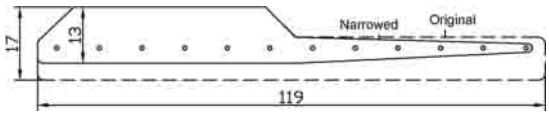

Fig. 9. The original and modified distributor channel geometries.

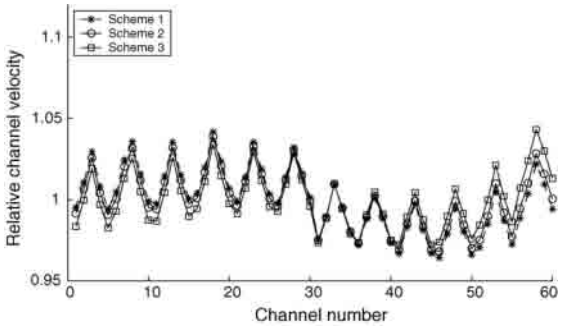

Fig. 10. The close to even channel velocity profile of the modified 3D model.

are close to equal. To accomplish this, the hydraulic resistance of the inlet distributor channel was modified by changing its geometrical shape. The modified distributor channel was optimized for the 0–0.5 A cm^{-2} current density with stoichiometric ratios between 1 and 2. With higher flow rates the velocity distribution will likely become more polarized. Schematics of the original and modified inlet distributor channel geometries are illustrated in Fig. 9.

The velocity profile of this modified 3D geometry is illustrated in Fig. 10. The largest individual channel velocity is approximately 8% larger than the smallest channel velocity, which means that the 16% difference of the original 3D geometry has been reduced to half. When the differences in each five-channel group average are studied, the 12% value of the original 3D geometry has diminished to 3.7%. Thus, the effect of the modification is significant. The differences in relative channel velocities between Schemes 1 and 3 are illustrated in Fig. 11. The maximum differences are 2.1% (Scheme 3 versus Scheme 1) and 0.7% (Scheme 3 versus Scheme 2). These values are

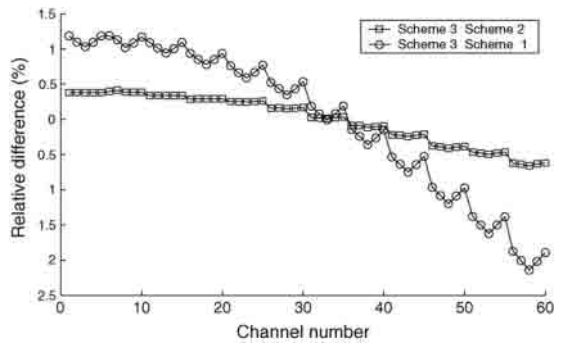

Fig. 11. The relative differences between the different modeling schemes of the modified 3D geometry.

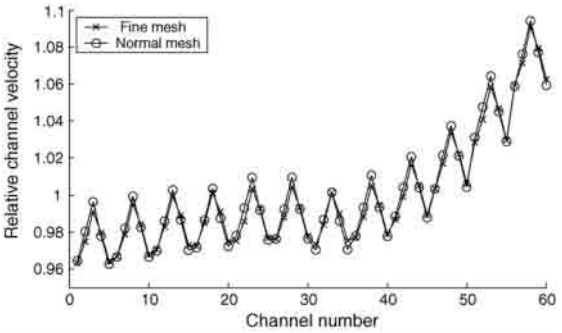

Fig. 12. The relative velocities of the original 3D geometry with two different meshes.

slightly larger than those of the original 3D geometry, which implies that the error made in excluding the source terms or the density and viscosity variation depends on the model geometry to some extent. The total pressure losses of Schemes 1 and 2 were 8.7% and 2.4% larger than that of Scheme 3, respectively.

The effect of the mesh size on the results of the 3D model was studied using a mesh of 220 000 elements for the 3D model and comparing the results to the modeling results presented above with 180 000 elements. The velocity profiles are compared in Fig. 12. The differences are small; the maximum difference in the relative channel velocities is 0.5%. The total pressure differences with the different meshes are within 0.2%. The effect of the mesh was also studied with a single five-channel group, where the number of elements could be grown to four times the original. The relative channel velocities were still within the 0.5% error marginal, but the total pressure difference grew to 5%. This gives reason to expect that the relative channel velocities should be fairly reliable, but that the total pressure difference is more inaccurate. Solving the 3D model with a larger number of elements was not realistic since with the available capacity reaching a solution for the model took from 15 to 40 h with the used mesh.

4. Experimental visualization

The modeling data of the original and modified 3D geometries were verified with experiments. The experimental procedure was simple: dye (water-soluble black ink) was mixed to the fluid flow in pulses, and the progress of the dye pulse was recorded with a digital camera. Since mixing dye into the gas flow would have been complicated, the type of fluid was changed from gaseous (air) to liquid (water). In order to conserve the behavior of the flow, the Reynolds number must remain constant in accordance with dimensional analysis. Following from Eq. (3) the product of density and velocity divided by viscosity must remain constant since the hydraulic diameter is not changed. The values of density and viscosity for air and water are listed in Table 1. A similar visualization study utilizing the laser-induced fluorescence method has previously been carried out by Barreras et al. [9].

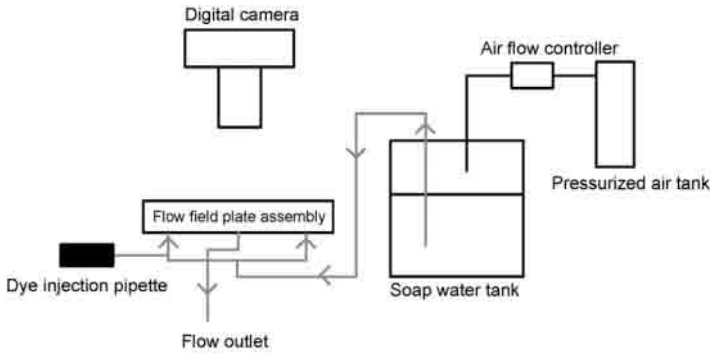

Fig. 13. The experimental arrangement of the flow visualization study. Because of symmetric cell structure, the dye was mixed to only one of the two inlet flows.

The Reynolds number for an air flow in the channels with a flow velocity $u = 1.1\ \mathrm{m\,s^{-1}}$ (corresponding to current density of $i = 0.5\ \mathrm{A\,cm^{-2}}$ at a stoichiometry of two for which the studied cell was designed), is 39. The flow velocity of water in the channels that results in the same Reynolds number is $0.060\ \mathrm{m\,s^{-1}}$, which corresponds to an inlet flow velocity of approximately $200\ \mathrm{ml\,min^{-1}}$.

The flow field plate and endplates were made of transparent polycarbonate. The usual gasket material was replaced with PTFE. The water flow was directed into the flow field plate assembly by pressurizing an air-space in a water tank with a constant $200\ \mathrm{ml\,min^{-1}}$ air flow to provide a stabile flow in the cell assembly. Circulating water through the system caused a part of the channels to be blocked by air bubbles due to the high surface tension of water. Mixing small amounts of soap into the water mostly prevented this phenomenon. The dye was injected with a pipette to the stabilized water flow a few centimeters before the flow entered the cell assembly. The advancing dye pulse was recorded with a Sony® DSC-F828 digital camera. The experimental setup is illustrated in Fig. 13.

The progress of the dye pulse in each five-channel group was studied from the recorded video shots. The flow velocities in each of the 12 five-channel groups were calculated from the time spent by the dye pulse to move through the length of the channels. These calculations were performed with eight sets of experimental data and the results were averaged to give the final values. The error in the channel velocities was taken for both geometries as the maximum average deviation of the individual channel velocities of each measurement set, 4.3% for the original geometry and 5.6% for the modified geometry.

The average velocities of the 12 five-channel groups are compared with the modeled data of the original 3D geometry in Fig. 14. The modeled data, to which the comparisons were made, is that of Scheme 1 (constant density and viscosity), since that is closest to the experimental conditions, where the density and viscosity of the water remain approximately constant. Within the error limits, the experimental results fit the model data, though the experimental velocity profile is more polarized. The stronger polarization is likely due to some systematic error affecting the measurements such as the surface tension of water. Another possibility is that imperfections in the flow field geometry could also have been left in the manufacturing process.

Table 1
Channel velocities corresponding to constant Reynolds number ($Re = 39$) and the densities and viscosities of air and water

	ρ ($\mathrm{kg\,m^{-3}}$)	η (Pas)	Inlet volume flow ($\mathrm{ml\,min^{-1}}$)
Air	1.031401	2.018^{-5}	4104
Water	1000	0.00103	217

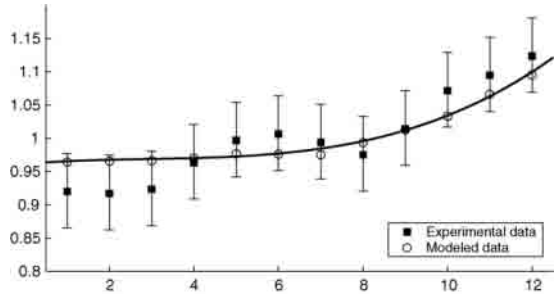

Fig. 14. The experimental and modeling results of the original 3D geometry.

The experiments were also performed with the modified 3D geometry. The results are illustrated in Fig. 15, and the flow profile is more uniform than in Fig. 14 with the original geometry as predicted by the modeling data. Thus, the experiments confirm

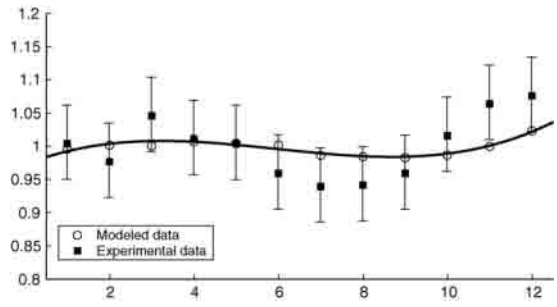

Fig. 15. The experimental and modeling results of the modified 3D geometry.

that the modified geometry should be more advantageous for use in a flow field plate since the reactants should be distributed more uniformly across the active area of the cell.

5. Summary and conclusions

The behavior of fluid flow in an isothermal parallel channel system was modeled with the finite element method. Three modeling schemes based on different approximations were employed in the modeling and the results achieved by these schemes were compared to each other. The modeled 3D parallel channel geometry based on that of a real cell was modified according to modeling data and the improved parallel channel system had nearly uniform flow distribution. The modeled flow profiles were also experimentally verified. The experiments were carried out by recording the progress of a dye pulse in the parallel channels. The distribution of the measured channel velocities was in good correlation with flow distribution predicted by the modeling.

It was discovered that neglecting the density and viscosity variation caused by the cell reactions caused in the case of the 2D geometry at maximum 8% differences in the individual channel velocities. In the case of the close to uniform flow profile of the 3D model this was reduced to 2%. The significance of this error varied between the used geometries, which suggests that in some cases the density and viscosity variation can be neglected, but that this does not hold generally.

However, the results imply that in many cases the effect of excluding the cell reactions on the flow profile is negligible and thus the optimization of the flow field channel system can be done separately from general cell optimization. Uncoupling the flow field channel optimization from the larger cell optimization problem should strongly reduce the required computing capacity. However, the real non-isothermal temperature profile of the cell depends on the cooling system and is likely to have some effect on the flow distribution, offering a subject for further studies.

Based on these conclusions, the 3D parallel channel system was optimized so that a close to uniform flow profile was achieved. Thus, it has been demonstrated in this work that one of the major problems in using the parallel channel system can be overcome with careful design of the flow field plate. This makes the parallel channel flow field a promising alternative due to its typically small pressure losses. The modeling results were verified with experiments and the experimental results were found to be in agreement with the modeling data.

Table A.1
The properties of dry standard air used in the modeling

Component	Molar mass ($g\,mol^{-1}$)	Molar fraction in standard air (%)	η at 343 K (Pas)	ρ at 343 K ($kg\,m^{-3}$)
Nitrogen	28	78	1.97×10^{-5}	0.995
Oxygen	32	21	2.29×10^{-5}	1.137
Argon	40	1	2.60×10^{-5}	1.421
Water	18	0	1.15×10^{-5}	0.64

Acknowledgements

The authors would like to thank the National Technology Agency TEKES and Academy of Finland for funding and VTT Technical Research Centre of Finland for providing flow field plates for the experimental part of the work.

Appendix A

The properties of dry standard air is shown in Table A.1.

References

[1] Z.H. Wang, C.Y. Wang, K.S. Chen, J. Power Sources 94 (2001) 40–50.
[2] L. Wang, H. Liu, J. Power Sources 134 (2004) 185–196.
[3] M. Hu, A. Gu, M. Wang, X. Zhu, L. Yu, Energy Convers. Manage. 45 (2004) 1883–1916.
[4] G. Hu, J. Fan, S. Chen, Y. Liu, K. Cen, J. Power Sources 136 (2004) 1–9.
[5] Y.S. Yoon, W. Lee, S.G. Park, T. Yang, C. Kim, Electrochim. Acta 50 (2004) 705–708.
[6] A. Su, Y.C. Chiu, F.B. Weng, Int. J. Energy Res. 29 (2005) 409–425.
[7] X. Li, I. Sabir, Int. J. Hydr. Energy 30 (2005) 359–371.
[8] G.H. Guvelioglu, H.G. Stenger, J. Power Sources 147 (2005) 95–106.
[9] F. Barreras, A. Lozano, L. Valiño, C. Marín, A. Pascau, J. Power Sources 144 (2005) 54–66.
[10] A. Kumar, R.G. Reddy, J. Power Sources 129 (2004) 62–67.
[11] I.E. Idelchik, Handbook of Hydraulic Resistance, 3rd ed., CRC Press, 1994.
[12] M.H. Oh, Y.S. Yoon, S.G. Park, Electrochim. Acta 50 (2004) 773–776.
[13] S.J. Lee, J.J. Lai, C.H. Huang, J. Power Sources 145 (2005) 362–368.
[14] V. Ramani, H.R. Kunz, J.M. Fenton, J. Membr. Sci. 232 (2004) 31–44.
[15] V. Ramani, H.R. Kunz, J.M. Fenton, Electrochim. Acta 50 (2005) 1181–1187.
[16] S. Yoshioka, A. Yoshimura, H. Fukumoto, O. Hiroi, H. Yoshiyasu, Fuel Cells Bull. 2005 (2005) 11–15.
[17] V. Ramani, H.R. Kunz, J.M. Fenton, J. Power Sources 152 (2005) 182–188.

PUBLICATION 2

Inhomogeneous compression of PEMFC gas diffusion layer

Part II. Modeling the effect

In: Journal of Power Sources 171(1), pp. 113–121.

Available online at www.sciencedirect.com
ScienceDirect
Journal of Power Sources 171 (2007) 113–121
JOURNAL OF POWER SOURCES
www.elsevier.com/locate/jpowsour

Inhomogeneous compression of PEMFC gas diffusion layer Part II. Modeling the effect

Tero Hottinen *, Olli Himanen, Suvi Karvonen, Iwao Nitta

Helsinki University of Technology, Laboratory of Advanced Energy Systems, P.O. Box 2200, Fin-02015 Hut, Finland

Received 4 September 2006; received in revised form 19 October 2006; accepted 31 October 2006
Available online 30 November 2006

Abstract

The effect of inhomogeneous compression of GDL on the mass and charge transfer in PEMFC is studied. The model utilizes experimentally evaluated GDL parameters as a function of thickness. The modeling results are compared with a conventional model that excludes the effects. As a result, it is shown that the inhomogeneous compression has a significant effect on the current density distribution because of the varying contact resistance between GDL and electrode. This also implies that there are possible hot spots occurring inside the electrode, and thus inhomogeneous compression can have significant effects on the lifetime and local performance of the cell. According to the achieved results, the inhomogeneous compression of GDL cannot be neglected.

Keywords: PEMFC; Modeling; Gas diffusion layer; Inhomogeneous compression; Contact resistance; Current density distribution

1. Introduction

Fuel cells are electrochemical devices that convert the chemical energy of reactants directly into electricity and heat. Due to their advantageous properties, such as potential for high energy density and low environmental emissions, fuel cells are believed to gain significant market in the near future. The main applications for fuel cells are automotive, stationary, and portable power production. The large-scale market penetration of fuel cells still requires cost and performance improvements. In order to achieve these improvements, it is essential to have a deep insight into the processes occurring inside the cell and its components.

One of the key components affecting the performance of a polymer electrolyte membrane fuel cell (PEMFC) is the gas diffusion layer (GDL). GDLs have to provide several functions for the fuel cell operation: a passage for reactant access and excess product water removal to and from the electrodes, electronic conductivity, heat removal, and adequate mechanical support for the membrane electrode assembly (MEA). GDLs are typically made of highly porous carbon-fiber based paper or cloth in order to fulfill these requirements. High porosity gives a characteristic soft and brittle structure for the GDLs, which causes a deformation in its shape when the fuel cell is assembled and components compressed together.

The physical properties of GDL are changed under compression, and thus also its mass, heat, and charge transfer properties are changed. Any change in physical properties of GDL in order to improve the charge transport may cause an adverse effect on the mass transport and vice versa. It has been experimentally shown that changes in the properties can have a significant effect on the fuel cell performance, see e.g. [1,2]. It is particularly worth noting that the deformation of GDL is not homogeneous. The parts of the GDL situated under the current collecting rib of the flow-field plate are significantly more compressed than the parts under the channel. This inhomogeneous compression may cause significant changes in the local physical properties of GDL, and thus also in the local cell performance by changing the local reactant and current profiles.

Even though it has been known for some time that the inhomogeneous compression of GDL may have a significant effect

* Corresponding author. Current address: Wärtsilä Corporation, Fuel Cells, Tekniikantie 14, 02150 Espoo, Finland. Tel.: +358 44 5838253; fax: +359 10 7099616.
E-mail address: tero.hottinen@wartsila.com (T. Hottinen).

0378-7753/$ – see front matter © 2006 Elsevier B.V. All rights reserved.
doi:10.1016/j.jpowsour.2006.10.076

Nomenclature

c	concentration (mol m^{-3})
d	channel and rib width (m)
D	diffusion coefficient (m^2 s^{-1})
$\vec{e}$	unit vector
E_0	reversible cell potential (V)
F	Faraday constant (A s mol^{-1})
h	thickness (m)
i	current density (A m^{-2})
j	current production rate (A m^{-3})
j_0	exchange current density (A m^{-3})
k	permeability (m^2)
M	molar mass (kg mol^{-1})
$\vec{N}$	molar flux (mol m^{-2} s^{-1})
p	pressure (Pa)
r	resistance (Ω m^2)
R	gas constant (J mol^{-1} K^{-1})
s	liquid water saturation
T	temperature (K)
$\vec{v}$	velocity (m s^{-1})
X	molar fraction
z	number of transferred electrons

Greek letters

α_r	reaction symmetry factor
ε	porosity
η	overpotential (V)
μ	viscosity (kg m^{-1} s^{-1})
ρ	density (kg m^{-3})
σ	conductivity (Ω^{-1} m^{-1})
ϕ	electronic potential (V)
ϕ_m	protonic potential (V)

Subscripts

a	anode
ave	average
c	cathode
comp	compressed
cont,e	contact between GDL and electrode
cont,gr	contact between GDL and graphite
e	electrode
eff	effective
GDL	gas diffusion layer
H_2O	water
min	minimum
N_2	nitrogen
O_2	oxygen
ref	reference
sat	saturation
x	x-direction, in-plane
y	y-direction, through-plane

on the cell performance, most of the PEMFC modeling studies have neglected this effect. Zhou et al. [3] investigated the effect that the shape of the current collecting rib has on the changes in porosity of GDL and contact resistance between rib and GDL. Sun et al. [4] studied the effect that the inhomogeneous compression of GDL, affecting the local porosity and conductivity, has on the fuel cell performance and local current density distribution. Even though they assumed a fairly small value for the compression (15%) and neglected the permeability and contact resistance effects, they concluded that the inhomogeneous compression affected the local current density distribution notably. Sui and Djilali [5] varied only the values of through-plane conductivity and diffusivity of GDL, and observed that the changes in local values affect the current density profile.

This second part of this contribution focuses on modeling the effect that inhomogeneous compression of GDL has on local species and current distributions. The model utilizes experimentally evaluated parameter values as a function of GDL thickness. These values are taken from the first part of this study, which focused on the ex-situ experimental evaluation of the GDL parameters [6]. The modeling results are compared with a conventional model that excludes the effects of inhomogeneous compression, and assumes the GDL parameters constant. The comparison gives insight into how the inhomogeneous compression of GDL affects the local cell performance.

2. Model

Two different cases are modeled: one with homogeneous properties of GDL (referred to as 'base case') and one where the inhomogeneous compression of GDL is taken into account. The used geometry is a 2D cross-section of the cell, and the modeled geometries are illustrated in Fig. 1. The model consists of the anode and cathode GDLs and electrodes, and the membrane. The ribs and channels of the flow-field plates are accounted for as boundary conditions. Only half-widths of the rib and channel structure and components below them are modeled, and the left and right geometry edges of Fig. 1 (boundaries III–VII) are modeled with symmetry boundary conditions, i.e. it is assumed that the cell geometry continues symmetrically to both directions.

The model takes into account the charge and multicomponent mass transfer in the cathode GDL and electrode, and charge transfer in the membrane and anode GDL and electrode. The main assumptions of the model are that water may exist in two phases but the transfer of liquid phase is similar to gas phase, i.e. equations for capillary movement are not included. In addition, the anode activation and mass transfer limitations are assumed to be negligible, and the cell is treated as isothermal. Even though the effects of inhomogeneous compression are taken into account also at the anode, the intrusion of the GDL into the channel is not included in the modeled geometry. This is made for simplicity, because the inclusion of it has an insignificantly small effect on the current profile of the anode GDL only. The details of the model are described in the following subchapters.

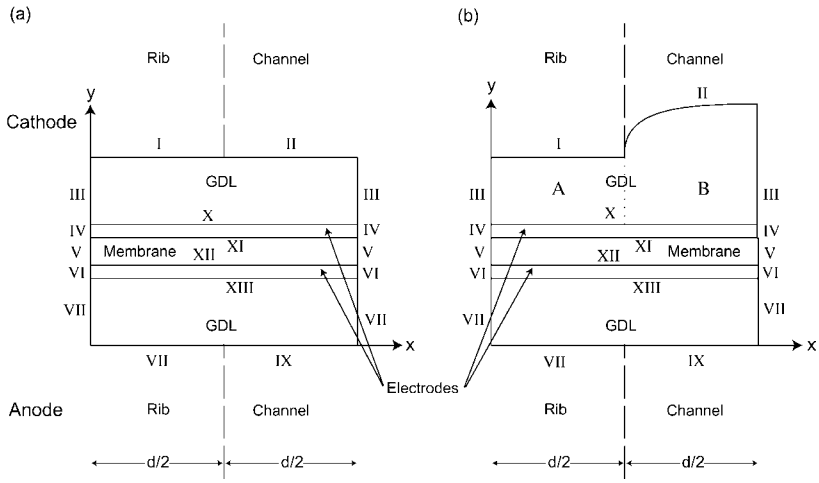

Fig. 1. Modeling domains: (a) geometry with homogeneous compression of GDL (base case); (b) geometry with inhomogeneous compression of GDL taken into account. Roman numerals refer to the boundaries of the modeled geometries. The domains representing different cell components are not in scale in the figure.

2.1. Equations

2.1.1. Cathode GDL

The governing equations at the cathode GDL are the conservation of mass, momentum, species, and charge listed in Eqs. (1)–(4), respectively:

$$\nabla \cdot (\rho \vec{v}) = 0 \tag{1}$$

$$\nabla p = -\frac{\mu}{k}\vec{v} \tag{2}$$

$$\nabla \cdot \vec{N}_i = 0 \tag{3}$$

$$\nabla \cdot \left(-\sigma_{\mathrm{GDL},x} \frac{\partial \phi_{\mathrm{GDL,c}}}{\partial x}\vec{e}_x - \sigma_{\mathrm{GDL},y} \frac{\partial \phi_{\mathrm{GDL,c}}}{\partial y}\vec{e}_y \right) = 0 \tag{4}$$

where different in-plane and through-plane conductivities of GDL are presented with subscripts x and y, respectively.

The multicomponent mass transfer of different species (oxygen, water, and nitrogen) takes into account the convective and diffusive mass fluxes. The species flux equation is

$$\begin{bmatrix} \vec{N}_{\mathrm{O_2}} \\ \vec{N}_{\mathrm{H_2O}} \end{bmatrix} = c\vec{v} \begin{bmatrix} X_{\mathrm{O_2}} \\ X_{\mathrm{H_2O}} \end{bmatrix} - c\bar{D}_{\mathrm{eff}} \begin{bmatrix} \nabla X_{\mathrm{O_2}} \\ \nabla X_{\mathrm{H_2O}} \end{bmatrix} \tag{5}$$

Concentration and density of the gas mixture are calculated from the ideal gas law:

$$c = \frac{p}{RT} \tag{6}$$

and

$$\rho = \frac{pM}{RT} \tag{7}$$

where M is the molar mass of the gas mixture defined as

$$M = \sum_i X_i M_i \tag{8}$$

$\bar{D}_{\mathrm{eff}}$ in Eq. (5) is the effective multicomponent diffusion coefficient tensor corrected by the Bruggeman correlation to take the effect of porosity and tortuosity into account:

$$\bar{D}_{\mathrm{eff}} = (\varepsilon(1-s))^{1.5}\bar{D} \tag{9}$$

The effect of porosity reduction due to liquid water saturation, s, is also accounted for. The saturation s is defined as the fraction of pores occupied by liquid water, i.e. the molar fraction of water exceeding the corresponding saturation molar fraction:

$$X_{\mathrm{sat}} = \frac{p_{\mathrm{sat}}}{p} \tag{10}$$

The saturation pressure of water can be calculated as [7]:

$$\log_{10}(p_{\mathrm{sat}}\,(\mathrm{bar})) = 28.59051 - 8.2\,\log(T+0.01) + 0.0024804(T+0.01) - \frac{3142.31}{T+0.01} \tag{11}$$

which gives the saturation pressure in bar. The components of multicomponent diffusion coefficient tensor $\bar{D}$ are calculated from binary Maxwell–Stefan diffusion coefficients as [8]:

$$\begin{aligned} D_{11} &= D_{\mathrm{O_2,N_2}} \frac{X_{\mathrm{O_2}} D_{\mathrm{H_2O,N_2}} + (1 - X_{\mathrm{O_2}}) D_{\mathrm{O_2,H_2O}}}{S}, \\ D_{12} &= X_{\mathrm{O_2}} D_{\mathrm{H_2O,N_2}} \frac{D_{\mathrm{O_2,N_2}} - D_{\mathrm{O_2,H_2O}}}{S}, \\ D_{11} &= X_{\mathrm{H_2O}} D_{\mathrm{O_2,N_2}} \frac{D_{\mathrm{H_2O,N_2}} - D_{\mathrm{O_2,H_2O}}}{S}, \\ D_{22} &= D_{\mathrm{H_2O,N_2}} \frac{X_{\mathrm{H_2O}} D_{\mathrm{O_2,N_2}} + (1 - X_{\mathrm{H_2O}}) D_{\mathrm{O_2,H_2O}}}{S}, \\ S &= X_{\mathrm{O_2}} D_{\mathrm{H_2O,N_2}} + X_{\mathrm{H_2O}} D_{\mathrm{O_2,N_2}} + X_{\mathrm{N_2}} D_{\mathrm{O_2,H_2O}} \end{aligned} \tag{12}$$

In addition, the pressure and temperature corrections for binary diffusion coefficients are used [9]:

$$D_{i,j} = \frac{p_0}{p}\left(\frac{T}{T_0}\right)^{1.5} D^0_{i,j} \tag{13}$$

The molar fraction of nitrogen is calculated knowing that the molar fractions sum up to unity:

$$X_{N_2} = 1 - X_{H_2O} - X_{O_2} \tag{14}$$

2.1.2. Cathode electrode

The governing equations for the cathode electrode are the same as for cathode GDL with the exception that the conservation equations of mass, species and charge have source terms. The mass and species equations have source terms because of the oxygen consumed and water produced in the fuel cell reactions, and charge equation because the protonic current is changed into electronic current. Thus, these conservation equations are rewritten as in Eqs. (15)–(19):

$$\nabla \cdot (\rho\vec{v}) = -\frac{j_c M_{O_2}}{4F} + \frac{j_c M_{H_2O}}{2F} \tag{15}$$

$$\nabla \cdot \vec{N}_{O_2} = -\frac{j_c}{4F} \tag{16}$$

$$\nabla \cdot \vec{N}_{H_2O} = \frac{j_c}{2F} \tag{17}$$

$$\nabla \cdot (-\sigma_e \nabla \phi_{e,c}) = j_c \tag{18}$$

$$\nabla \cdot (-\sigma_m \nabla \phi_m) = -j_c \tag{19}$$

The current production due to electrochemical reactions at the cathode is calculated from the Butler–Volmer equation:

$$j_c = j_{0,c}\frac{c_{O_2}}{c^{ref}_{O_2}} \exp\left(\frac{-\alpha_r F}{RT}\eta\right) \tag{20}$$

The reference oxygen concentration is taken to be the case where only pure oxygen is present at the electrode, and thus the concentration term in the Butler–Volmer equation can be approximated as the molar fraction of oxygen, i.e.:

$$\frac{c_{O_2}}{c^{ref}_{O_2}} = X_{O_2} \tag{21}$$

The cathode overpotential in Eq. (19) is defined as

$$\eta = \phi_{e,c} - \phi_m - E_0 \tag{22}$$

2.1.3. Cathode boundary conditions

The electronic potential of the cathode decreases at the interface between gas diffusion layer and electrode due to contact resistance. The potentials of electrode and gas diffusion layer are related to each other through the current density passing the interface by Ohm's law giving a condition for both electrode and gas diffusion layer potentials at boundary X:

$$i = -\sigma_{GDL,y}\frac{\partial \phi_{GDL,c}}{\partial y} = -\sigma_e \frac{\partial \phi_{e,c}}{\partial y} = \frac{\phi_{e,c} - \phi_{GDL,c}}{r_{cont,e}} \tag{23}$$

The potential loss in the current collector is assumed to be negligible, and thus the only loss between the gas diffusion layer and current collector is due to contact resistance. Similarly as in Eq. (23) the contact resistance between the current collecting rib and GDL at boundary I yields:

$$i = -\sigma_{GDL,y}\frac{\partial \phi_{GDL,c}}{\partial y} = \frac{\phi_{GDL,c} - \phi_{0,c}}{r_{cont,gr}} \tag{24}$$

No electronic current passes through the interfaces between the GDL and the channel (boundary II), and electrode and membrane (boundary XI), and thus

$$\frac{\partial \phi_{GDL,c}}{\partial y} = \frac{\partial \phi_{e,c}}{\partial y} = 0 \tag{25}$$

The protonic potential is set continuous over boundary XI because it is assumed that there is no contact resistance for protonic current between membrane and electrode. Gas diffusion layer does not conduct protons, and thus no protonic current passes through boundary X yielding:

$$\frac{\partial \phi_m}{\partial y} = 0 \tag{26}$$

It is assumed that the gas mixture is at ambient pressure in the channel and that the gas mixture is always ideally mixed, leading into fixed boundary conditions for pressure and species molar fractions at boundary II. Typically in 2D models, a standard value of 0.21 is used for molar fraction of oxygen. However, such a condition exists only at the very beginning of the inlet channel where no oxygen has been consumed, or when an infinite air stoichiometry is used. For this reason, it is assumed here that the molar fraction of oxygen corresponds to the average value in the middle of the channel when dry air with a stoichiometry of 2 is fed into the cell. This leads into fixed values of approximately 0.153 and 0.077 for oxygen and water molar fractions, respectively. The fixed molar fraction of nitrogen at boundary II is calculated from Eq. (14).

There is no mass transfer at the interfaces between the gas diffusion layer and current collecting rib (boundary I), and electrode and membrane (boundary XI), and thus

$$\vec{v} \cdot \vec{e}_y = 0 \tag{27}$$

$$\vec{N}_i \cdot \vec{e}_y = 0 \tag{28}$$

Because the anode side mass transfer was neglected, it is assumed for simplicity that also the water does not penetrate the membrane.

Finally, symmetry boundary conditions are applied on the boundaries III and IV, i.e.:

$$\vec{v} \cdot \vec{e}_x = 0 \tag{29}$$

$$\vec{N}_i \cdot \vec{e}_x = 0 \tag{30}$$

$$\frac{\partial \phi_{GDL,c}}{\partial x} = \frac{\partial \phi_{e,c}}{\partial x} = \frac{\partial \phi_m}{\partial x} = 0 \tag{31}$$

2.1.4. Membrane and anode

It was assumed that there is no mass transfer of water in the membrane. Thus, the only governing equation at the membrane

is the conservation of charge:

$$\nabla^2 \phi_m = 0 \tag{32}$$

Due to significantly faster electrode kinetics and smaller mass transfer limitations compared to the cathode, the conservation equations of mass, momentum, and species are not solved at the anode. Thus also at the anode gas diffusion layer the only equation to be solved is the conservation of charge:

$$\nabla \cdot \left(-\sigma_{\mathrm{GDL},x} \frac{\partial \phi_{\mathrm{GDL,a}}}{\partial x} \vec{e}_x - \sigma_{\mathrm{GDL},y} \frac{\partial \phi_{\mathrm{GDL,a}}}{\partial y} \vec{e}_y \right) = 0 \tag{33}$$

At the anode electrode the electronic current is consumed and protonic current produced yielding:

$$\nabla \cdot (-\sigma_e \nabla \phi_{e,a}) = -j_a \tag{34}$$

$$\nabla \cdot (-\sigma_m \nabla \phi_m) = j_a \tag{35}$$

where the current production at the anode is calculated from the Tafel equation:

$$j_a = \frac{j_{0,a} z F}{RT} (\phi_{e,a} - \phi_m) \tag{36}$$

2.1.5. Membrane and anode boundary conditions

It is assumed that there is no contact resistance for protonic current at the interfaces between membrane and electrode, and thus the protonic potential is continuous over boundary XII. Boundary conditions for electronic current at the anode electrode and GDL are similar to those at the cathode. The contact resistances at the interfaces between electrode and GDL, and current collecting rib and GDL yield conditions for boundaries XIII and VIII:

$$i = -\sigma_{\mathrm{GDL},y} \frac{\partial \phi_{\mathrm{GDL,a}}}{\partial y} = -\sigma_e \frac{\partial \phi_{e,a}}{\partial y} = \frac{\phi_{\mathrm{GDL,a}} - \phi_{e,a}}{r_{\mathrm{cont,e}}} \tag{37}$$

$$i = -\sigma_{\mathrm{GDL},y} \frac{\partial \phi_{\mathrm{GDL,a}}}{\partial y} = \frac{\phi_{0,a} - \phi_{\mathrm{GDL,a}}}{r_{\mathrm{cont,gr}}} \tag{38}$$

Because the mass transfer at the anode was neglected, the interface between the GDL and gas channel (boundary IX) has only a no current condition:

$$\frac{\partial \phi_{\mathrm{GDL,a}}}{\partial y} = 0 \tag{39}$$

Finally, the symmetry boundary conditions apply again at boundaries V–VII:

$$\frac{\partial \phi_m}{\partial x} = \frac{\partial \phi_{e,a}}{\partial x} = \frac{\partial \phi_{\mathrm{GDL,a}}}{\partial x} = 0 \tag{40}$$

2.1.6. Effect of inhomogeneous compression

Due to the inhomogeneous compression of the gas diffusion layer its properties are changed. The affected GDL properties are porosity, permeability, in- and through-plane bulk conductivities, and contact resistance between gas diffusion layer and electrode interface. These changes are taken into account in the modeled cathode domain B of Fig. 1b. Cathode domain A remains unchanged compared to the base case of Fig. 1a. Because mass transfer is considered negligible at the anode, the effect of the porosity and permeability changes can be neglected there. The only differences at the anode compared to the base case are the varying bulk conductivities of GDL and contact resistance at GDL/electrode interface due to inhomogeneous compression.

The results of the measurements in the experimental part [6] imply that the gas diffusion layer is very little compressed in the middle of the channel, and that the total change from the original uncompressed volume remains small. Thus, the thickness of the gas diffusion layer in the cathode domain B is modeled with a logarithmic curve having a maximum that corresponds to 10 μm compression from the original thickness h_0. The curve was fitted so that it coincides with the constant compressed thickness h_{comp} at the point where the gas channel ends and current collecting rib begins, and equals the maximum thickness in the middle of the channel, i.e. at the right boundary III. The resulting function for gas diffusion layer thickness implemented into the model geometry coordinates is

$$h(x)\,[\mathrm{m}] = \begin{cases} h_{\mathrm{comp}}, & x \in A \\ 19.30314 \log((x - 0.0005) \times 10^6 + 1) \times 10^{-6} + h_{\mathrm{comp}}, & x \in B \end{cases} \tag{41}$$

It is assumed that the change in thickness under compression is due to change in volume of pores, not in volume of bulk material. Thus, the porosity of the GDL can be calculated from the thickness as

$$\varepsilon(x) = \varepsilon_0 \frac{h(x) - h_{\min}}{h_0 - h_{\min}} \tag{42}$$

where $h_{\min}$ equals the minimum thickness when there is only bulk material left, i.e.:

$$h_{\min} = (1 - \varepsilon_0) h_0 \tag{43}$$

A third degree polynomial fit was made with the least square sum method to the permeability data from the measurements [6], and the yielding function (fitting accuracy of $R^2 = 0.994$) for GDL is

$$k(x)\ [\mathrm{m}^2] = -1.700 \times 10^{-11} + 2.760 \times 10^{-7} h(x) - 1.484 \times 10^{-3} h(x)^2 + 2.754 h(x)^3 \tag{44}$$

The GDL in- and through-plane bulk conductivities were modeled as linear fits from the experimental data (fitting accuracies of $R^2 = 1.000$ and 0.975, respectively), and they were

$$\sigma_{\mathrm{GDL},x}(x)\,[\Omega^{-1}\,\mathrm{m}^{-1}] = 6896 - 1.159 \times 10^7 h(x) \tag{45}$$

$$\sigma_{\mathrm{GDL},y}(x)\,[\Omega^{-1}\,\mathrm{m}^{-1}] = 3285 - 8.385 \times 10^6 h(x) \tag{46}$$

An exponential fit for the experimental data ($R^2 = 0.983$) of the contact resistance between GDL and current collecting rib gave

$$r_{\mathrm{cont,gr}}(x)\,[\Omega\,\mathrm{m}^2] = 5.83 \times 10^{-10} \exp(2.06 \times 10^4 h(x)) \tag{47}$$

Because the experimental data of the contact resistance at GDL/electrode interface was unreliable, it was determined from

Table 1
Dimensions of the modeled geometries

Parameter	Symbol	Value
Channel and rib width	d	1 mm
Uncompressed GDL thickness	h_0	380 μm
Compressed GDL thickness	h_{comp}	250 μm
Electrode thickness		10 μm
Membrane thickness		25 μm

the contact resistance of GDL/rib interface. A correction factor for the Nafion content of the electrode, typically approximately 30 vol.%, was used because Nafion does not conduct electrons. Thus, the used function for contact resistance was

$$r_{\mathrm{cont,e}}(x)\,[\Omega\,\mathrm{m}^2] = \frac{1}{1-0.3} r_{\mathrm{cont,gr}}(x) = 1.429 r_{\mathrm{cont,gr}}(x) \quad (48)$$

The above-listed parameter values for domain A and for the base case were calculated from the fitted equations in order to have continuous and similar parameter values between different domains and models.

2.2. Parameters and model solving

The dimensions of the modeled geometries are given in Table 1. The constants and parameters used in the model are listed in Table 2. Standard textbook values for constants and typical values found in the PEMFC modeling articles for fuel cell parameters are used when a reference is not given.

The modeling was done using a commercial finite element method program COMSOL Multiphysics version 3.2b (formerly known as FEMLAB) with a parametric nonlinear direct (UMFPACK) solver. When solving the model, the cell voltage was used as a fixed parameter by setting the potential of anode current collector to zero and the potential of cathode current collector to cell voltage. The used mesh consisted of 24,089 elements for base case and 24,420 elements for the case where inhomogeneous compression was taken into account. The respective degrees of freedom were 36,383 and 46,443.

Table 2
Constants and parameter values

Parameter	Symbol	Value
Ambient pressure	p_0	101,325 Pa
Binary diffusion coefficient O_2,H_2O	$D^0_{O_2,H_2O}$	3.98×10^{-5} m^2 s^{-1}
Binary diffusion coefficient O_2,N_2	$D^0_{O_2,N_2}$	2.95×10^{-5} m^2 s^{-1}
Binary diffusion coefficient H_2O,N_2	$D^0_{H_2O,N_2}$	4.16×10^{-5} m^2 s^{-1}
Conductivity of electrode	σ_e	300 Ω^{-1} m^{-1} [6]
Exchange current density, cathode	$j_{0,c}$	20×10^3 A m^{-3}
Exchange current density, anode	$j_{0,a}$	1.7×10^9 A m^{-3}
Faraday constant	F	96,487 A s mol^{-1}
Gas constant	R	8.314 J mol^{-1} K^{-1}
Molar mass of oxygen	M_{O_2}	0.032 kg mol^{-1}
Molar mass of water	M_{H_2O}	0.018 kg mol^{-1}
Molar mass of nitrogen	M_{N_2}	0.028 kg mol^{-1}
Permeability of electrode	k_e	1.26×10^{-13} m^2 [10]
Porosity of uncompressed GDL	ε_0	0.84 [11]
Porosity of electrode	ε_e	0.4
Protonic conductivity	σ_m	5 Ω^{-1} m^{-1}
Reaction symmetry factor	α_r	0.5
Reversible cell potential	E_0	1.23 V
Temperature	T	323.15 K
Viscosity of air	μ	1.9×10^{-5} kg m^{-1} s^{-1}

3. Results

The polarization curves of the both simulated geometries are illustrated in Fig. 2. These were achieved by changing the cell voltage in steps of 0.1 V and calculating the average current density at each voltage over boundary X as

$$i_{\mathrm{ave}} = \frac{1}{d}\int_0^d \frac{1}{r_{\mathrm{cont,e}}}(\phi_{\mathrm{e,c}} - \phi_{\mathrm{GDL,c}})\,\mathrm{d}x \quad (49)$$

There are no significant differences between the modeled cases at practical cell voltages implying that the overall cell

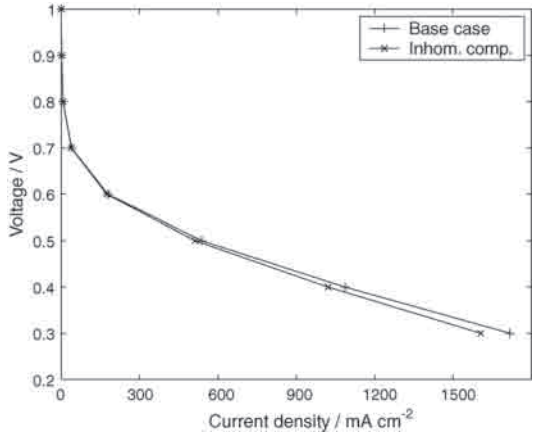

Fig. 2. Polarization curves.

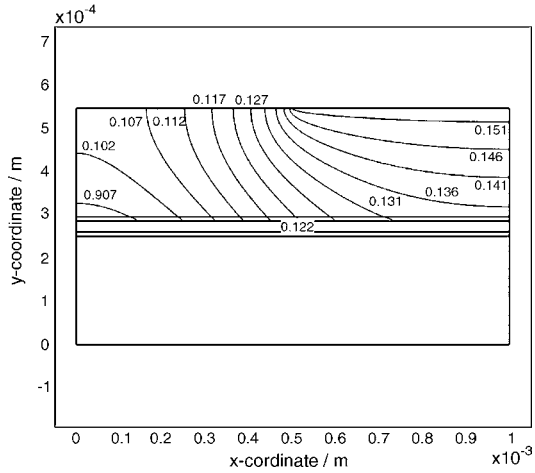

Fig. 3. Oxygen molar fraction at 0.4 V for the base case.

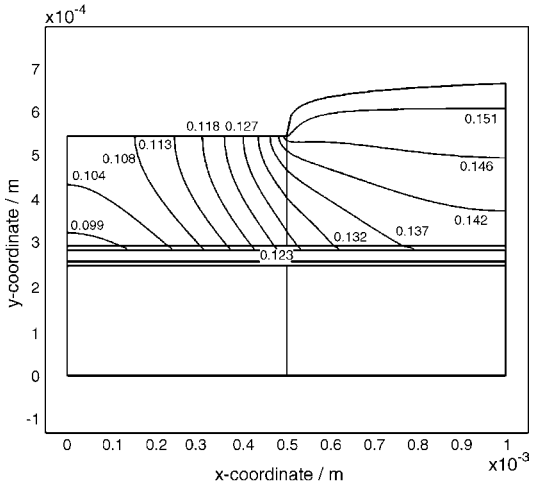

Fig. 4. Oxygen molar fraction at 0.4 V when the inhomogeneous compression is taken into account.

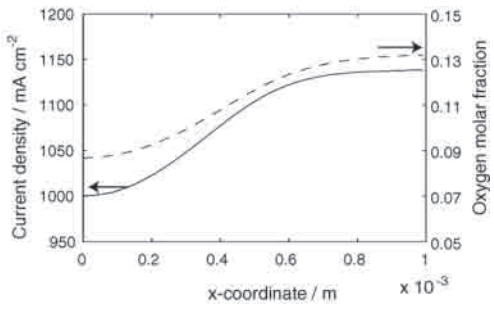

Fig. 5. Current density distribution and oxygen molar fraction at the GDL/electrode interface at 0.4 V for the base case.

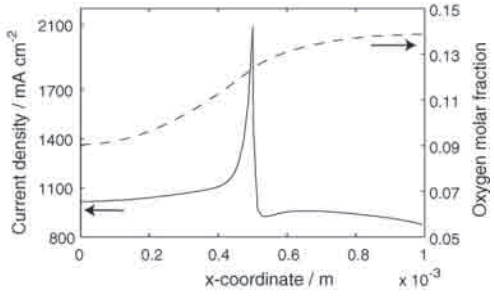

Fig. 6. Current density distribution and oxygen molar fraction at the GDL/electrode interface at 0.4 V when the inhomogeneous compression is taken into account.

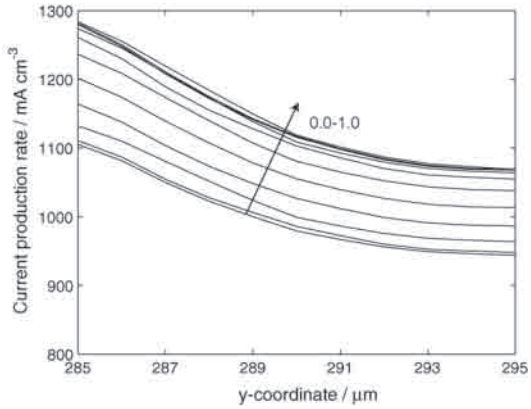

Fig. 7. Current production profiles at the electrode at 0.4 V for the base case. The profiles are current production rates in *y*-direction drawn at every 0.1 mm in *x*-direction. The arrow in the figure shows the direction of increasing *x*-axis.

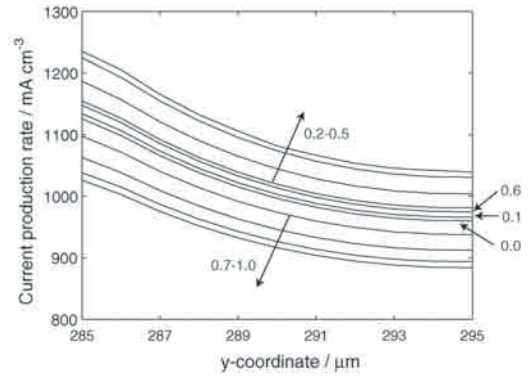

Fig. 8. Current production profiles at the electrode at 0.4 V when the inhomogeneous compression is taken into account. The profiles are current production rates in *y*-direction drawn at every 0.1 mm in *x*-direction. The arrows and labels in the figure show the direction of increasing *x*-axis and corresponding values in millimeters.

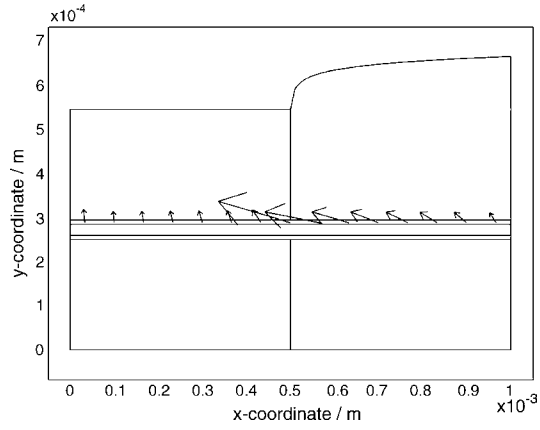

Fig. 9. Current density profile in the cathode electrode at 0.4 V when the inhomogeneous compression is taken into account.

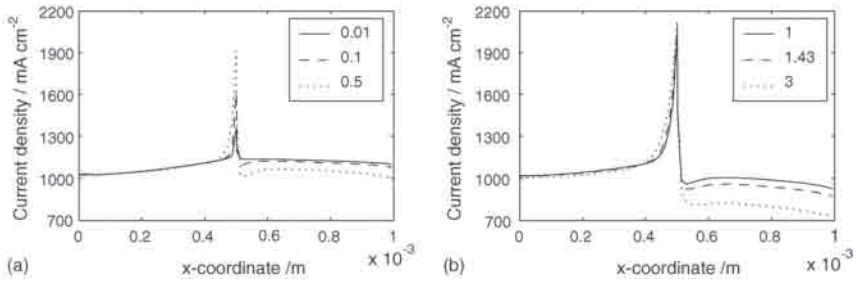

Fig. 10. Current density distributions at the GDL/electrode interface at 0.4 V with varying contact resistance values between GDL and electrode when the inhomogeneous compression is taken into account: (a) $r_{cont,e} = 0.01r_{cont,gr}$, $0.1r_{cont,gr}$, and $0.5r_{cont,gr}$; (b) $r_{cont,e} = r_{cont,gr}$, $1/(1-0.3)r_{cont,gr}$, and $3r_{cont,gr}$.

performance is not significantly affected by the inhomogeneous compression of GDL.

The differences in oxygen molar fractions between the modeled cases were also quite small. As an example, the contour plots of oxygen molar fraction at cell voltage of 0.4 V are illustrated in Figs. 3 and 4. When the inhomogeneous compression is taken into account, the equimolar lines are slightly more vertical and shifted towards the parts below the current collecting rib. For example, there is only a 5% difference in oxygen molar fraction at the GDL/electrode interface below the middle of the channel at 0.4 V. There is also no significant difference when the liquid water saturation begins (at the electrode/membrane interface below the middle of the rib) between the modeled cases, being 519 mV for the base case and 513 mV when the inhomogeneous compression is taken into account.

The small differences in mass transfer are due to relatively high open porosity and permeability of the used GDL. With another GDL material that has a microporous layer and denser structure, the differences in mass transfer are most probably more pronounced. In addition, the capillary movement of liquid water was neglected, and thus the mass transfer at low cell voltages is somewhat distorted.

Even though there were no significant differences in the overall cell performance and molar fractions between the different modeled cases, the current density distribution is significantly affected by the inhomogeneous compression. The current density profiles at GDL/electrode surface at 0.4 V are illustrated in Figs. 5 and 6. Also the oxygen molar fractions at the same interface are illustrated in the figures.

The shape of the current density distribution follows quite much the oxygen molar fraction profile in the base case, which is a very typical modeling result. When the inhomogeneous compression of GDL is taken into account, there is a significant increase in the current density below the position where the channel begins. This increase is not due to numerical inaccuracies of the solution, because the shape of the peak was unaffected by the density of the mesh.

The current production profiles, illustrated in Figs. 7 and 8, show that there are significant differences in the reaction rates between the modeled cases. The reaction rate is decreased below the channel when the inhomogeneous compression is taken into account because of higher resistive losses. However, the differences in reaction rates are quite moderate compared to current density distribution in order to explain the observed peak in Fig. 6.

The reason for the peak is illustrated in Fig. 9, where the current density profile in the cathode electrode is plotted. A significant portion of the current produced in the parts below the channel flows in-plane in the electrode and enters the GDL from the part where the contact resistance is decreased. This phenomenon obeys the second Kirschoff law: the amount of current going through a certain route is inversely proportional to the total resistance of that route. Even though the contact resistance value between GDL and electrode was estimated from the contact resistance between GDL and graphite, the effect exists even if the value was highly overestimated. This is due to the fact that when the total resistive losses under the channel are increased, a bigger portion of the produced current flows laterally in the electrode towards the smaller resistance. This phenomenon is illustrated in Fig. 10, where the current density distribution is calculated with several different contact resistance values ranging from $0.01r_{cont,gr}$ to $3r_{cont,gr}$. The current density distribution is somewhat smoothened when the contact resistance is decreased, but even at two orders of magnitude smaller value, the distribution is still highly peaked. The average current density values between different cases vary from 966 to 1113 mA cm^{-2} between the highest and lowest contact resistance values, respectively.

4. Summary and discussion

This paper focused on modeling the effects that the inhomogeneous compression of gas diffusion layer has on the performance of a PEMFC. Model took into account the multicomponent mass transfer in the cathode components and charge transfer in all of the cell components. Model was isothermal and the capillary movement of liquid water was not taken into account. The experimental parameters evaluated in Ref. [6] were used in the model, and the results were compared with a conventional model that excludes the effects of inhomogeneous compression.

There were no significant differences in the overall cell performance between the modeled cases. In addition, the mass transfer was not significantly affected by the inhomogeneous compression, which was due to the used highly porous and per-

meable GDL. This may not be the case when a denser GDL material with a microporous layer is used, because then the differences in mass transfer are pronounced. In addition, the capillary movement of liquid water was neglected and thus the mass transfer at low cell voltages was somewhat distorted.

The effect of inhomogeneous compression on the reaction rate was evident. The reaction rate was decreased under the channel because of higher total losses caused by increased bulk and contact resistances. Besides affecting the reaction rate, the effect of inhomogeneous compression on current distribution was tremendous. The current density distribution on the GDL/electrode interface was peaked at the parts below the edge of the channel. This was due to redistribution of the current profile in the electrode. A significant portion of the current flowed in in-plane direction in the electrode, and entered the GDL below the rib where there was significantly lower contact resistance. This phenomenon was investigated with several different contact resistance values between GDL and electrode, and even with very small values the current density distribution was significantly peaked.

In the model it was assumed that there is a sharp edge in the shape of the GDL at the rib/channel interface. Even though the measurement results in Ref. [6] implied that the GDB is virtually not compressed below the channel, the edge is not necessarily that sharp in reality. This is especially the case when molded composite flow-field plates with slightly rounded corners are used. However, this causes that the changes in GDL properties under the channel are not that drastic only under the rounding and thus has only a small effect on the current density distribution by slightly widening the peak to the right and rounding the tip of the peak.

The observed current density peak can have tremendous effects not only on current density distribution, but also to temperature distribution inside the cell. According to the analogy between charge and heat transfer, it can be assumed that also a significant portion of the heat produced in the electrode below the channel flows in in-plane direction. This means that there has to be a lateral temperature gradient within the electrode causing a possible hot spot below the channel. In addition, the Ohmic heating at the place where most of the current enters the GDL causes another possible hot spot below the place where the rib begins. This uneven temperature distribution can have significant effects on cell lifetime and the local cell performance. In the optimization of the PEMFC design the effect of these possible hot spots should be minimized by minimizing the parts that have low compression pressure, but in a way that efficient mass transfer is simultaneously ensured.

It was shown in this paper that the inhomogeneous compression of GDL cannot be neglected. In addition, in order to reveal the possible hot spots caused by the lateral current and heat flow in the electrode, also the electrodes have to modeled as a separate domains, i.e. modeling the electrodes as boundary conditions as sometimes is done is not a valid approach. In order to achieve reliable estimates for the temperature distribution, the energy equations have to be included in the model. Before this can be accomplished, accurate evaluation of the GDL bulk and contact heat transfer parameters as a function of thickness is required.

Acknowledgements

The financial support of the National Technology Agency of Finland (TEKES) and the Academy of Finland (project decision no. 206132) is gratefully acknowledged.

References

[1] W.-K. Lee, C.-H. Ho, J.W. Van Zee, M. Murthy, J. Power Sources 84 (1999) 45–51.
[2] J. Ge, A. Higier, H. Liu, J. Power Sources 159 (2006) 922–927.
[3] P. Zhou, C.W. Wu, G.J. Ma, J. Power Sources 129 (2006) 1115–1122.
[4] W. Sun, B.A. Peppley, K. Karan, J. Power Sources 144 (2005) 42–53.
[5] P.C. Sui, N. Djilali, J. Power Sources 161 (2006) 294–300.
[6] I. Nitta, T. Hottinen, O. Himanen, M. Mikkola, Inhomogeneous compression of PEMFC gas diffusion layer. Part I. Experimental, J. Power Sources, submitted for publication.
[7] M.J. Lampinen, Kemiallinen termodynamiikka energiatekniikassa, vol. 90, Publications of Helsinki University of Technology, Laboratory of Applied Thermodynamics, Finland, 1996 (in Finnish).
[8] R. Taylor, R. Krishna, Multicomponent Mass Transfer, John Wiley & Sons Inc., New York, 1993.
[9] J.R. Welty, C.E. Wicks, R.E. Wilson, Fundamentals of Momentum, Heat, and Mass Transfer, 3rd ed., John Wiley & Sons Inc., New York, 1984.
[10] O. Himanen, T. Hottinen, M. Mikkola, V. Saarinen, Electrochim. Acta 52 (2006) 206–214.
[11] Manufacturer's data sheet for ®Sigracet GDL 10 BA by SGL Carbon AG.

PUBLICATION 3

Modelling the effect of inhomogeneous compression of GDL on local transport phenomena in a PEM fuel cell

In: Fuel Cells 8(6), pp. 410–421.

Fuel Cells DOI: 10.1002/fuce.200700058

ORIGINAL RESEARCH PAPER

Modelling the Effect of Inhomogeneous Compression of GDL on Local Transport Phenomena in a PEM Fuel Cell

I. Nitta[1]*, S. Karvonen[1], O. Himanen[2], and M. Mikkola[1]

[1] Laboratory of Advanced Energy Systems, Helsinki University of Technology, P.O. Box 2200, 02015 TKK, Finland
[2] VTT Technical Research Center of Finland, Fuel Cells, P.O. Box 1000, 02044 VTT, Finland

Received November 08, 2007; accepted May 19, 2008

Abstract

The effects of inhomogeneous compression of gas diffusion layers (GDLs) on local transport phenomena within a polymer electrolyte membrane (PEM) fuel cell were studied theoretically. The inhomogeneous compression induced by the rib/channel structure of the flow field plate causes partial deformation of the GDLs and significantly affects component parameters. The results suggest that inhomogeneous compression does not significantly affect the polarisation behaviour or gas–phase mass transport. However, the effect of inhomogeneous compression on the current density distribution is evident. Local current density under the channel was substantially smaller than that under the rib when inhomogeneous compression was taken into account, while the current density distribution was fairly uniform for the model which excluded the effect of inhomogeneous compression. This is caused by the changes in the selective current path, which is determined by the combination of conductivities of components and contact resistance between them. Despite the highly uneven current distribution and variation in material parametres as a function of GDL thickness, the temperature profile was relatively even over the active area for both the modelled cases, contrary to predictions in previous studies. However, an abnormally high current density significantly accelerates deterioration of the membrane and is critical in terms of cell durability. Therefore, fuel cells should be carefully designed to minimise the harmful effects of inhomogeneous compression.

Keywords: Gas Diffusion Layer, Inhomogeneous Compression, Mathematical Model, PEM Fuel Cell

1 Introduction

The polymer electrolyte membrane (PEM) fuel cell has been receiving substantial attention as a potential power source for a wide range of applications because of its lower operation temperature compared to other types of fuel cell, flexibility in size, quick start, environment-friendly characteristics and high energy density. However, further improvements of its performance, lifetime and cost-effectiveness are still needed to achieve a large-scale commercialisation; and a deeper understanding of local phenomena taking place in the fuel cell is of vital importance for future development.

A mathematical model is a powerful tool for studying the various phenomena occurring in a fuel cell from local to system level. An excellent review of fuel cell models is given by Yao et al. [1]. The accuracy of the modelled results depends highly on the modelling parameters and assumptions used. Therefore, the experimental evaluation of the physical parameters used in the models is essential. The properties of gas diffusion layers (GDLs) play an important role in fuel cell operation [2] and many experimental studies can be found on subjects such as gas permeability [3–8], electrical properties [9–14], thermal properties [15–17], water transport properties [18–28] and the effect of compression [17, 29–32]. In accordance with the experimental studies, significant modelling efforts have been devoted to explore the impact of these parameters on the transport mechanisms and fuel cell performance. Examples of the systematic parametric study are found on the electric anisotropy of GDL [33–35], thickness

[*] *Corresponding author, iwao.nitta@gmail.com*

and porosity of the GDL [36–39], pore size distribution [40–42], gas permeability [33, 43, 44], water transport parameters [45–49], and effects of compression [50–53].

One of the most common shortcomings in previous modelling studies is that the effect of inhomogeneous compression on the GDL induced by the rib/channel structure of the flow field plate was not properly considered. A typical carbon paper or cloth GDL is soft and flexible and, therefore, when the GDL is compressed between two flow field plates it is deformed and intrudes into the channel as shown in Figure 1. Variations in GDL thickness and porosity due to compression affect the local transport phenomena since gas permeability, electric conductivity and electric and thermal contact resistances at the interfaces with neighbouring components all depend on compression.

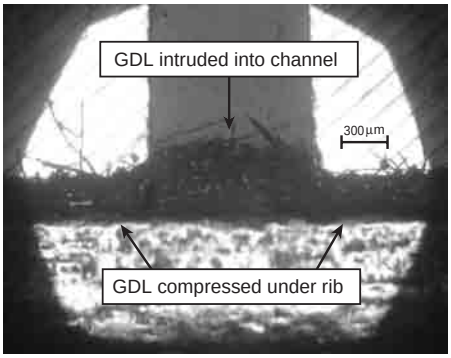

Fig. 1 Cross-sectional view of the GDL (SGL 10 BA, SIGRACET®) taken by optical microscope (PMG3, Olympus).

To the authors' knowledge, only a few studies which consider this inhomogeneous compression can be found in the literature, see ref. [53–56]. Although their findings are enlightening, many of the adopted modelling parameters are subject to a large uncertainty, or some of the relevant issues are ignored. For example, Sun et al. [56] took into account the inhomogeneous compression of GDL, but the contact resistance between GDL and CL and its variation across the active area are not properly considered. Therefore, the authors have experimentally evaluated the physical properties of GDL as a function of compressed GDL thickness [57, 58, 72] as well as conducted a modelling study using the experimental data [59]. In this paper, the earlier model is improved by applying a more realistic geometry of GDL deformation and including thin contact resistance layers with newly evaluated physical parameters as well as correcting some inaccuracies in porosity expression of compressed GDL and assuming an electric contact resistance between GDL and the catalyst layer (CL). However, due to a lack of information, particularly for those which describe liquid water behaviour, the model excludes two-phase phenomena and the study on the subject is left for future work.

2 Model Description

2.1 Model Assumptions

Making a theoretically rigorous fuel cell model which reflects micro- and macro-scale transport processes is extremely challenging because of the lack of experimentally evaluated physical parameters. Therefore, the following assumptions were employed in the model:

1. Steady state conditions;
2. All gases obey the ideal gas law and are ideally mixed;
3. Water exists only in gaseous form;
4. Anode reaction rate is high enough so that the anode activation loss can be neglected, and anode mass transfer is fast enough to keep the H_2 oxidation going at a high rate;
5. CLs and membrane are isotropic and homogeneous;
6. The membrane is fully hydrated;
7. Physical properties of GDL under the rib are constant.

Because of assumption (3), the model presented here is valid only when the partial pressure of water is below the saturation pressure. Assumption (4) implies that the limitations at the cathode become the determining factor in terms of the fuel cell operation and the conservation equations for

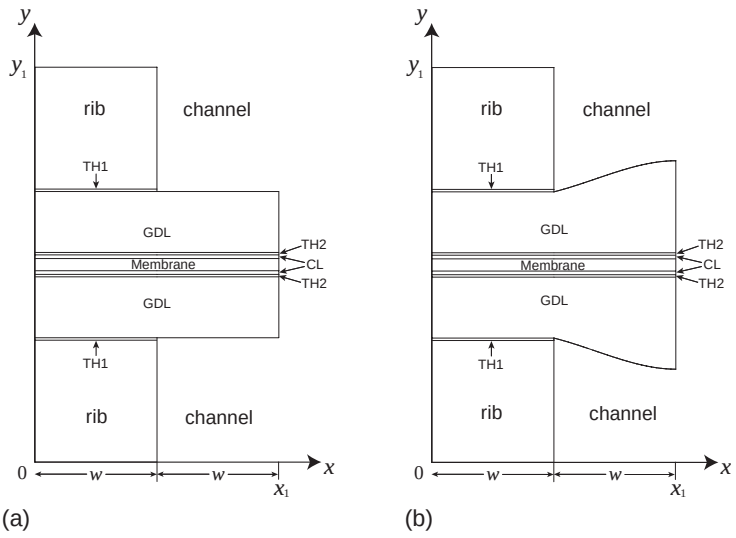

Fig.2 Modelled domain (a) base case and (b) inhomogeneous compression.

mass, momentum and species at anode GDL and CL are not solved. Assumption (7) was made since all the experimental works to evaluate the physical properties of GDL were conducted by changing the thickness of the compressed GDL under the assumption that the compression pressure applied to the GDL were uniform [57, 58, 72].

2.2 Modelling Domain

The modelled domain is a two-dimensional partial cross-section of a unit cell as shown in Figure 2, which consists of a half of both the graphite rib and the channel in the flow field plate, two GDLs and CLs, the electrolyte membrane and two pseudo-thin layers TH1 and TH2 which represent the contact resistance between the graphite rib and GDL, and GDL and CL, respectively.

The effects of inhomogeneous compression are studied by comparing the two models. In the base case [Figure 2(a)] the GDL is compressed evenly and its physical properties are assumed constant. The alternative model [Figure 2(b)] considers the inhomogeneous compression of GDL and the GDL partially intrudes into the flow channel. The shape of the deformed GDL and the dependence of physical properties on the local thickness are described in Section 2.4.

2.3 Equations

2.3.1 Governing Equations and Source Terms

The transport phenomena occurring within the cell are modelled with conservation equations for mass, momentum, species, charge and energy. All the governing equations are listed in Table 1. Table 1 also includes the subdomains where the equations are solved.

The Navier-Stokes equation that describes momentum conservation was reduced to Darcy's law since the Reynolds number is less than one and thus the inertia and viscous terms can be neglected in the GDL and CL. Reynolds number can be calculated using the measured pore radius of GDLs, in ref. [27] and the reported mean gas velocity in them, in ref. [60]. Darcy's law was combined with the mass conservation equation which gives Eq. (1) in Table 1. The species conservation equation Eq. (2) is the Maxwell-Stefan diffusion equation and takes into account the convective and diffusive molar fluxes. Since air is fed to the cathode, the multicomponent mass transfer involves a ternary gas mixture (oxygen, water vapour and nitrogen). The charge conservation Eqs. (3 and 4) describe the electric current in electrically conductive components and ionic current in ionically conductive components. The energy conservation Eq. (5) takes into account both conductive and convective heat fluxes. Note that on the anode only the charge and energy conservation equations were solved.

The source terms for the governing equations are listed in Table 2. Source terms of the mass and species conservation equation represent the consumption of oxygen and production of water in the cathode CL. The number of electrons involved in the reaction (four for oxygen consumption and two for water production) appears in these equations. The source terms in the charge conservation equation describe the charge transfer current density between the electric and ionic phases inside the anode and cathode CLs. The transfer cur-

Table 1 Governing equations.

	Conservation equation	Equation no.	Subdomains
Mass	$\nabla \cdot \left(-\rho_t \frac{k_{sd}}{\mu_t} \nabla p\right) = S_c$	(1)	Cathode (GDL, TH2, CL)
Species	$\nabla \cdot N_i = \nabla \cdot (c_t \mathbf{v} X_i) - \nabla \cdot \left(c_t \bar{D}_{eff} \nabla X_i\right) = S_i$	(2)	Cathode (GDL, TH2, CL)
Charge (electric)	$\nabla \cdot \left(-\sigma_{s,sd} \nabla \varphi_s\right) = S_s$	(3)	Rib, TH1, GDL, TH2, CL
(Ionic)	$\nabla \cdot \left(-\sigma_{m,sd} \nabla \varphi_m\right) = S_m$	(4)	CL, membrane
Energy	$\nabla \cdot \left(\sum_i \rho_i C_{p,i} \mathbf{v} T\right) - \nabla \cdot (\kappa_{sd} \nabla T) = S_T$	(5)	All

Table 2 Source terms in each modelling subdomain.

Region	Mass	Species	Charge	Energy
GDL	0	0	0	$S_T = \sigma_{GDL} (\nabla \varphi_s)^2$
CL (Anode)	0	0	$S_{s,a} = -j_a$ $S_{m,a} = j_a$	$S_T = \sigma_s^{CL} (\nabla \varphi_s)^2 + \sigma_m^{CL} (\nabla \varphi_m)^2 + j_a \eta_a + \frac{j_a T \Delta S_a}{2F}$
(Cathode)	$S_c = -\frac{j_c M_{O_2}}{4F} + \frac{j_c M_{H_2O}}{2F}$	$S_{O_2} = -\frac{j_c}{4F}$ $S_{H_2O} = \frac{j_c}{2F}$	$S_{s,c} = j_c$ $S_{m,c} = -j_c$	$S_T = \sigma_s^{CL} (\nabla \varphi_s)^2 + \sigma_m^{CL} (\nabla \varphi_m)^2 - j_c \eta_c - \frac{j_c T \Delta S_c}{4F}$
TH1, TH2	0	0	0	$S_T = \sigma_{s,sd} (\nabla \varphi_s)^2$
Membrane	0	0	0	$S_T = \sigma_m (\nabla \varphi_m)^2$

rent densities are expressed with the Butler-Volmer relation as follows:

$$j_a = -a_v j_a^{ref}\left[\frac{(\alpha_a^a + \alpha_c^a)F}{RT}\eta_a\right] \quad \text{for anode} \tag{6}$$

$$j_c = a_v j_c^{ref,T}\left(\frac{c_{O_2}}{c_{O_2}^{ref}}\right)\exp\left(-\frac{\alpha_c^c F}{RT}\eta_c\right) \quad \text{for cathode} \tag{7}$$

The anode side has fast reaction kinetics and low overpotential compared to the cathode, and thus the anode transfer current density can be linearised as in Eq. (6). The reference concentration $c_{O_2}^{ref}$ is equal to the concentration of oxygen in air at STP conditions and c_{O_2} is the concentration of oxygen in the CL. In the model, the ratio of c_{O_2} to $c_{O_2}^{ref}$ in Eq. (7) was replaced by the molar fraction of oxygen, X_{O_2}. η_a and η_c are the overpotentials at the anode and cathode, respectively:

$$\eta_a = \varphi_m - \varphi_{s,a} \tag{8}$$

$$\eta_c = \varphi_{s,c} - \varphi_m - E_0 \tag{9}$$

where E_0 is the open circuit voltage.

The source terms in the energy conservation equation correspond to Joule heating, irreversible heat of electrochemical reactions and entropic heat of reactions in CLs but only Joule heating in other subdomains.

The constitutive relations used for the governing equations are listed in Table 3. The molar density can be calculated from the ideal gas law as in Eq. (10). The molar fraction of nitrogen is calculated from the fact that the sum of molar fractions is equal to unity (Eq. 11). The effective Maxwell-Stefan diffusion coefficient tensor, $\bar{D}_{eff}$, is related to the non-porous diffusion coefficient, $\bar{D}$, through the Bruggeman correlation as in Eq. (12). The elements of $\bar{D}$ for a ternary system are calculated from the Maxwell-Stefan binary diffusion coefficients as in Eq. (13). The temperature and pressure dependence of the binary diffusion coefficients were taken into account with Eq. (14). Also, the temperature dependence of exchange current density was taken into account with Eq. (15).

2.3.2 *Boundary Conditions*

Symmetry boundary conditions were applied at $x = 0$ and $x = x_1$ in Figure 2, i.e. all the fluxes were set to zero. No electric current passes through the interface between the GDL/channel and CL/membrane. It was assumed that there is no ionic contact resistance at the CL/membrane interface, and thus the ionic potential and temperature are continuous. On the other hand, ionic current does not pass through the GDL/CL interface since the GDL is not ionically conductive. The concentrations and pressure are continuous through GDL, TH2 and CL, and no boundary conditions are required at the interfaces. However, there is no mass flux across the rib/GDL and CL/membrane interfaces.

At the cathode gas channel/GDL interface, the pressure was set equal to the ambient pressure. The molar fractions of the species at the channel/GDL interface were calculated based on the following assumptions:

1. The modelled cross-section is in the middle of the cell and the produced current is constant along the channel;
2. The stoichiometry of air is 2;
3. Air temperature is 325 K and the relative humidity of the air is 40%;
4. There is no water transport through the membrane.

Thus, the molar fractions of oxygen and water vapour were fixed to 0.143 and 0.149, respectively.

Furthermore, heat transfer from the GDL to air in the channel is calculated via:

$$-\mathbf{nQ} = \kappa_h(T_{GDL} - T_{air}) \tag{16}$$

Table 3 Constitutive relations.

Expression		Equation no.
Ideal gas law	$\rho_t = M_t c_t = \frac{M_t p}{RT}$	(10)
Molar mass of gas mixture	$M_t = \sum_i X_i M_i$	(11)
Effective diffusion coefficient tensor	$\bar{D}_{eff} = \varepsilon_{sd}^{1.5}\bar{D}$	(12)
Elements of $\bar{D}$	$\bar{D}_{11} = D_{O_2,N_2}\frac{X_{O_2}D_{H_2O,N_2} + (1 - X_{O_2})D_{O_2,H_2O}}{S}$	(13)
	$\bar{D}_{12} = X_{O_2}D_{H_2O,N_2}\frac{D_{O_2,N_2} - D_{O_2,H_2O}}{S}$	
	$\bar{D}_{21} = X_{H_2O}D_{O_2,N_2}\frac{D_{H_2O,N_2} - D_{O_2,H_2O}}{S}$	
	$\bar{D}_{22} = D_{H_2O,N_2}\frac{X_{H_2O}D_{O_2,N_2} + (1 - X_{H_2O})D_{O_2,H_2O}}{S}$	
	$S = X_{O_2}D_{H_2O,N_2} + X_{H_2O}D_{O_2,N_2} + X_{N_2}D_{O_2,H_2O}$	
Temperature and pressure dependence of binary diffusion coefficients	$D_{i,j} = \frac{p_0}{p}\left(\frac{T}{T_0}\right)^{1.5} D_{i,j}(p_0, T_0)$	(14)
Temperature dependence of exchange current density	$j_c^{ref,T} = j_c^{ref,T_0}\exp\left[-\frac{\Delta E_{exc}}{R}\left(\frac{1}{T} - \frac{1}{T_0}\right)\right]$	(15)

where **Q** denotes the heat flux calculated from Eq. (5), κ_h the heat transfer coefficient, T_{GDL} the temperature of GDL and T_{air} the temperature of air. The temperature of the graphite ribs at $y = 0$ and $y = y_1$ was set to 330 K. If gas flow in the flow channel is described as a fully developed laminar flow in square duct, and heat is removed from all the walls, the heat transfer coefficient would be between 70 and 90 W m^{-2} K^{-1}. This gives an upper limit for κ_h. Furthermore, a sensitivity analysis of κ_h between solid materials (GDL and graphite current collector) and the gas flow in the channel was conducted, and it was found that this parameter does not significantly affect the temperature profile across the active area. Therefore, a value of 5 W m^{-2} K^{-1} was used for κ_h in the model.

The electric and thermal contact resistances at graphite rib/GDL and GDL/CL interfaces were converted to corresponding electric and thermal conductivities of TH1 and TH2. Therefore, the electric potential and temperature through graphite rib, GDL and CL are continuous through TH1 and TH2 and no boundary conditions have to be prescribed.

2.4 Model Input Parameters

Table 4 lists the cell design parameters and material, kinetic and electrochemical parameters. When the GDL deformation is taken into account (see Figure 2b), the properties of GDL are varied as a function of the thickness. These changes are described in the following Sections.

2.4.1 GDL Deformation

The deformation curve of GDL observed in the photomicrographs taken with an optical microscope (Figure 1) was fitted with a third-order polynomial (fitting accuracy, $R^2 = 0.947$) and its dimensionless thickness can be expressed as

$$h(x) = \begin{cases} h_c\,[\mathrm{m}^{-1}], & x \le 500\ \ 10^{-6}[\mathrm{m}] \\ -1.047x^3\ \ 10^{6}[\mathrm{m}^{-3}] + 2.105x^2\ \ 10^{3}[\mathrm{m}^{-2}] - \\ 1.070x\,[\mathrm{m}^{-1}] + 3.894\ \ 10^{-4}, & x > 500\ \ 10^{-6}[\mathrm{m}] \end{cases} \quad (17)$$

Table 4 Cell design parameters and material properties.

Symbol	Description	Value
Geometrical parameters		
w	Channel and rib width	500 μm
h_c	Compressed GDL thickness under rib	150-300 μm
h_0	Uncompressed GDL thickness	380 μm
	CL thickness	25 μm
	Membrane thickness	50 μm
	TH1, TH2 thickness	10 μm
Material parameters		
$D_{O_2,H_2O}(p_0, T_0)$	Binary diffusion coefficient O_2,H_2O	3.98 × 10^{-5} m^2 s^{-1} [59]
$D_{O_2,N_2}(p_0, T_0)$	Binary diffusion coefficient O_2,N_2	2.95 × 10^{-5} m^2 s^{-1} [59]
$D_{H_2O,N_2}(p_0, T_0)$	Binary diffusion coefficient H_2O,N_2	4.16 × 10^{-5} m^2 s^{-1} [59]
σ_s^{CL}	CL electric conductivity	320 S m^{-1} [57]
σ_m^{CL}	CL ionic conductivity	5.09 S m^{-1}
κ_{CL}	CL thermal conductivity	0.476 W m^{-1} K^{-1} [15]
κ_{GDL}	GDL thermal conductivity	1.18 [72]
σ_{GR}	Graphite electric conductivity	69,700 S m^{-1} [63]
κ_{GR}	Graphite thermal conductivity	128 W m^{-1} K^{-1} [63]
σ_m	Membrane ionic conductivity	5.09 S m^{-1} [64]
κ_m	Membrane thermal conductivity	0.12 W m^{-1} K^{-1} [15]
κ_h	Heat transfer coefficient from solid materials to air	5 W m^{-2} K^{-1}
k_{CL}	Permeability of CL	1.26 × 10^{-13} m^2 [62]
ε_{CL}	Porosity of CL	0.4 [61]
ε_0	Porosity of uncompressed GDL	0.83 [65]
Kinetic and electrochemical and other parameters		
ΔE_{exc}	Activation energy ($E_{cell} \ge 0.8$ V)	76.5 kJ mol^{-1} [66]
	($E_{cell} < 0.8$ V)	27.7 kJ mol^{-1} [66]
p_0	Ambient pressure	101,325 Pa
$\alpha_a^a + \alpha_c^a$	Anodic and cathodic transfer coefficients in Eq. (6)	1 [34]
α_c^c	Cathodic transfer coefficient in Eq. (7)	1 [34]
ΔS_a	Entropy change of anode	0.104 J mol^{-1} K^{-1}
ΔS_c	Entropy change of cathode	–326.36 J mol^{-1} K^{-1}
$a_v j_a^{ref}$	Exchange current density × ratio of reaction surface to CL volume, anode	1.7 × 10^9 A m^{-3} [59]
$a_v j_c^{ref,T_0}$	Exchange current density × ratio of reaction surface to CL volume, cathode	2 × 10^4 A m^{-3} [59]
C_{p,O_2}	Heat capacity of oxygen	923 J kg^{-1} K^{-1}
C_{p,H_2O}	Heat capacity of water	1996 J kg^{-1} K^{-1}
E_0	Open circuit voltage	1.23 V
T_0	Reference temperature	273 K

for the case where the compressed GDL thickness, h_c, is 250 μm. The same process was used to obtain expressions for the thickness of the GDL when the h_c was varied from 150 to 300 μm.

2.4.2 Gas Permeability and Porosity

The reduction of the GDL thickness was assumed to be caused by the reduction of GDL porosity. Therefore, the porosity of the compressed GDL, ε_c, is calculated from the equation (see ref. [5])

$$\varepsilon_c = \frac{h(x) - h_s}{h(x)} = 1 - (1 - \varepsilon_0)\frac{h_0}{h(x)} \tag{18}$$

where ε_0 denotes the porosity of uncompressed GDL and h_0 the thickness of uncompressed GDL. h_s is the thickness of GDL when all the pores are lost:

$$h_s = (1 - \varepsilon_0)h_0 \tag{19}$$

The reduction of GDL porosity leads to a decrease in gas permeability. The in-plane gas permeability of the compressed GDL, $k(x)$, was evaluated [57] and the fitted curve (fitting accuracy, $R^2 = 0.997$) can be expressed as

$$k(x) = 0.806h(x)^3 - 6.464\times10^{-5}h(x)^2 - 5.305\times10^{-8}h(x) + 7.164\times10^{-12}\left[\mathrm{m}^2\right] \tag{20}$$

The permeability of GDL was assumed to be isotropic, i.e. the dependence of through-plane gas permeability on compression was expressed by Eq. (20). Furthermore, Eq. (20) was also used to express the permeability of TH2. The porosity of CL, ε_{CL}, adopted by Bernardi et al. [61] and permeability of CL, k_{CL}, reported by Himanen et al. [62] were assumed to be not affected by compression.

2.4.3 Electric Properties

The electric conductivity of GDL as a function of a compressed GDL thickness was evaluated in a previous study [57]. The conductivity was found to be anisotropic and fitted with a linear curve (fitting accuracy, $R^2 = 0.964$ for in-plane and $R^2 = 0.975$ for through-plane):

$$\sigma_{GDL,x} = -1.159\times10^7 h(x) + 6.896\times10^3\ \left[\mathrm{S\,m^{-1}}\right] \tag{21}$$

for in-plane conductivity and,

$$\sigma_{GDL,y} = -8.385\times10^6 h(x) + 3.285\times10^3\left[\mathrm{S\,m^{-1}}\right] \tag{22}$$

for through-plane conductivity.

The electric contact resistances between the GDL and other cell components depend strongly on the compression pressure. The electric contact resistance between GDL and graphite current collector, $R_{c,GDL/GR}(h_c)$, was found to decrease exponentially as GDL was compressed [57]. The $R_{c,GDL/GR}(h_c)$ was converted into the through-plane electric conductivity of TH1, $\sigma_{TH1,y}(x)$. The $\sigma_{TH1,y}(x)$ was calculated as a function of compressed GDL thickness, and the exponential curve was fitted into the data (fitting accuracy, $R^2 = 0.983$), yielding

$$\sigma_{TH1,y}(x) = 1.714\times10^4\exp\left(-2.056\times10^4 h_c\right)\left[\mathrm{S\,m^{-1}}\right] \tag{23}$$

The electric contact resistance between the GDL and CL, $R_{c,GDL/CL}(h_c)$, was also evaluated experimentally by the authors [58]. The $R_{c,GDL/CL}(h_c)$, was converted to the through-plane electric conductivity of TH2, $\sigma_{TH2,y}(x)$, which was fitted to a third-degree polynomial (fitting accuracy, $R^2 = 0.996$), giving

$$\sigma_{TH2,y}(x) = 7.726\times10^{11}h(x)^3 - 4.943\times10^8 h(x)^2 + 2.664\times10^4 h(x) + 18.911\ \left[\mathrm{S\,m^{-1}}\right] \tag{24}$$

Accurate experimental evaluation of the $R_{c,GDL/CL}(h_c)$ was found to be difficult as the compression pressure decreased. Therefore, in ref. [58], the lowest compression pressure at which the $R_{c,GDL/CL}(h_c)$ could be evaluated was 0.664 MPa. This corresponds to a GDL thickness of approximately 300 μm, above which the accuracy of Eq. (24) diminishes. However, the trend is clear - the lower the compression, the higher the contact resistance.

It should be noted that the values used for the in-plane electric conductivity of TH1 and TH2, $\sigma_{TH1,x}$ and $\sigma_{TH2,x}$, were set equal to the in-plane electric conductivity of GDL and CL, respectively. These values were adopted because the lateral current flow in TH1 and TH2 can be expected to follow that in the neighbouring more conductive components, the GDL and CL. On the other hand, the conductivity of CL evaluated previously [57] was assumed to be isotropic since no reliable experimental data on its anisotropy was found.

2.4.4 Thermal Properties

Compared to electric properties, relatively little experimental data on the thermal properties of GDL have been reported in the literature. According to the authors' previous study [72], the through-plane thermal conductivity of GDL, κ_{GDL}, was not affected by the compression pressure and a constant value was used in this model. The in-plane thermal conductivity of GDL was assumed to be the same as the through-plane thermal conductivity.

The evaluated thermal contact resistance between the graphite current collector and GDL [72] was converted to the through-plane thermal conductivity of TH1, $\kappa_{TH1,y}(x)$. The calculated $\kappa_{TH1,y}(x)$ as a function of compressed GDL thickness was fitted with a fourth degree polynomial (fitting accuracy, $R^2 = 0.993$), giving

$$\kappa_{TH1,y}(x) = -2.912\times10^{14}h(x)^4 + 3.133\times10^{11}h(x)^3 - 1.170\times10^8 h(x)^2 + 1.639\times10^4 h(x) - 0.438\ \left[\mathrm{W\,m^{-1}K^{-1}}\right] \tag{25}$$

The thermal contact resistance between the GDL and CL was assumed to be same as the thermal contact resistance between graphite and GDL. Therefore, Eq. (25) was used also for the through-plane thermal conductivity of TH2, $\kappa_{TH2,y}(x)$. The in-plane thermal conductivities of TH1 and TH2, $\kappa_{TH1,x}$ and $\kappa_{TH2,x}$, were set equal to the in-plane thermal conductivity of GDL and CL, respectively, based on the same assumption of charge transport at the interface.

The thermal conductivity of CL was calculated from the data reported by Khandelwal and Mench [15]. In their study, the combined thermal resistance, i.e. thermal bulk resistance of the CL plus thermal contact resistance between GDL and CL, was determined to be 1.25×10^4 m^2 K W^{-1} at a compression pressure of 1.83 MPa [compressed GDL thickness of ca. 250 μm [72]]. By subtracting the thermal contact resistance between GDL and CL, which can be calculated from Eq. (25), from the combined thermal resistance, the thermal bulk resistance of CL was determined. The thermal conductivity of CL, κ_{CL}, calculated using the measured thermal bulk resistance of CL was assumed to be isotropic and independent of compression.

3 Results and Discussion

3.1 Polarisation Behaviour and Species Distribution

In the following discussion of modelling results, the compressed GDL thickness under the rib is 250 μm for the both cases, i.e. base case and case considering inhomogeneous compression, unless stated otherwise.

The polarisation curves for the two modelled cases, presented in Figure 3, were obtained by changing the cell voltage from 1 to 0.45 V. The curves are almost identical for both the cases except at lower voltages. Since two-phase flow is not taken into account here, the model is valid only when the partial pressure of water, p_{H_2O}, does not exceed the saturation pressure, p_{sat}. The lowest limit for voltage was determined by calculating the relative humidity under the rib where flooding usually starts, see ref. [67]. Figure 4 shows the relative humidity of gas (p_{H_2O}/p_{sat}) at the GDL/CL interface at cell voltages of 0.45 and 0.5 V. In both the modelled cases, water starts to condense when the cell voltage is below 0.5 V. In the following, therefore, the cell voltage is fixed at 0.5 V.

Figure 5 shows the molar fraction of oxygen at the GDL/CL interface for both the modelled cases. Only a slight difference in the molar fraction of oxygen is observed between the two cases as discussed in a previous work [59], which suggests that the mass transfer is not significantly affected by GDL deformation as long as no flooding occurs.

3.2 Current Density Distribution

Figure 6 shows the current density distribution at the GDL/CL interface. For the base case, the current density distribution is fairly uniform over the active area. However, a notably uneven distribution is seen when inhomogeneous compression is taken into account. In this case the local current density is significantly lower in the middle of the channel and increases in the region close to the edge of the rib. This is because of changes in the selective current path, which is largely determined by the electric contact resistance between the GDL and CL, i.e. $\sigma_{TH2,y}(x)$ in Eq. (24), and electric conductivities of GDL in Eqs. (21) and (22). A large portion of the produced current flows laterally under the channel where the contact resistance is high and crosses over to the GDL near the rib edge (see Figure 7).

The shape of the current density distribution is different from that observed in the previous study [59]. The difference mainly arises from the estimates used for the contact resistance between the GDL and CL, and the shape of the deformed GDL, which both differed significantly from the experimentally evaluated values used here. As a result, the current density was overestimated at the edge of the rib and

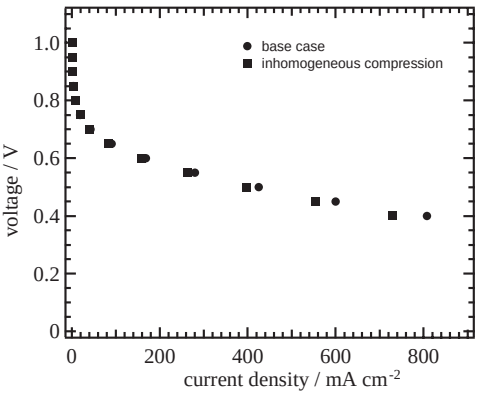

Fig. 3 Polarisation curves for the base case and case considering the inhomogeneous compression.

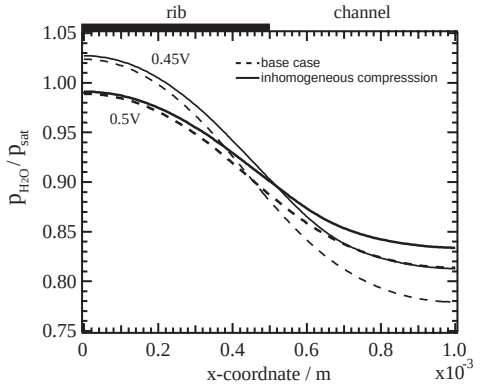

Fig. 4 Relative humidity (p_{H_2O}/p_{sat}) at the GDL/CL interface at the cell voltage of 0.45 (thin line) and 0.5 V (bold line) for the base case and case considering the inhomogeneous compression.

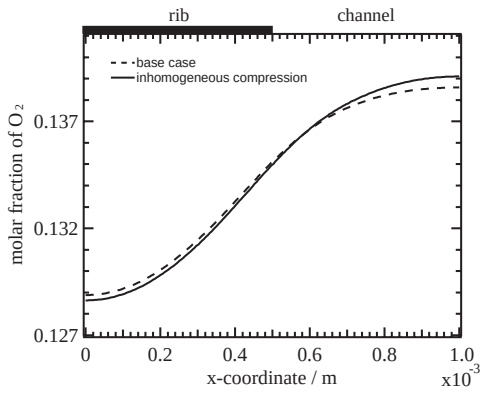

Fig. 5 Oxygen molar fraction at the GDL/CL interface at cell voltage of 0.5 V.

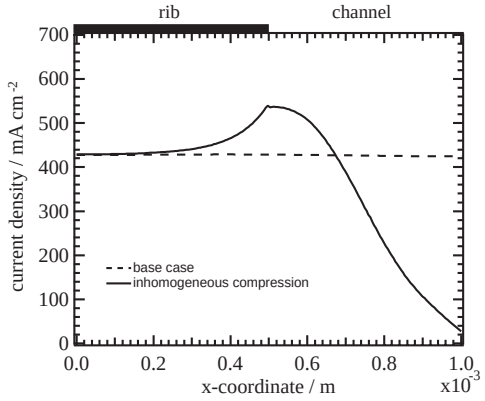

Fig. 6 Current density distribution at the GDL/CL interface at cell voltage of 0.5 V.

under the channel in ref. [59]. GDL parameters have an effect on the location of the current density distribution. Pharoah et al. [33] and Sun et al. [56] found that depending on the electrical conductivity of GDL, the region of higher reaction rate may occur either under the rib or under the channel.

3.3 Temperature Profile

Figure 8 shows the temperature profile at the GDL/CL interface. The local temperature of the CL surface is determined by several factors, including current density distribution, GDL gas permeability, thermal bulk resistances of components and thermal contact resistances between them. It is interesting to note that when inhomogeneous compression is taken into account the temperature profile is more uniform than that of the base case. A possible reason for this is that the current density under the channel is substantially smaller when inhomogeneous compression is taken into account than in the base case (see Figure 6). All the terms of the heat source equation include current density, and thus the current density distribution directly affects the temperature profile. Among the heat sources, the irreversible heat of electrochemical reactions accounts for a major part of heat production.

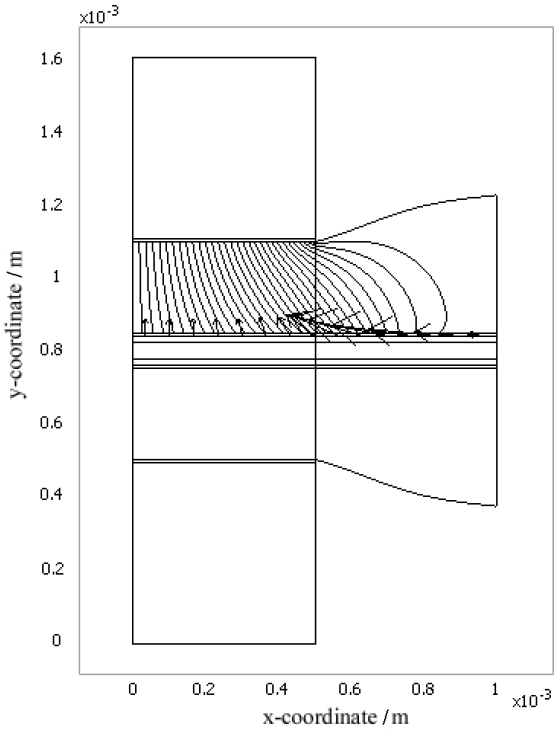

Fig. 7 Current density profile at TH2/CL interface (arrow plot) and at cathode GDL (streamline plot). Note that the magnitudes of arrow and streamline plots are not in scale.

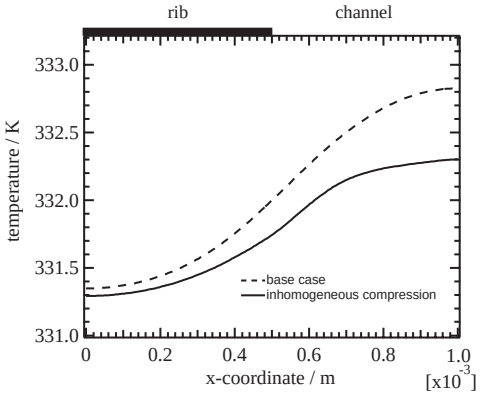

Fig. 8 Temperature distribution at the GDL/CL interface at cell voltage of 0.5 V.

For inhomogeneous compression, the temperature difference across the active area is less than 1 °C, which is much smaller than the value, more than 10 °C, predicted in a previous study [68]. There, the values for the thermal contact and thermal bulk resistances were overestimated and the values of electric contact resistances between GDL and CL were underestimated, leading to larger temperature differences across the components.

3.4 Effect of the Compressed GDL Thickness

Applying the simulation technique described above, the effects of compressed GDL thickness on charge and heat transport were investigated. The thickness of the compressed GDL under the rib was varied from 300 to 150 μm, and a corresponding expression for the shape of the GDL intruding into the channel was used. The physical properties of the GDL were changed correspondingly.

Figure 9(a) shows the current density distribution at the GDL/CL interface for various compressed GDL thicknesses under the rib. The total current integrated over the active area increases as the GDL is compressed more, since both the electric contact and bulk resistances of GDL are reduced. For example, the case in which the GDL is compressed to 150 μm produces ca. 25% more current than the case of 300 μm at the same cell voltage of 0.5 V. The shape of the current density distribution also changes when the compressed GDL thickness is changed. A current density peak is observed at the edge of the rib when the GDL is compressed to 300 μm. On the other hand, when the GDL under the rib is compressed to 150 μm the current density has a maximum at around x = 0.61 mm. In this case, the contact resistance between GDL and CL is small enough even under the channel so that lateral current flows in the CL change the direction and enter into the GDL. The shape of the current density distribution is largely determined by the profile of the deformed GDL on which the contact resistance between the GDL and CL depends.

Figure 9(b) shows the temperature profile at the GDL/CL interface for various compressed GDL thicknesses under the rib. As predicted in a previous study [72], the temperature under the rib increases on decreasing the compression because of an increase in both thermal bulk and contact resistance. However, the temperature profile becomes more uniform over the active area when the GDL under the rib is less compressed. This is due to lesser heat production under the channel in such a case. Since the value of oxygen molar fraction depends on the porosity of GDL, i.e. the shape of GDL, lower compression of GDL leads to a relatively higher value of oxygen molar fraction compared to the case of higher compression, which in turn results in a lower value of overpotential in CL. Even though the differences in their values are fairly small (ca. less than 2% for both oxygen molar fraction and overpotential), changes in heat production are notable.

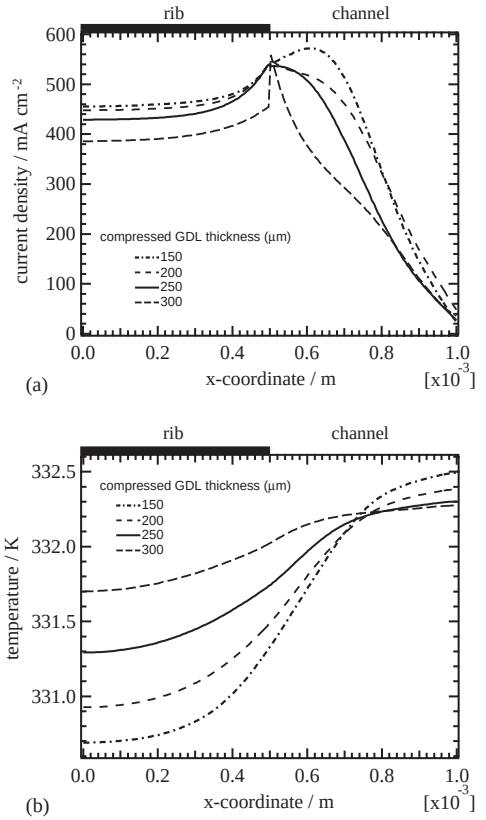

Fig. 9 (a) Current density distribution and (b) temperature profile at the GDL/CL interface at cell voltage of 0.5 V with various compressed GDL thickness (150–300 μm) under the rib.

For example, the irreversible heat of electrochemical reactions when the compressed GDL thickness is 200 μm is ca. 23% higher than that for the case of 300 μm on an average over the active area.

The minor irregularities in the shape of the current density distribution under the channel [Figure 9(a)], such as variation in the value of current density in the middle of the channel and crossing of the current density curves for the GDLs compressed to 150 and 200 μm at around x = 0.81 mm, stem from the difficulty in determining the profile of the GDL intrusion into the channel $h(x)$, i.e. the equivalent of Eq. (17) for each compressed GDL thickness under the rib. Due to the structure of the GDL, the profile of the deformed part and the uncompressed GDL thickness under the channel varied from sample to sample in the photomicrographs taken at the same compressed thickness under the rib. Therefore, the expressions for $h(x)$ are unique for each sample and compressed thickness, which is in turn reflected in the current density profiles.

4 Summary and Conclusions

A two-dimensional model was developed to study the effect of inhomogeneous compression of GDL on the local transport phenomena in PEM fuel cell. The results were compared to those given by a base case model in which the GDL compression was assumed to be homogeneous.

The polarisation behaviour and gas-phase mass transport predicted by the two models were almost identical, but the current density profiles were noticeably different. The model which considered the inhomogeneous compression showed that the local current density under the channel was substantially smaller than under the rib and had a maximum at the edge of the rib, while the current density for the base case was fairly uniform over the active area. This high variation in local current density may significantly accelerate membrane deterioration and affect the cell durability.

The model predicted a fairly uniform temperature profile over the active area, with a maximum variation of ca. 1 °C. This contradicts the results of a previous study [68], where a larger temperature variation, up to 10 °C, was predicted within the cell under similar conditions. This difference stems from the adopted modelling parameters such as contact resistance and conductivity, and the geometry of the deformed GDL. Especially, the local current density distribution, which significantly affects the temperature profile, was found to be very sensitive to the value and variation of contact resistance between GDL and CL. Each GDL has unique physical properties, see, ref. [29, 32] and thus, the right choice of modelling parameters is essential for accurate prediction of local phenomena which cannot be easily interpreted by the modelled polarisation curves only, as discussed in the literature [69-71].

The compressed GDL thickness under the rib affects the current density distribution and temperature profile. Although the total current over the active area increased as GDL was compressed more, the unevenness of the temperature profiles became more prominent. Further effort should be made to mitigate the detrimental effects of inhomogeneous compression of GDL, e.g. by developing rigid GDLs or rigid microporous layers onto the GDL which do not deform under compression, or implementing pre-treatment which curbs or compensates for the deformation of the GDL.

A limitation of the model presented here is that phase change of water and liquid water transport are not considered. When the cell is flooded by the condensed water, gas transport is significantly hindered, which in turn affects the current production and temperature distribution. A further study using proper water transport parameters is left for the future.

Acknowledgements

The authors gratefully acknowledge the financial support from the Fortum Foundation, the Academy of Finland (decision no. 110748), the Wihuri Foundation and Tekes, the Finnish Funding Agency for Technology and Innovation.

Nomenclature

a_v	Ratio of reaction surface to CL volume (m^{-1})
c	Concentration (mol m^{-3})
C_p	Heat capacity (J kg^{-1} K^{-1})
D	Diffusion coefficient (m^2 s^{-1})
F	Faraday constant, 96,487 (A s mol^{-1})
h	Thickness (m)
j	Transfer current density (A m^{-3})
j^{ref}	Exchange current density (A m^{-2})
k	Permeability (m^2)
M	Molar mass (kg mol^{-1})
$\mathbf{n}$	Unit vector
$\mathbf{N}$	Molar flux (mol m^{-2} s^{-1})
p	Pressure (Pa)
Q	Heat flux (W m^{-2})
R	Gas constant, 8.314 (J mol^{-1} K^{-1})
S	Source term
T	Temperature (K)
$\mathbf{v}$	Velocity (m s^{-1})
X	Molar fraction

Greek Letters

α	Transfer coefficient
ε	Porosity
η	Overpotential (V)
κ	Thermal conductivity (W m^{-1} K^{-1})
μ	Viscosity of air, 1.9×10^{-5} (kg m^{-1} s^{-1})
ρ	Density (kg m^{-3})
σ	Electric conductivity (Ω^{-1} m^{-1})
φ	Potential (V)

Subscripts

a	Anode
c	Cathode
CL	Catalyst layer
GDL	Gas diffusion layer
GR	Graphite
H_2O	Water
i	Species of gas
m	Ionic phase
N_2	Nitrogen
O_2	Oxygen
s	Electric phase
sat	Saturation
sd	Subdomain
t	Mixture of gas
TH1	Thin layer 1
TH2	Thin layer 2
x	x-Direction, in-plane
y	y-Direction, through-plane

References

[1] K. Z. Yao, K. Kran, K. B. McAuley, P. Oosthuizen, B. Peppley, T. Xie, *Fuel Cell* **2004**, *4*, 3.
[2] M. Mathias, J. Roth, J. Fleming, W. Lehnert, in *Handbook of Fuel Cells* (Eds. W. Vielstich, A. Lamm, H. Gasteiger), John Wiley & Sons Ltd., New York, **2003**, pp. 517.
[3] H. Dohle, R. Jung, N. Kimiaie, J. Mergel, M. Müller, *J. Power Sources* **2003**, *124*, 371.
[4] V. Gurau, M. J. Bluemle, E. S. De Castro, Y.-M. Tsou, T. A. Zawodzinski, J. A. Mann., *J. Power Sources* **2007**, *165*, 793.
[5] J. T. Gostick, M. W. Fowler, M. D. Pritzker, M. A. Ioannidis, L. M. Behra, *J. Power Sources* **2006**, *162*, 228.
[6] J. P. Feser, A. K. Prasad, S. G. Advani, *J. Power Sources* **2006**, *162*, 1226.
[7] M. V. Williams, E. Begg, L. Bonville, H. R. Kunz, J. M. Fenton, *J. Electrochem. Soc.* **2004**, *151*, A1173.
[8] J. Soler, E. Hontanon, L. Daza, *J. Power Sources* **2003**, *118*, 172.
[9] S. A. Freunberger, M. Reum, J. Evertz, A. Wokaun, F. N. Büchi, *J. Electrochem. Soc.* **2006**, *153*, A2158.
[10] T. Tomimura, S. Nakamura, H. Nonami, H. Saito, *2001 IEEE 7th International Conference on Solid Dielectrics*, Eindhoven, Netherlands **2001**, 101.
[11] V. Mishra, F. Yang, R. Pitchumani, *J. Fuel Cell Sci. Technol.* **2004**, *1*, 2.
[12] J. Ihonen, F. Jaouen, G. Lindbergh, G. Sundholm, *Electrochim. Acta* **2001**, *46*, 2899.
[13] P. M. Wilde, M. Mandle, M. Murata, N. Berg, *Fuel Cells* **2004**, *4*, 180.
[14] Cunningham, M. Lefévre, G. Lebrun, J. P. Dodelet, *J. Power Sources* **2005**, *143*, 93.
[15] M. Khandelwal, M. M. Mench, *J. Power Sources* **2006**, *161*, 1106.
[16] P. J. S. Vie, S. Kjelstrup, *Electrochim. Acta* **2004**, *49*, 1069.
[17] J. Ihonen, M. Mikkola, G. Lindbergh, *J. Electrochem. Soc.* **2004**, *151*, A1152.
[18] J. T. Gostick, M. W. Fowler, M. A. Ioannidis, M. D. Pritzker, Y. M. Volfkovich, A. Sakars, *J. Power Sources* **2006**, *156*, 375.
[19] V. Gurau, M. J. Bluemle, E. S. D. Castro, Y.-M. Tsou, J. A. Mann, Jr., T. A. Zawodzinski, Jr., *J. Power Sources* **2006**, *160*, 1156.
[20] S. Litster, D. Sinton, N. Djilali, *J. Power Sources* **2006**, *154*, 95.
[21] A. Bazylak, D. Sinton, Z. S. Liu, N. Djilali, *J. Power Sources* **2007**, *163*, 784.
[22] N. Holmström, J. Ihonen, A. Lundblad, G. Lindbergh, *Fuel Cells* **2007**, *7*, 306.
[23] J. Benziger, J. Nehlsen, D. Blackwell, T. Brennan, J. Itescu, *J. Membr. Sci.* **2005**, *261*, 98.
[24] E. C. Kumbur, K. V. Sharp, M. M. Mench, *J. Power Sources* **2006**, *161*, 333.
[25] E. C. Kumbur, K. V. Sharp, M. M. Mench, *J. Power Sources* **2008**, *176*, 191.
[26] E. C. Kumbur, K. V. Sharp, M. M. Mench, *J. Electrochem. Soc.* **2007**, *154*, B1295.
[27] E. C. Kumbur, K. V. Sharp, M. M. Mench, *J. Electrochem. Soc.* **2007**, *154*, B1305.
[28] E. C. Kumbur, K. V. Sharp, M. M. Mench, *J. Electrochem. Soc.* **2007**, *154*, B1315.
[29] W. K. Lee, C. H. Ho, J. W. V. Zee, M. Murthy, *J. Power Sources* **1999**, *84*, 45.
[30] J. Ge, A. Higier, H. Liu, *J. Power Sources* **2006**, *159*, 922.
[31] S. Escribano, J. F. Blachot, J. Etheve, A. Morin, R. Mosdale, *J. Power Sources* **2006**, *156*, 8.
[32] W. R. Chang, J. J. Hwang, F. B. Weng, S. H. Chan, *J. Power Sources* **2007**, *166*, 149.
[33] J. G. Pharoah, K. Karan, W. Sun, *J. Power Sources* **2006**, *161*, 214.
[34] T. Zhou, H. Liu, *J. Power Sources* **2006**, *161*, 444.
[35] H. Meng, C. Y. Wang, *J. Electrochem. Soc.* **2004**, *151*, A358.
[36] J. H. Jang, W. M. Yan, C. C. Shih, *J. Power Sources* **2006**, *156*, 244.
[37] G. Inoue, Y. Matsukuma, M. Minemoto, *J. Power Sources* **2006**, *154*, 8.
[38] D. Natarajan, T. V. Nguyen, *J. Electrochem. Soc.* **2001**, *148*, A1324.
[39] J. H. Jang, W. M. Yan, C. C. Shih, *J. Power Sources* **2006**, *161*, 323.
[40] Z. Liu, Z. Mao, C. Wang, *J. Power Sources* **2006**, *158*, 12299.
[41] H. S. Chu, C. Yeh, F. Chen, *J. Power Sources* **2003**, *123*, 1.
[42] J. T. Gostick, M. A. Ioannidis, M. W. Fowler, M. D. Pritzker, *J. Power Sources* **2007**, *173*, 277.
[43] J. G. Pharoah, *J. Power Sources* **2005**, *144*, 77.
[44] A. S. Rawool, S. K. Mitra, J. G. Pharoah, *J. Power Sources* **2006**, *162*, 985.
[45] X. D. Niu, T. Munekata, S. A. Hyodoa, K. Suga, *J. Power Sources* **2007**, *172*, 542.
[46] J. H. Nam, M. Kaviany, *Int. J. Heat Mass Transfer* **2003**, *46*, 4595.
[47] U. Pasaogullari, C. Y. Wang, *Electrochim. Acta* **2004**, *49*, 4359.
[48] U. Pasaogullari, C. Y. Wang, *J. Electrochem. Soc.* **2004**, *151*, A399.
[49] X. Zhu, P. C. Sui, N. Djilali, *J. Power Sources* **2007**, *172*, 287.
[50] P. C. Sui, N. Djilali, *J. Power Source* **2006**, *161*, 294.
[51] V. P. Schulz, J. Becker, A. Wiegmann, P. P. Mukherjee, C. Y. Wang, *J. Electrochem. Soc.* **2007**, *154*, B419.
[52] L. Zhang, Y. Liu, H. Song, S. Wang, Y. Zhou, S. J. Hu, *J. Power Sources* **2006**, *162*, 1165.
[53] P. Zhou, C. W. Wu, G. J. Ma, *J. Power Sources* **2006**, *159*, 1115.
[54] P. Zhou, C. W. Wu, *J. Power Sources* **2007**, *170*, 93.
[55] P. Zhou, C. W. Wu, G. J. Ma, *J. Power Sources* **2007**, *163*, 874.
[56] W. Sun, B. A. Peppley, K. Karan, *J. Power Sources* **2005**, *144*, 42.

[57] I. Nitta, T. Hottinen, O. Himanen, M. Mikkola, *J. Power Sources* **2007**, *171*, 26.
[58] I. Nitta, O. Himanen, M. Mikkola, *Electrochem. Commun.* **2008**, *10*, 47.
[59] T. Hottinen, O. Himanen, S. Karvonen, I. Nitta, *J. Power Sources* **2007**, *171*, 113.
[60] Y. Wang, C. Y. Wang, *J. Electrochem. Soc.* **2005**, *152*, A445.
[61] D. M. Bernardi, M. W. Verbrugge, *J. Electrochem. Soc.* **1992**, *139*, 2477.
[62] O. Himanen, T. Hottinen, M. Mikkola, V. Saarinen, *Electrochim. Acta* **2006**, *52*, 206.
[63] Manufacture's data sheet for ISEM-3 graphite by Svenska Tanso AB.
[64] S. Cleghorn, J. Kolde, W. Liu, in Handbook of Fuel Cells (Eds., W. Vielstich, A. Lamm, H. Gasteiger), John Wiley & Sons Ltd., New York, **2003**, pp. 566.
[65] Manufacturer's Data Sheet for ®Sigracet GDL 10 BA by SGL Carbon AG.
[66] W. Sun, B. A. Peppley, K. Karan, *Electrochim. Acta* **2005**, *50*, 3359.
[67] D. Natarajan, T. V. Nguyen, *J. Power Sources* **2003**, *115*, 66.
[68] T. Hottinen, O. Himanen, *Electrochem. Commun.* **2007**, *9*, 1047.
[69] W. Q. Tao, C. H. Min, X. L. Liu, Y. L. He, B. H. Yin, W. Jiang, *J. Power Sources* **2006**, *160*, 359.
[70] C. H. Min, Y. L. He, X. L. Liu, B. H. Yin, W. Jiang, W. Q. Tao, *J. Power Sources* **2006**, *160*, 374.
[71] H. Ju, C. Y. Wang, *J. Electrochem. Soc.* **2004**, *151*, A1954.
[72] I. Nitta, O. Himanen, M. Mikkola, Thermal Conductivity and Contact Resistance of Compressed Gas Diffusion Layer of PEM Fuel Cell, *Fuel Cells* **2008**, *2*, 111.

PUBLICATION 4

Modeling of polymer electrolyte membrane fuel stack end plates

In: Journal of Fuel Cell Science and Technology 5(4),
art. no. 041009-1.

Modeling of Polymer Electrolyte Membrane Fuel Cell Stack End Plates

Suvi Karvonen
Laboratory of Advanced Energy Systems,
Helsinki University of Technology,
P.O. BOX 2200,
FIN-02015 TKK, Finland

Tero Hottinen
Wärtsilä Finland Oyj,
Tekniikantie 14,
02150 Espoo, Finland

Jari Ihonen

Heidi Uusalo

VTT Technical Research Centre of Finland,
P.O. Box 1601,
FI-02044 VTT, Finland

Good thermal and electric contacts of gas diffusion layers (GDLs) with electrode surface and flow-field plates are important for the performance of a polymer electrolyte membrane fuel cell (PEMFC). These contacts are dependent on the compression pressure applied on the GDL surface. The compression also affects the GDL porosity and permeability, and consequently has an impact on the mass transfer in the GDL. Thus, the compression pressure distribution on the GDL can have a significant effect on the performance and lifetime of a PEMFC stack. Typically, fuel cell stacks are assembled between two end plates, which function as the supporting structure for the unit cells. The rigidity of the stack end plates is crucial to the pressure distribution. In this work, the compression on the GDL with different end plate structures was studied with finite element modeling. The modeling results show that more uniform pressure distributions can be reached if ribbed-plate structures are used instead of the traditional flat plates. Two different materials, steel and aluminum, were compared as end plate materials. With a ribbed aluminum end plate structure and a certain clamping pressure distribution, it was possible to achieve nearly uniform pressure distribution within 10–15 bars. The modeling results were verified with pressure-sensitive film experiments.
[DOI: 10.1115/1.2930775]

Keywords: PEM fuel cell stack, end plates, compression, modeling

1 Introduction

The type of fuel cell under study in this paper is the polymer electrolyte membrane (a.k.a. proton exchange membrane) fuel cell, PEMFC. PEMFC is a low temperature fuel cell that typically operates in the temperature range of liquid water, although membranes that allow operation in higher temperatures have also been developed. PEMFCs are typically suitable for small-scale applications ranging from portable electronics to automobiles and distributed energy and heat production for houses and apartments. In order to make PEMFCs economically competitive and thus achieve large-scale fuel cell commercialization, the efficiency and lifetime of the cell must be maximized while the cost should be strongly reduced.

The operating voltage of a single PEMFC, less than 1 V, is low for most practical applications. Consequently, in a typical PEMFC power source, many cells are connected in series. Usually, the structure of PEMFCs is planar and thus the cells are stacked on top of each other; this arrangement is known as a fuel cell stack. Each unit cell in the stack has the following components: a solid electrolyte membrane and two electrodes that are usually integrated into a single component known as membrane electrode assembly (MEA), two gas diffusion layers (GDLs), two flow-field plates that can also be combined as a two-sided flow-field plate known as the bipolar plate, and insulation structures. The unit cells are inserted between end plates and the whole structure is fastened with a bolt assembly. A stack usually has also a cooling system so that the heat produced in the cells can be removed efficiently.

Good cell operation requires that the clamping pressure in each cell is approximately equal. The clamping pressure should also be distributed across the GDLs as evenly as possible since the attributes of the GDL are dependent on the compression pressure. The higher the pressure on the GDL is, the smaller are the thermal and electric contact resistances between the interfaces of the GDL with the electrode and flow-field plate. Typically, a compression pressure of 10 bars is sufficient for low contact losses as the contact resistances do not significantly decrease after that, see, e.g., Refs. [1,2]. On the other hand, high compression pressure decreases GDL porosity, which reduces its gas permeability and thus increases mass transfer limitations. As a consequence, the GDL porosity can have a significant effect on cell performance, see, e.g., Ref. [3]. The optimal pressure depends on the gas diffusion material and to some extent on cell operating parameters such as temperature or humidity of the inlet gases. Even pressures up to 30 bars on the rib area can be used for some materials [1]. However, as a compression of 10 bars is typically sufficient for contacts and excess compression causes mass transfer limitations, it is assumed here that a pressure distribution between 10 and 20 bars is sufficient, and 10 and 15 bars is ideal.

The local (under rib or channel) and regional (whole cell area) pressure distributions on the MEA and GDL are influenced by the dimensions, geometrical shape, and material of the stack components. The most important components in terms of the regional pressure distribution are usually the end plates, which should be as rigid as possible so that the clamping pressure of the bolt assembly that is typically located around the edges of the end plates is distributed across the whole cell area. From the manufacturing point of view, high rigidity is easily accomplished by making a simple thick flat plate. However, such a plate has large mass/volume, which results in a heavy/bulky stack. This is a serious disadvantage in most practical applications. Low mass and high rigidity can be simultaneously accomplished by using more complex end plate configurations such as ribbed structures. A ribbed structure is, in principle, a relatively thin flat plate with supporting ribs added to its surface. An interesting alternative to these high rigidity end plates is presented by curved shapes, more specifically curved end plates or additional curved layers inserted directly below the end plates such as described, e.g., in Ref. [4]. The curved component straightens when pressure is applied to the as-

Manuscript received October 31, 2006; final manuscript received October 19, 2007; published online September 9, 2008. Review conducted by Michael von Spakovsky.

sembly and thus produces an even pressure distribution if the original radius of curvature was suitably chosen for the used compression. However, this alternative requires high design and manufacturing accuracy in order to function properly. In this paper, the focus is on ribbed end plate structures.

The end plate material has a large influence on the mechanical properties of the end plate. A good end plate material has a high Young's modulus and a low density. Possible materials for end plates include, for example, steel, aluminum, and composite materials. In this work, two different materials, steel and aluminum, are compared. Steel has a high Young's modulus, typically approximately 200 GPa, but its density is also relatively high ($7600\ \mathrm{kg\,m^{-3}}$). Aluminum has a significantly lower Young's modulus, ~70 GPa, but on the other hand its density is also lower ($2700\ \mathrm{kg\,m^{-3}}$). If the end plate functions only as a supporting structure, other qualities such as corrosion characteristics or electric properties can be ignored, and the better choice of these two materials is the one that at a certain mass makes a more rigid end plate than the other one.

In this work, the stack assembly pressure distribution is studied using numerical analysis. The models were solved using a commercial partial differential equation solver, COMSOL MULTIPHYSICS® (formerly known as FEMLAB®) that employs the generally used finite element method (a.k.a. finite element analysis). The models made and solved in this work are based on the design of an existing fuel cell stack that is developed in the POWERPEMFC-project funded by the National Technology Agency of Finland (TEKES).

Earlier numerical studies on the pressure distribution and component deformation of a single cell have been made, e.g., by Lee et al. [5]. In their work, the modeled pressure distributions were clearly uneven so that the compression pressure on the middle area was significantly lower than on the edges. In this work, a significant improvement in the pressure distribution is accomplished by changing the plate structure from flat to ribbed plate. At the same time, the end plate mass is also significantly reduced.

2 Theory

The state of stress in an object is represented by the stress tensor σ as follows:

$$\sigma = \begin{bmatrix} \sigma_x & \tau_{xy} & \tau_{xz} \\ \tau_{xy} & \sigma_y & \tau_{yz} \\ \tau_{xz} & \tau_{yz} & \sigma_z \end{bmatrix} \tag{1}$$

which consists of the normal stresses σ_i and shear stresses τ_{ij}. Here, it is assumed that adjacent shear stresses are equal, $\tau_{ij}=\tau_{ji}$, which applies for most materials. For an object in equilibrium state with no volume forces acting on it, the stress tensor obeys the following differential equation, see, e.g., Ref. [6]:

$$\nabla \cdot \sigma = 0 \tag{2}$$

The stress tensor is often written in vector notation as $\sigma = (\sigma_x, \sigma_y, \sigma_z, \tau_{xy}, \tau_{yz}, \tau_{xz})^T$. With this formulation, the stress tensor in an elastic material can be calculated from the strain tensor $\varepsilon = (\varepsilon_x, \varepsilon_y, \varepsilon_z, \gamma_{xy}, \gamma_{yz}, \gamma_{xz})^T$ by Hooke's law as follows:

$$\sigma = D\varepsilon \tag{3}$$

where D is the elasticity matrix. Here, it is assumed that there are no initial stresses or strains that can occasionally be created during the manufacturing process in the materials. The elasticity matrix is calculated using Young's modulus E and Poisson's ratio ν as follows:

$$D = \frac{E}{(1+\nu)(1-2\nu)} \begin{bmatrix} 1-\nu & \nu & \nu & 0 & 0 & 0 \\ \nu & 1-\nu & \nu & 0 & 0 & 0 \\ \nu & \nu & 1-\nu & 0 & 0 & 0 \\ 0 & 0 & 0 & \frac{1}{2}-\nu & 0 & 0 \\ 0 & 0 & 0 & 0 & \frac{1}{2}-\nu & 0 \\ 0 & 0 & 0 & 0 & 0 & \frac{1}{2}-\nu \end{bmatrix} \tag{4}$$

The derivation of D can be found in many structural mechanics books, see, e.g., Ref. [7], and is thus not repeated here. In this work, all materials are approximated as elastic, isotropic, and homogeneous so that the material parameters E and ν are constant in each component. Thermal stresses due to a temperature difference caused by the heat production of the operating fuel cell are excluded since the operating temperature of the PEMFC is typically less than 373 K. Temperature differences within the unit cells are usually at largest 20 K, see, e.g., Ref. [8]. Some error is likely introduced to the modeled GDL pressure distributions due to the assumption of constant material parameters. In reality, the composite material of the flow-field plates is not isotropic and the elastic approximation is not entirely valid for some of the materials, such as the carbon paper of the GDLs. However, the approximations are valid for the metallic end plates that have the largest influence on the pressure distributions throughout the stack. Thus, the results given by the model should be good approximations of the real situation.

The strain ε is a measure of the material's deformation that is calculated by dividing the change in length at a certain point by the original length at that point. The components of the strain tensor ε are calculated from the deformation vector, $\mathbf{u}=u\mathbf{i}+v\mathbf{j}+w\mathbf{k}$, as follows:

$$\varepsilon_i = \frac{\partial \mathbf{u}_i}{\partial i} \tag{5}$$

$$\gamma_{ij} = \frac{\partial \mathbf{u}_j}{\partial i} + \frac{\partial \mathbf{u}_i}{\partial j} \tag{6}$$

Using these equations, the following differential equation can be written for the deformation:

$$\nabla \cdot (D\nabla \mathbf{u}) = 0 \tag{7}$$

This is the equation solved with COMSOL MULTIPHYSICS®. The solution consists of the deformation values, from which the stress and strain components can be calculated using Eqs. (3)–(6). The most interesting aspect of the results is the compression pressure on the GDL. It is taken as the z-directional stress component, i.e., σ_z. According to Eqs. (3)–(6), this can be calculated from the deformation components as

$$\sigma_z = \frac{E}{(1+\nu)(1-2\nu)} \left(\nu \frac{\partial u}{\partial x} + \nu \frac{\partial v}{\partial y} + (1-\nu) \frac{\partial w}{\partial z} \right) \tag{8}$$

3 Model Properties

The model geometry was based on an existing fuel cell stack design. However, solving a model that includes each geometrical detail was not possible with the available computing capacity. In order to restrict the number of elements in the models to a reasonable limit, the geometry was simplified by reducing the number of different components and approximating some of the more complex structures with simpler ones.

In the real stack design that was used as a basis for the models in this work, each unit cell consists of the following components:

- two 3 mm thick polymer composite flow-field plates
- two 1 mm thick layers including gasket material (Grafoil®),

Table 1 The values of Young's modulus and Poisson's ratio for the different components

	E (GPa)	υ	Source
Flow-field plate (graph/epoxy)	10	0.25	Estimate, material still in development
Gas diffusion layer	0.06	0.33	Taken the same as in Ref. [5]
Grafoil	1.4	0.25	[9]
Steel	200	0.33	Well known material
Aluminum	70	0.33	Well known material
Rubber	0.1	0.4	Estimate
Steel net	110	0.33	Estimate

gas space, and steel net (part of the gas distribution and cooling systems)
- one ~0.5 mm thick layer including two rubber gaskets for gases, two GDLs (SGL Sigracet 35 BC), and MEA
- one 0.5 mm thick metal (steel) separator plate

The total thickness of a unit cell is thus 9 mm. The cross-sectional area of the end plates and flow-field plates is 258×190 mm^2.

In the modeled stack, each cell was reduced to the following three homogeneous components:

- one 8.5 mm thick plate that includes the two 3 mm flow-field plates, the 0.5 mm metal plate, and the two 1 mm Grafoil® layers with the steel nets
- the two rubber gaskets merged into one component with a simplified geometry
- 0.5 mm layer that represents the two GDLs and MEA.

In addition to reducing the multitude of components to only three, the geometry was simplified by excluding fine geometrical details such as the flow-field pattern (1 mm wide gas channels crossing the cell) and the bolt holes with the bolts set through them. This simplification should be justifiable since the exceptions to symmetry in the flow-field pattern are relatively minor in terms of the cross-sectional area. The curved shape of the rubber insulator was approximated with a polygon. The two material parameters, E and υ, of the two latter components were simply those of rubber and the GDL material (Carbel®). The MEA is relatively thin and flexible so that the GDLs dominate the deformation of the GDL-MEA component. However, the material parameters of the 8.5 mm thick plate formed by many different materials could not be defined as easily. Thus, a separate model was solved to discover the proper values for this component. The rigidity of the flow-field plate–gasket–separator assembly was studied with this model, first with the real E and υ of each separate component and the detailed component geometry, and then with the constant values using the simplified geometry (homogeneous plate with gas and cooling system channels). The result was that with $E = 7.7$ GPa, the deformation behavior of the homogeneous plate was similar to the more detailed model. Poisson's ratio υ was taken as 0.25, since that was the value of all component materials except the relatively thin steel separator plate. The values for E and υ of the different materials are listed in Table 1 and cross-sectional schematics of the real stack and model components are presented in Fig. 1. The error induced by these approximations is studied in a separate section.

Since the channel configurations in the flow-field plates were excluded, the modeled fuel cell stack was a symmetric structure with respect to the center in all three dimensions. Thus, through employment of symmetry boundary conditions, it is sufficient to solve the problem in only one-eighth of the whole stack geometry. The model geometry consists of one-quarter of the cross-sectional area of the cell and one-half of the stack (three cells). On each symmetry boundary, the deformation in the direction normal to the surface is fixed to zero. A schematic of the modeled flat end plate and its symmetry axes are presented in Fig. 2. The compression is directed to the object by setting 1 kN load divided with the area of the used spring washers on each of the circular areas marked in Fig. 2. The bolt holes and the bolts set through them were not included in the models as separate geometrical objects since they complicate the mesh and do not significantly affect the rigidity of the end plates.

The original end plate, whose cross section is illustrated in Fig. 2, was a flat 2 cm thick steel plate that has a weight of 7.1 kg. The two objectives of this work were to lower the end plate mass and simultaneously improve the GDL pressure distribution. In this work, it is assumed that a sufficient GDL pressure distribution is restricted to between 10 and 20 bars, and only those end plate configurations that result in pressure distributions that obey this criterion were recognized as acceptable.

One method of lowering the end plate mass while increasing its rigidity is to reduce the thickness of the plate and then add supporting ribs in a suitable configuration to its surface. The resulting structure is known as a ribbed end plate. The rigidity of a rib with a square cross section is proportional to the third power of its height d but only directly proportional to its width b, see, e.g., Ref. 7:

$$I = \tfrac{1}{12} b d^3 \tag{9}$$

Thus, a high and thin rib will be more rigid than a low and wide one that has the same volume. In practice, the manufacturing process and the possible applications of the stack limit the dimensions of the ribs.

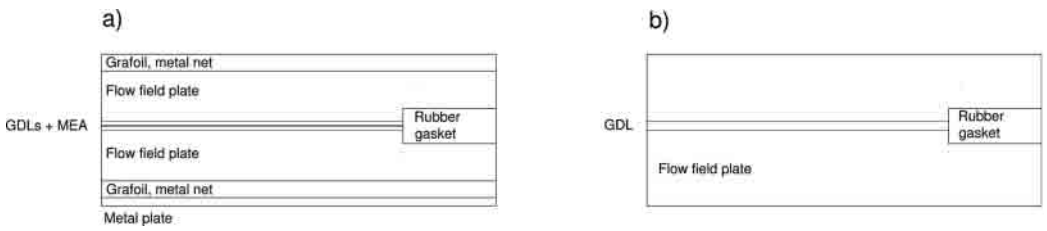

Fig. 1 A cross-sectional schematic of the unit cell components in (*a*) a real stack and (*b*) the approximative model

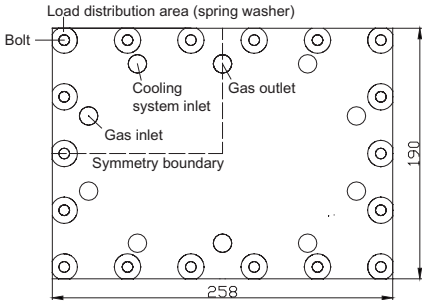

Fig. 2 A top (*x*,*y*-plane) view of the flat end plate structure. The dimensions are in millimeters.

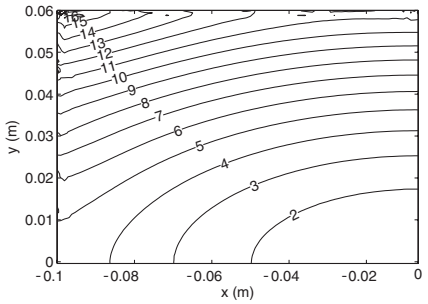

Fig. 4 The clamping pressure isobars on the GDL surface of the original flat plate with 1 kN load at each bolt. The pressure values are in bars. The origin (lower right corner) corresponds to the point of symmetry.

The geometric possibilities for the placement, thickness, and width of the ribs are infinite. However, the ribs cannot cross the gas and cooling system inlets and outlets. Furthermore, setting the ribs from one bolt to another improves the load distribution across the whole area, and thus the number of possible rib structures can be decreased to such geometries only. In this work, the search for the best geometry was limited to three alternative rib structures illustrated in Fig. 3. Modeling these structures revealed that Structure (*b*) in Fig. 3 was the most promising one. Structure (*a*) is the most simple to manufacture and has the lightest weight, but its pressure distribution is only slightly better than that of the original flat plate. Structure (*c*) has the best pressure distribution, but not significantly better than Structure (*b*). Therefore, because Structure (*c*) is clearly heavier than Structure (*b*), the latter would appear to be the most advantageous choice and was accordingly chosen for further study. Different rib widths and heights were tested with both steel and aluminum and the results for the best structures are presented in the next chapter.

The geometry was meshed with tetrahedral elements. Because the GDL-MEA component is very thin compared to its length and width, the mesh elements were flattened in the *z*-direction. The used values for the scaling factor, i.e., the height of the normal element divided by the height of flattened element, varied between 2.5 and 3.5. This mesh manipulation reduced the number of elements from 300,000 to 70,000–95,000 elements depending on the geometry. When different scaling factors between 2 and 4 were tested, the differences between the corresponding GDL pressure distributions were in the range of 2% and this is likely due more to the differences in the total number of elements than the scaling. Thus, scaling the mesh should not affect the results significantly. The calculations were performed over a 64 bit COMSOL MULTIPHYSICS® client-server connection. The server computer was an AMD Athlon64 3500+ with 4 Gbyte random access memory (RAM) and 40 Gbytes of swap space. The operating system was SuSe 9.1 AMD64 Linux. With this equipment, a model was usually solved in a few hours.

4 Results

The pressure distribution data were taken from the middle (in *z*-direction) of the GDLs. Unless mentioned otherwise, the results were taken from the second cell from the end plates. The results for the flat end plate with constant 1 kN point loads are illustrated in Fig. 4. The compression pressure isobars are curved and the largest pressure, approximately 16 bars, is found in the left upper corner that corresponds to the four outer corners of the GDL. In contrast, at the lower right corner, i.e., the middle area of the GDL, the pressure values are much lower, close to 1 bar. The pressure map illustrated in Fig. 4 represents the average pressure values over several channel widths. The disturbances on the top and left edges are caused by contact of the GDL with the rubber gasket at the interface boundaries, where the deformation of the rubber affects the stresses in the GDL. The pressure values are more easily read from Fig. 5, where the values are taken along the diagonal of the GDL (from upper left corner to lower right corner in Fig. 4).

If the disturbances close to the rubber gasket–GDL interface are ignored, the pressure distribution is a monotonous function as can be seen from Fig. 5. The compression pressure is at maximum in the outer corner of the GDL. This is in accordance with previous results such as those presented by Lee et al. [5]. The maximum and minimum pressures are 16.5 bars and 1.1 bars, respectively. The compression pressure at the middle regions of the GDL is very small, than 2 bars, and only 6.7% of the pressure at the outer corner, whereas optimal cell performance can be assumed to require at least 10 bars and a significantly more homogeneous pressure distribution. Smaller pressures are likely to cause high thermal and electric contact resistances, which decrease the cell performance and can cause heat removal problems, which can significantly shorten the lifetime of the cell. These results suggest that significant improvement in cell performance could be achieved if the unsatisfactory GDL pressure distribution could be made more even by modifying the end plate structure.

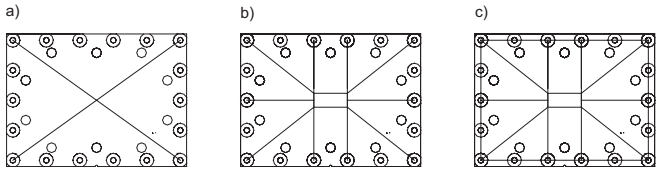

Fig. 3 Schematic representations of three different rib structures: (*a*) the two-rib, (*b*) the ten-rib, and (*c*) the edge-supported ten-rib structures.

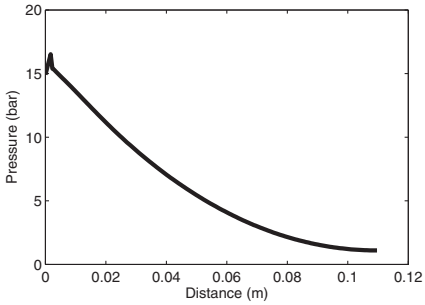

Fig. 5 The diagonal GDL pressure values of the flat plate structure with 1 kN load at each bolt

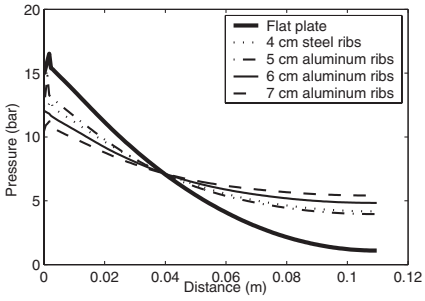

Fig. 7 The diagonal GDL pressure values of the studied steel and aluminum structures with 1 kN load at each bolt

As mentioned in Sec. 3, the best structure of the choices considered here is the ten-rib structure illustrated in Fig. 3(*b*). This structure was tested with both steel and aluminum. Steel has a larger Young's modulus than aluminum (see Table 1), which makes steel structures more rigid. On the other hand, aluminum is much lighter than steel and thus larger amounts of aluminum can be used without the end plate mass growing too large. The cross sections of the ten-rib structures used with steel and aluminum are illustrated in Fig. 6. The difference between the two structures is that the aluminum bars are wider and higher than those of the steel structure since aluminum is less rigid and has a lighter density. Note that the ten-rib configurations used here are not necessarily the optimal ones, but ones that were found to be sufficiently rigid for use in the stack studied in this work.

The GDL pressure distribution results for the steel and aluminum ten-rib structures are illustrated in Fig. 7. These data show that the best result, i.e., the most even GDL pressure distribution, is achieved with 7 cm high aluminum ribs. Nevertheless, the pressure distributions achieved with the other structures are also significantly better than that of the original flat steel plate. The most uneven compression is achieved with the 5 cm high aluminum ribs and the 4 cm high steel ribs. If higher or wider steel ribs were made, a better distribution would be gained, but this would increase the end plate mass over the original 7.1 kg limit. The pressure isobars of the best structure, the 7 cm aluminum rib structure, are illustrated in Fig. 8. The shape of the isobars has changed from the nearly elliptical ones of the flat plate in Fig. 4 closer to linear.

None of the pressure distribution curves presented in Fig. 7 is in the desired 10–20 bar range. This is due to the fact that the 1 kN load at each bolt is insufficient. For this reason, the loads were increased. Another consideration is that using the same load at each bolt does not give an optimal pressure distribution. This can be seen also in Fig. 8, where the shape of the pressure isobars suggests that the loads at the bolts at the middle of the edges are too small compared to the loads at the corner bolts. Increasing the loads at the middle of the edges and decreasing them at the corners should flatten the GDL pressure distribution. Different loads were tested through a trial-and-error method until the desired GDL pressure range was achieved. The shape of the pressure isobars was also monitored. Ideally, the isobars should be rectangular.

The results accomplished with bolt load variation are illustrated in Fig. 9. The 7 cm aluminum structure gives the best results with 10–15 bar GDL pressure range and the original objective; 10–20 bar is satisfied with the 4 cm steel and 5 cm aluminum structures. The GDL pressure isobars of the different structures are presented in Fig. 10. Unlike in Fig. 8 with the constant 1 kN bolt load, the pressure isobars are no longer close to linear. Instead, the curves loosely follow the rectangular shape of the GDL. Comparison of Figs. 10(*a*)–10(*d*) confirms that the 7 cm aluminum rib structure has the most even GDL pressure distribution.

It should be noted that the pressure distributions in the different cells of the stack have some differences. The GDLs of the cells closest to the end plates have the most uneven pressure distribution while the GDLs of the cells in the middle of the stack experience compression more evenly. This effect is illustrated in Fig. 11, where the pressure distributions in three cells with 7 cm aluminum rib end plate can be compared to each other.

The masses of the different structures are listed in Table 2 along with the corresponding GDL pressure ranges. As can be seen in Table 2, the 7 cm aluminum structure that had the best pressure distributions weighs 3.7 kg, whereas the 4 cm steel structure weighs 6.5 kg. Consequently, from the mechanical point of view, aluminum would seem to be the better choice as a material despite its lower Young's modulus. However, it is not yet clear which of the aluminum structures should be chosen for a real stack since it

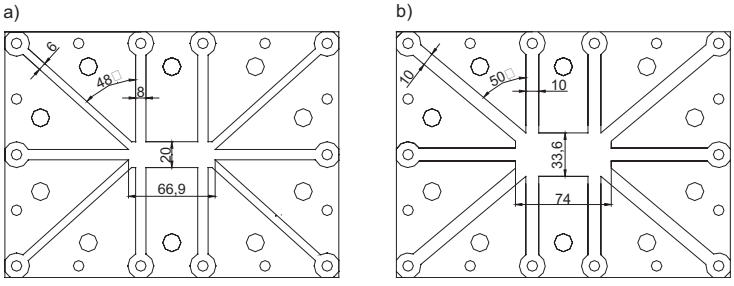

Fig. 6 A schematic of the ten-rib structures for (*a*) steel and (*b*) aluminum. The dimensions are in millimeters.

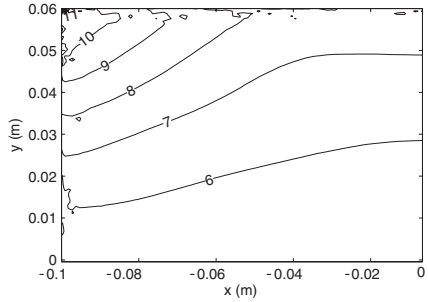

Fig. 8 The clamping pressure isobars on the GDL surface of the 7 cm aluminum rib structure with 1 kN load at each bolt. The pressure values are in bars.

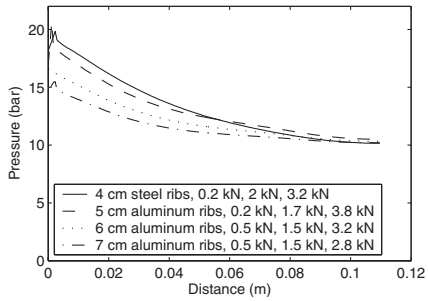

Fig. 9 The diagonal GDL pressure values of the structures with optimized bolt loads. The first load value refers to the corner bolt, the second to the bolts next to the corner, and the last to the bolts at the middle of the edges.

is not known whether there is any significant difference in the fuel cell performance if the GDL pressure distribution is 10–15 bars instead of 10–20 bars. If no difference can be experimentally observed, then the 0.7 kg lighter 5 cm high rib structure can be chosen instead of the 7 cm high structure. In large stacks that consist of many unit cells, the weight difference may be negligible, since the weight of the unit cells used in these experiments is approximately 0.9 kg and stacking 100 or more cells makes the reduction in end plate weight negligible. However, some mobile low voltage applications require stacks with only a few cells that have large areas. In these stacks, the rigidity of the end plates is crucial and the weight of the end plates becomes a significant factor.

5 Error Estimation

The effect of the mesh was studied with the flat plate model that usually had approximately 64,000 elements. This model was solved using three different meshes: 74,000, 80,000, and 95,000, and the pressure distributions were compared. The maximum differences in the GDL pressure values between the solutions given by the original mesh and larger meshes were below 1.5%. The relative errors are largest at the middle area of the cell, where the compression pressure is small. In order to check that each of the models presented in this work gives reliable results, each model was solved with two different meshes. The maximum differences between the solutions varied in the range of 1–3%, so the error induced by the mesh can be considered insignificant.

To further simplify the model, the flow-field plates, gasket layers, and metal nets were replaced with a single homogeneous component as described in Sec. 3. The value for the Young's modulus of this approximative component was taken as the value that resulted in a similar deformation of the homogenous component compared to that of the combined original components as determined with a separate model, i.e., 7.7 GPa. However, some error is likely introduced to the models because of this simplification. Therefore, the flat plate model was solved with two different Young's moduli, 5 GPa and 10 GPa, for the homogeneous component. The larger value, 10 GPa, corresponds to the Young's modulus of the flow-field plates. Despite the significant difference (over 30%) in the Young's modulus of the homogeneous plate, the

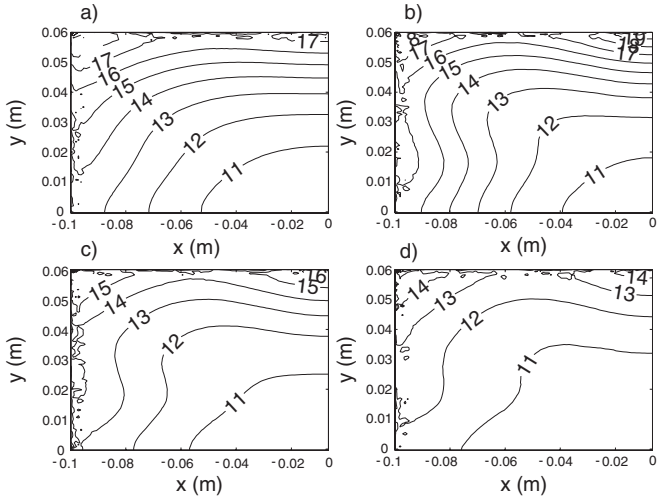

Fig. 10 Pressure isobars on the GDL: (*a*) 4 cm steel ribs, (*b*) 5 cm aluminum ribs, (*c*) 6 cm aluminum ribs, and (*d*) 7 cm aluminum ribs. The pressure values are in bars.

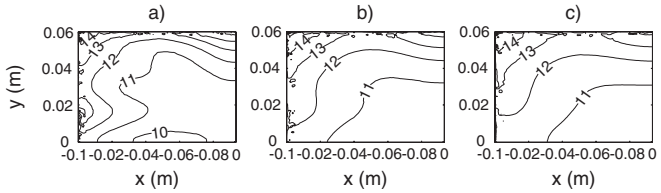

Fig. 11 The pressure isobars of the 7 cm aluminum ribs on the three GDL surfaces: (*a*) top (outermost), (*b*) middle, and (*c*) bottom (closest to *z*-symmetry boundary, i.e., middle of the stack)

compression values are close to similar. The relative differences are largest at the middle region of the cell where the pressure values are small at 7% with 10 GPa and 18% with 5 GPa data. Thus, it can be assumed that approximating the different components with a single homogeneous one should not give rise to an unacceptable source of error.

The models include other sources of inaccuracy besides the mesh and the reduced number of components discussed above. The material values for some of the components such as the flow-field plates and the GDL were only estimates of the real values. It is also probable that the Young's moduli for these components are, in fact, dependent on the stress in the material and not constant as assumed in the modeling. Also, several fine details of the cell structure were excluded to decrease the number of degrees of freedom. However, the stress and strain behavior of the stack is dominated by the end plates and their properties are known with good accuracy. The effect of the fine geometrical details is very local and uninteresting for end plate development. Furthermore, even though the compression data might not be exact, comparison of the data achieved with different end plates should still give valid information on which end plate structure is the most promising one.

6 Experiment

The modeling results were verified with experiments. Two of the modeled end plate structures, the original flat plate and the 5 cm rib aluminum plate, were manufactured and compared experimentally. Experiments were made with both a five-cell stack assembly and a unit cell assembly where the MEAs were replaced with a Pressurex® Super Low pressure-sensitive film. The advantage of the latter was that there was much less noise in the measurements, which will be discussed in more detail later in this section. It should be noted that neither of the experimental results corresponds exactly to the modeled situation (i.e., a six-cell stack), which was due to practical considerations of available materials. However, not only is there not much difference in practice between a five- and a six-cell stack, but also the essential point in these experiments is not to get the exact same pressure distributions as modeled but rather to be able to verify the advantageousness of the optimized structure in general. In addition, it was noticed in the experiments that quantitative validation was in any case impracticable with the available measurement accuracy, which is to be discussed in more detail later in this section.

Prior to the stack pressure measurements, the relationship between the color intensity of the film and the clamping pressure directed to the film was studied with calibration measurements. However, later experiments showed that despite the measurements being done in controlled ambient temperature and humidity, even the films corresponding to different cells in the stack had varying total color intensity levels, even though the pressure in each cell was definitely the same. A possible reason for this behavior is inhomogeneous quality of the pressure-sensitive film. Thus, the actual pressure values given as results of each measurement are not reliable. However, the differences in intensity, i.e., pressure, on each pressure-sensitive film, should not be strongly affected and thus results from different experiments can be compared to each other, not through the actual pressure but rather through the variation in pressure.

In each measurement, the stack was assembled with all components, excluding the MEAs, which were replaced with pressure-sensitive films. The metal net was replaced with Grafoil® because the thickness of the available metal net was significantly different from the surrounding Grafoil® gasket, which would have led to disturbances in the pressure distribution. The bolts were tightened gradually to avoid inhomogeneous compression on the stack at any time during the assembly. The compression in the assembled stack was let to stabilize. After disassembly, the pressure-sensitive films were scanned. The color intensity values were changed into pressure values by using the calibration data and compared to the average pressure measured by each film. Finally, the pressure data were averaged over the four symmetrical cell segments in order to minimize the effect of thickness variation in the stack components. The pressure values were also smoothed by local averaging so that the uninteresting effect of the channel structure was mostly lost and the pressure distributions became easier to compare to the modeling results.

The largest single source of error in these measurements was, however, the manufacturing tolerance of the different cell components, e.g., in flow-field plates the thickness variation was on average 0.1 mm and at maximum 0.15 mm. This error was to some extent mitigated by pairing off the flow-field plates so that the manufacturing defects in the two plates canceled each other out. Nevertheless, this method of increasing the accuracy was relatively unsophisticated and the measurement results clearly show the effect of the thickness variation. The noise from this effect was so significant that stack experiments with the optimized clamping pressures, which had been originally planned, were not performed at all since the pressure distribution measured with the optimized end plate was so uniform that any differences were almost inseparable from the noise. This is why the unit cell measurements were

Table 2 The masses and achieved pressure ranges of the different structures

Component	Mass (kg)	Mass/mass of flat plate (%)	Pressure range (bar)
4 cm steel ribs	6.5	92	10–20
5 cm aluminum ribs	3.0	42	10–20
6 cm aluminum ribs	3.4	47	10–17
7 cm aluminum ribs	3.7	52	10–15

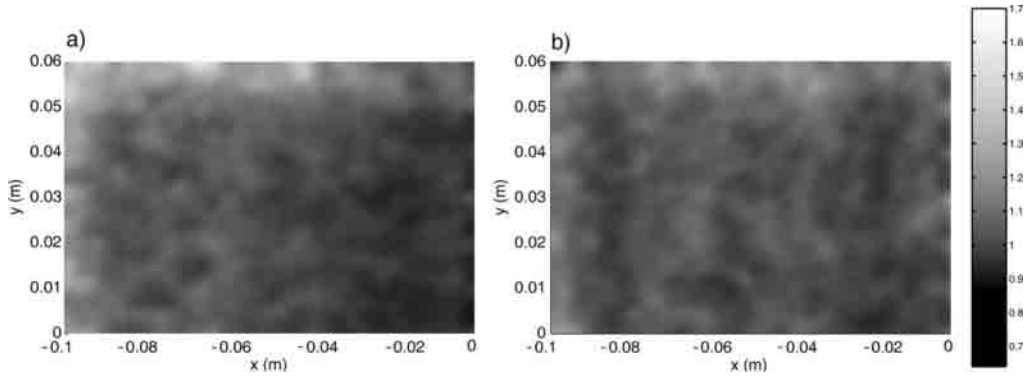

Fig. 12 The five-cell stack measurement results: (*a*) corresponds to the pressure on the middle cell in the stack with the original flat end plates and (*b*) to the 6 cm rib aluminum plates. The color bar values show the pressure value in relation to the average clamping pressure.

also performed; with far fewer components, there is also less noise present in the results and the improvement in the pressure distribution that can be had by using the optimized clamping pressures could be seen.

The results from the five-cell stack measurements are illustrated in Fig. 12. While in Fig. 12(*a*) the pressure is clearly smaller in the middle, as predicted by the modeling, in Fig. 12(*b*) the background noise is dominating the pressure distribution. The results from the single cell measurements are illustrated in Fig. 13. Here, the distorting noise is smaller and the pressure distribution is closer to the one predicted by the modeling. It should be noted that in Fig. 13(*a*), the pressure values in the lower right corner corresponding to the center of the cell are too large. This is due to the fact that the used pressure-sensitive film does not show pressures beneath 6.5 bars, which corresponds to the minimum relative pressures shown in these pictures. Taking this into consideration, it is clear that the pressure distribution measured with the 6 cm aluminum rib end plates is clearly more homogeneous than that of the original flat plate. With the single cell experiments, it was also possible to study the effect of using the optimized clamping pressures. The measurement results are shown in Fig. 13(*c*), where the pressure distribution is clearly more even than in the two other cases. The reason for the low pressure values on the right edge of the figures is the flow-field plate channel structure.

7 Summary and Discussion

The compression pressure distribution on the GDLs in a PEMFC stack was studied by modeling using the finite element method. The results show that the often used flat steel plate structure is not only heavy and thus impractical for many applications, but also clearly inferior in terms of the GDL pressure distribution to alternative structures such as a ribbed aluminum plate. Thus, even though aluminum has a lower Young's modulus than steel, it is nevertheless the better choice for an end plate in terms of the end plate mass since its density is also lower. The GDL compression pressure directly affects the electric and heat contact resistances between the GDL and the flow-field plates and the MEA as well as the GDL mass transport properties and consequently the GDL pressure distribution can be assumed to affect the performance and lifetime of the cell.

Using the aluminum rib structure with optimized clamping pressure at each bolt, it was possible to improve the 1–17 bar pressure distribution corresponding to the original flat plate to 10–15 bars with the aluminum rib structure. At the same time, the end plate mass was reduced to half of the original. It would seem that a pressure range of 10–15 bars or 20 bars is ideal so that the contact resistances are low enough while GDL is not compressed too heavily for the mass transport properties to suffer significantly.

In the modeling, all component materials were assumed to be elastic and the cell structure was simplified by reducing the number of components and excluding details such as the flow-field channel structure. As a result of these idealizations and the fact that in reality the stack components are not uniform in thickness due to manufacturing tolerances, the model results were not expected to exactly correspond to experimental data.

The improvement in the pressure distribution range is significant, since a compression in the range of a few bars as in the original case is so low that the contact resistances can be expected

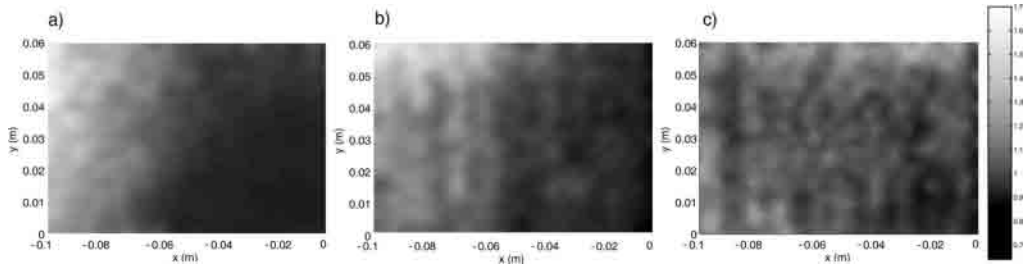

Fig. 13 The single cell measurement results: (*a*) original flat plates with homogeneous clamping, (*b*) 6 cm rib aluminum plates with homogeneous clamping, and (*c*) 6 cm rib aluminum plates with optimized clamping distribution. The color bar values show the pressure value in relation to the average clamping pressure.

to be too high for good performance. Experimental study of the modeled end plate structures did not show quite as much improvement, which was to large degree due to manufacturing defects, i.e., significant thickness variation in the cell components. However, in five-cell stack experiments, the aluminum rib structure proved to have a more even pressure distribution. In the stack experiments, the noise due to the thickness variations was so large that studying the effect of optimizing clamping pressure was not practicable. Consequently, this was studied with a single cell assembly, where the difference was easier to see and, as expected according to the modeling results, the pressure distribution was improved by optimizing the clamping pressure.

In a stack, the compression differences between end cells and middle cells are unavoidable. The more uneven pressure distribution in end cells can lead to reduced gas flows, which usually results in increased flooding. By using simulations, it can be estimated whether the difference between the middle cells and end cells will lead to major deviation in performance that can be called "end cell problem."

The experiments also showed that in many cases, inadequate tolerances in the thickness of the cell components can be a significant problem. In the experiments performed in this work, the flow-field plates were arranged so that the thickness variation was to some extent canceled. However, a random arrangement when components with low tolerances are used is likely to lead to a worse scenario, where the GDL compression is much larger on one side of the cell than on the other. Interestingly, the problem is quite different in a single cell assembly, where the problem is more that there is not enough noise to smooth the pressure distribution and thus the end plate design becomes more critical, which incidentally is quite the opposite to the usual phenomenon of problems increasing when moving from unit cells to stacks. It would also seem that structures, which work in single cells, may not work in stacks and vice versa.

Acknowledgment

The authors would like to thank the National Technology Agency TEKES and Academy of Finland for funding and VTT Technical Research Centre of Finland for providing flow-field plates for the experimental part of the work. The help and advice of D. Sc. Paavo Hassinen on structural mechanics are also gratefully acknowledged.

Nomenclature

- b = thickness (m)
- D = elasticity matrix (Pa)
- d = height (m)
- E = Young's modulus (Pa)
- I = coefficient of rigidity (m^4)
- $\mathbf{u}$ = deformation vector (m)
- u = x-directional deformation (m)
- v = y-directional deformation (m)
- w = z-directional deformation (m)

Greek Symbols

- γ_{ij} = shear strain in i,j-plane
- $\boldsymbol{\varepsilon}$ = strain tensor
- ε_i = i-directional normal strain
- υ = Poisson's ratio
- ρ = density ($kg\,m^{-3}$)
- $\boldsymbol{\sigma}$ = stress tensor (Pa)
- σ_i = i-directional normal stress (Pa)
- τ_{ij} = shear stress in i,j-plane (Pa)

References

[1] Ihonen, J., Mikkola, M., and Lindbergh, G., 2004, "Flooding of Gas Diffusion Backing in PEFCs," J. Electrochem. Soc., **151**(8), pp. A1152–A1161.
[2] Escribano, S., Blachot, J.-F., Ethève, J., Morin, A., and Mosdale, R., 2006, "Characterization of PEMFC Gas Diffusion Layer Properties," J. Power Sources, **156**(1), pp. 8–13.
[3] Lee, W., Ho, C.-H., Van Zee, J. W., and Murthy, M., 1999, "The Effects of Compression and Gas Diffusion Layers on the Performance of a PEM Fuel Cell," J. Power Sources, **84**(1), pp. 45–51.
[4] Evertz, J., and Günthart, M., 2003, "Structural Concepts for Lightweights and Cost-Effective end Plates for Fuel Cell Stacks," *Second European PEFC Forum*, Lucerne, Switzerland, Vol. 2, pp. 469–482.
[5] Lee, S.-J., Hsu, C.-D., and Huang, C.-H., 2005, "Analyses of the Fuel Cell Stack Assembly Pressure," J. Power Sources, **145**(2), pp. 353–361.
[6] Young, W. C., and Budynas, R. G., 2002, *Roark's Formulas for Stress and Strain*, 7th ed., McGraw-Hill, New York.
[7] Zienkiewicz, O. C., and Taylor, R. L., 2000, *Finite Element Method*, Vol. 1, 5th ed., Elsevier, New York.
[8] Ju, H., Meng, H., and Wang, C.-Y., 2005, "A Single-Phase, Non-Isothermal Model for PEM Fuel Cells," Int. J. Heat Mass Transfer, **48**(7), pp. 1303–1315.
[9] Grafoil data sheet at GrafTech, http://www.graftechaet.com/upload/GHA%20sheet%20properties.pdf, referred to on 26.10.2005.

PUBLICATION 5

Modeling free convective mass and heat transfer in fuel cells

Submitted to Journal of Fuel Cell Science and Technology.

Modeling Free Convective Mass and Heat Transfer in Fuel Cells

Suvi Karvonen
VTT Technical Research Centre of Finland
Biologinkuja 5, Espoo, P.O.Box 1000, FI-02044 VTT, Finland
Tel. +358 40 136 7774
suvi.karvonen@vtt.fi

Abstract
The polymer electrolyte fuel cell (PEMFC) is a possible power source for many applications ranging from portable electronics to distributed energy production. In portable electronics the competition is mainly with batteries and the fuel cell system must be small and light. Using free-breathing fuel cells that take their oxygen from the surrounding air reduces the required volume of auxiliary equipment. However, managing the free convection induced mass and heat transfer is difficult and by necessity relies on passive methods and cell design. This work focuses on modeling heat and mass transfer on the cathode of a free-breathing fuel cell. A comparison of two- and three-dimensional models demonstrates that two-dimensional models do not give reliable results on the heat and mass transfer of such cells. The results also show that some earlier modeling efforts have been made using unnecessarily complicated or incorrect boundary conditions.

Nomenclature

Symbol	Quantity	Value/unit
c	concentration	mol/m^3
c_p	thermal capacity	J/kgK
D	binary diffusion coefficient	m^2/s
$\tilde{D}$	Maxwell-Stefan diffusion coefficient	m^2/s
E	energy	J
F	Faraday constant	96485 C/mol
$\mathbf{g}$	gravity vector	m/s^2
i	current density	A/ m^2
$\mathbf{j}$	molar flux vector	mol/m^2s
k	heat conductivity	J/m^2
M	molar mass	kg/mol
$\mathbf{n}$	normal vector	-
$\dot{\mathbf{N}}$	molar flux on electrode boundary	kg/m^2s
p	pressure	Pa
R	gas constant	8.314 J/molK
T	temperature	K
$\mathbf{t}$	tangential vector	-
q	thermal flux	W/m^2
$\mathbf{u}$	velocity vector	m/s
x	molar fraction	-
z	number of electrons involved in a reaction	-

Greek symbols

α	water transport number	-
ε	porosity	-
ρ	density	kg/m^3
κ	permeability	m^2
ω	mass fraction	-
η	dynamic viscosity	Pa s

1 Introduction

The polymer electrolyte membrane fuel cell (PEMFC) is a low temperature, small-scale fuel cell with a solid, proton conducting electrolyte membrane. PEM fuel cells could be used as a power source in portable electronics where they offer advantages over traditional batteries such as no need for recharging time and potentially more power density. However, before large-scale commercialization can take place, problems concerning the storage of the hydrogen fuel, reliability and life-time of the cell will have to be solved. The power density and efficiency of the fuel cell are also critical in terms of possible commercialization. In free-breathing fuel cells these attributes are strongly dependant on the effectiveness of the passive mass and heat transfer to ambient air.

A fuel cell system designed for use in portable electronics should be as compact as possible in order to minimize necessary auxiliary equipment. In a free-breathing fuel cell free convection in ambient air takes care of the heat and mass transfer on the cathode side of the cell. Free convection (a.k.a. natural convection) is caused by density variations in air resulting from temperature and concentration gradients generated by the operating fuel cell. Of these two, the temperature effect is usually more significant. The size, geometrical design and tilt angle of the fuel cell all affect the free convection phenomenon.

In this work, the mass and heat transfer driven by free convection was studied on the cathode to gain an understanding of how this effect should be modeled and how the different geometrical and operating parameters affect the heat and mass transfer. It should be noted that the model developed here is an example of a worst-case scenario in the sense that the ambient air is still and all movement is caused by natural convection, which is usually not the case. In reality, heat and mass transfer fluctuate according to wind or drafts and other disturbances as shown in e.g. [1].

The model consists of the cathode of a fuel cell and an ambient air zone surrounding the cathode. This corresponds to a fuel cell set in a larger portable application where the convection flow is blocked on one side by the device itself. Several simplifications were made in the modeling due to practical necessity. Only the cathode gas diffusion layer is included as a modeling domain and the cathode overpotential is taken as a constant across the active area. This is due to the fact that modeling the free convection in the ambient air requires a lot of computational capacity, and thus adding small-scale details such as the MEA would make the model computationally heavy. The product water of the cell reactions was assumed to be gaseous, i.e. two-phase flow conditions were not considered in this work. This decision was made partially due to necessity, since two-phase equations are complicated to solve, but mostly because of the fact that of the various required two-phase parameters, only a few have been properly either measured or theoretically derived. Most two-phase parameters derive from experiments made on sand or soil samples and using these values and correlations for a fibrous, partially hydrophobic material such as the GDL is questionable. However, should satisfactory values for the two-phase parameters be discovered, the results of this work apply also to making a two-phase model of a free-breathing fuel cell.

The aim of this work was to develop a good model of a free breathing fuel cell by comparing different approaches to modeling such cells. Here the focus is more on the free convection phenomenon and less on internal cell operation, thus complementing studies such as [2]. Different boundary conditions were studied to find the optimal one in 2D. Based on these results, a 3D model was built and its results were compared to those of the 2D models. This was done to evaluate whether 2D modeling of free-breathing fuel cells is reliable since it offers many advantages over 3D

models and has been used before, e.g. in [3]. The results show that some 3D models such as presented in [4] can be improved in terms of accuracy and computational efficiency by using different boundary conditions.

2 Theory

The models are divided into subdomains that include the ambient air zone, the cathode gas diffusion layer and the current collector ribs, the latter of which have to be excluded in the 2D model. The modeling domain is illustrated in Fig. 1. The area of the cell is 1 cm^2. The cathode catalyst layer is assumed to be an infinitely thin layer on the gas diffusion layer boundary. The size of the ambient air zone was chosen so that further increase in size no longer affected the results since if the zone is too small there is a risk of the natural convection mass transfer becoming more efficient than in reality.

The gas flow, species (nitrogen, oxygen and water) concentrations and temperature are modeled using the Navier-Stokes equations (in the ambient free convection zone), Darcy's Law (in the gas diffusion layer), continuity equation, Maxwell-Stefan diffusion and convection equation and the energy equation. The product water of the cell is assumed to be gaseous. This is typically not the case in a PEM fuel cell, but serves here as a first approximation. The authors are working on implementing a three-dimensional model that takes into account liquid water.

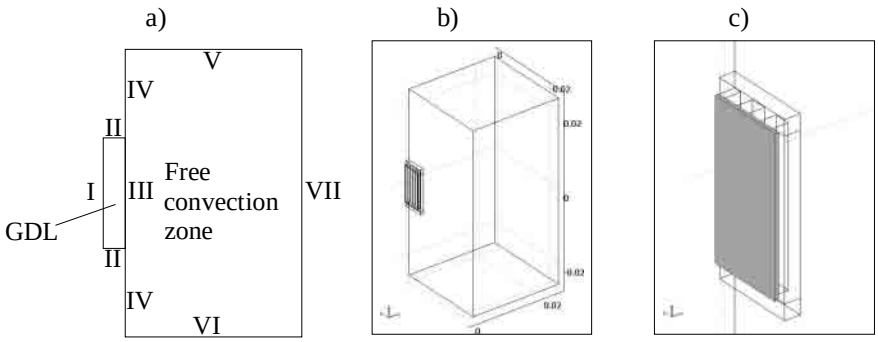

Figure 1. A schematic of the modeling domain in a) 2D (not in scale), b) 3D and c) the cathode GDL and current collector ribs enlarged in 3D. The shaded area in c) corresponds to the cathode GDL.

The equations used in the different modeling domains are standard electrochemical and mass transport equations used in fuel cell modeling with the effect of free convection derived buoyancy included.

Mass, momentum and energy transport:

$$-\rho\mathbf{u}\cdot\nabla\mathbf{u}+\rho\,\mathbf{g}-\nabla p+\nabla\cdot\left(\eta(\nabla\mathbf{u}+\nabla\mathbf{u}^{\mathrm{T}})\right)=0 \quad (1)$$

$$\nabla\cdot\left(\rho\frac{\eta}{\kappa}\nabla p\right)=0 \quad (2)$$

$$\nabla\cdot(\rho\,\mathbf{u})=0 \quad (3)$$

$$\nabla\cdot(k\nabla T)=c_p\rho\,\mathbf{u}\cdot\nabla T \quad (4)$$

The use of the Navier-Stokes equations (1) to model flow is acceptable with laminar flow (Reynolds number below 2000). For the Darcy equation (2), the Reynolds number has to be below 1. The first condition is satisfied in the whole modeling domain and the latter in the GDL. Consequently, Eq. (1) is used in the ambient air zone and Eq. (2) in the GDL. In the current collector ribs only energy transport is modeled.

Multicomponent diffusion equations (Maxwell-Stefan equations) were used to model diffusion in the model:

$$\nabla \cdot (\mathbf{j}_i + \rho \omega_i \mathbf{u}) = 0, \qquad i = \mathrm{O}_2, \mathrm{H}_2\mathrm{O}, \mathrm{N}_2 \tag{5}$$

$$\mathbf{j}_i = -\rho \omega_i \sum_{j=O_2,H_2O,N_2} \tilde{D}_{ij} \left(\nabla x_j\right), \tag{6}$$

$$\nabla x_j = \frac{M^2}{M_j} \sum_{\substack{j=O_2,H_2O,N_2 \\ k \neq j}} \left(\frac{1}{M} + \omega_k \left(\frac{1}{M_k} - \frac{1}{M_j} \right) \right) \nabla \omega_k \tag{7}$$

It should be noted that only two of the three (for oxygen, nitrogen and water) Maxwell-Stefan equations (5) have to be solved because the mass fraction of one species can be calculated from the other mass fractions since the sum of the mass fractions always has to equal one. Consequently, the mass fraction of nitrogen was calculated from those of oxygen and water, i.e. $\omega_{\mathrm{N}_2} = 1 - \omega_{\mathrm{O}_2} - \omega_{\mathrm{H}_2O}$. The Maxwell-Stefan diffusion coefficients $\tilde{D}_{ij}$ in the mass-averaged velocity frame are calculated from the binary diffusion coefficients D_{ij}, which were calculated with Equations (8) and (9) [5], as discussed in [6]. This calculation is equivalent with another formulation used in some articles, see e.g. [7].

$$D_{ij} = C \frac{T^{1.75} \sqrt{1/M_i + 1/M_j}}{p\left((v_i)^{1.3} + (v_j)^{1.3}\right)^2}, \text{ where } C \text{ is a constant (see Table (1)).} \tag{8}$$

The driving force for free convection is the density difference in air caused by temperature and composition differences. The temperature dependency of the density of air is calculated according to the ideal gas law:

$$\rho = -\frac{pM}{RT}, \qquad M = M_{\mathrm{N}_2} x_{\mathrm{N}_2} + M_{\mathrm{O}_2} x_{\mathrm{O}_2} + M_{\mathrm{H}_2O} x_{\mathrm{H}_2O} \tag{9}$$

Boundary Conditions

The boundaries of the 2D model are marked in Fig. 1 a). The 3D model has also thermally conductive current collectors. On the current collector boundaries, the temperature and its derivate are continuous and all the other fluxes are zero. The other boundaries are defined with appropriate boundary conditions listed in the following section.

Boundary I: the cathode catalyst layer. Oxygen is consumed and water and heat are generated on this boundary. Since the mass flux of generated water is not equal to the mass flux of consumed oxygen, there is total nonzero velocity across this boundary.

$$\rho \frac{\eta}{\kappa} \mathbf{n} \cdot \nabla p = (\dot{\mathbf{N}}_{O2} + \dot{\mathbf{N}}_{H2O}) / \varepsilon \rho \tag{10}$$

$$\mathbf{n} \cdot (\mathbf{j}_{H2O} + \rho \omega_{H2O} \mathbf{u}) = \dot{\mathbf{N}}_{H2O} \tag{11}$$

$$\mathbf{n}\cdot(\mathbf{j}_{O2}+\rho\omega_{O2}\mathbf{u})=\dot{\mathbf{N}}_{O2} \tag{12}$$

$$\mathbf{n}\cdot k\nabla T=c_p\rho\,\mathbf{u}\cdot\nabla T+q_0 \tag{13}$$

where $\dot{\mathbf{N}}_{O2}=\frac{i}{4F}M_{O2}$, $\dot{\mathbf{N}}_{H2O}=-\frac{i}{2F}M_{H2O}$ and $q_0=i\left(\eta+\frac{326T}{4F}\right)\cdot 0.8$ (the multiplier 0.8 follows from the assumption that 80 % of the generated heat is conducted out of the cell through the cathode side free convection).

The current density i on the catalyst layer boundary is calculated from the Butler-Volmer equation (14) and depends on the temperature and the mass fraction of oxygen on the catalyst boundary. The cathode overpotential is assumed constant. The water transfer coefficient α is 0.5.

$$i=i_0\frac{c_{O_2}}{c_{O_2}^0}\left(\exp\left(\frac{\alpha\,zF}{RT}\eta_c\right)-\exp\left(\frac{-(1-\alpha)zF}{RT}\eta_c\right)\right) \tag{14}$$

where i_0 is the temperature dependent cathode exchange current density calculated from [8]

$$i_0(T)=i_0(T_0)\exp\left(-\frac{\Delta E}{R}\left(\frac{1}{T}-\frac{1}{T_0}\right)\right) \tag{15}$$

where ΔE = 27 kJ/mol as discussed in [8].

Boundary II: Insulated GDL boundaries. There is no mass, heat or species transport across these boundaries.

$$\rho\frac{\eta}{\kappa}\mathbf{n}\cdot\nabla p=0 \tag{16}$$

$$\mathbf{n}\cdot(\mathbf{j}_i+\rho\omega_i\mathbf{u})=\mathbf{n}\cdot\mathbf{j}_i=0 \tag{17}$$

$$\mathbf{n}\cdot k\nabla T=c_p\rho\,\mathbf{u}\cdot\nabla T \tag{18}$$

Boundary III: Boundary between the GDL and the free convection zone. The momentum equation changes between Darcy's law and Navier-Stokes Equations. The effect of GDL porosity is taken into account as the difference (the multiplier ε) between the velocities in the gas diffusion layer and the free convection zone.

ω_{O_2}, ω_{H_2O}, and T are continuous across the boundary

$$\mathbf{u}_{Navier-Stokes}=\varepsilon\rho\frac{\eta}{\kappa}\mathbf{n}\cdot\nabla p_{Darcy} \tag{19}$$

$$p_{Navier-Stokes}=p_{Darcy} \tag{20}$$

Boundary IV: Insulated boundaries of the free convection zone.

$$\mathbf{u}=0 \tag{21}$$

$$\mathbf{n}\cdot(\mathbf{j}_i+\rho\omega_i\mathbf{u})=\mathbf{n}\cdot\mathbf{j}_i=0 \tag{22}$$

$$\mathbf{n}\cdot k\nabla T=c_p\rho\,\mathbf{u}\cdot\nabla T \tag{23}$$

Boundaries V, VI and VII: Free convection zone boundaries.

$$\mathbf{t}\cdot\mathbf{u}=0 \tag{24}$$

$$\mathbf{n}\cdot(\mathbf{j}_i+\rho\omega_i\mathbf{u})=\mathbf{n}\cdot\mathbf{u}\omega_i \text{ (Boundary V)} \tag{25}$$

$$\omega_{O_2}=\omega_{O_2}^0,\ \omega_{H_2O}=\omega_{H_2O}^0 \text{ (Boundaries VI and VII)} \tag{26}$$

$$T=T_0 \qquad \text{(Boundary VII)} \tag{27}$$

Alternative boundary conditions have also been used on these boundaries, see e.g. [8, 9]:

$$\mathbf{u} = 0 \tag{28}$$

$$\omega_{O_2} = \omega_{O_2}^0 \,,\ \omega_{H_2O} = \omega_{H_2O}^0 \text{ (Boundaries VI and VII)} \tag{29}$$

$$T = T_0 \qquad \text{(Boundary VII)} \tag{30}$$

In short, with the alternative boundary conditions the gas velocity is fixed to zero and temperature and mass fractions are fixed to those of ambient air on the outer boundaries of the free convection zone. Thus for the air flow the boundaries are "closed". The problem with this formulation is that a much larger modeling domain is required and the resulting free convection vortex can be problematic for the solver and typically more computing capacity is required since a finer mesh is necessary throughout the whole free convection zone. Both types of boundary conditions have been used in free convection modeling: for "open" boundaries, see e.g. [10] and for "closed" e.g. [9].

The governing equations (1-5) were solved with commercial finite element software, Comsol Multiphysics®. Depending on the cell dimensions, the models had 5000-10 000 elements, which corresponds to 60 000-120 000 degrees of freedom. The calculations were performed over a 64-bit client-server connection. The server computer had 12 Gb RAM and 40 Gb of swap-space. The operating system was SuSe 9.1 AMD64 Linux. The solution time with this hardware was from less than half an hour to a few hours.

3 Results

Quantities such as current density, temperature and mass fractions of water and oxygen were studied in the solved models. The aim was to find out how they vary between the 2D and 3D models and how changing the ambient air boundary conditions from open to closed affects these variables. This information allows for building a computationally efficient but still accurate model of a free-breathing fuel cell.

2D model and Boundary Conditions

Comparison of the results of 2D models with differently sized ambient air zones showed that the modeling domain has to be larger in the case of the closed boundary settings than with open, since otherwise the mass and heat transfer in the ambient zone will be overestimated. This causes the closed boundary settings to require more computing capacity. A sufficient distance for the boundaries from the fuel cell for both boundary settings was determined by enlarging the area until there was no significant difference resulting from further changes. The difference between the open and closed boundary conditions is shown in Fig. 2 and Fig. 3. The two flow fields are very different as a whole, but give similar results close to the cell.

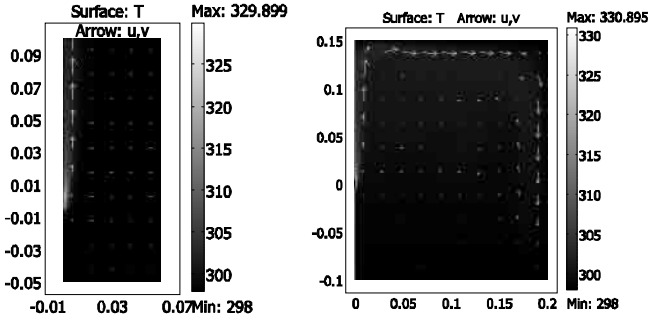

Figure 2. The flow fields and temperature distribution in the 2D models with a) open and b) closed boundary settings.

Comparison of the key parameters such as the current density and temperature of the cell show that with sufficiently large modeling domains, the differences between the two models are minute, less than 0.5 % for the current density and approximately 1 K for temperature. For the mass fractions, the differences are even smaller. In short, the closed boundary settings lead to slightly less efficient heat and mass transfer, presumably because the air velocity is a slower due to the zero-velocity boundaries. However, these differences are negligible. Thus both alternatives are suitable for modeling free convection. Using closed boundary conditions requires considerably more computing capacity and is thus impractical, especially for application in the 3D model. Based on these results the 3D model was implemented with the open boundary conditions.

3D model

The 2D model by necessity assumes a semi-infinite fuel cell with no cathode cover structures. The 3D model corresponds more accurately to reality since the width of the cell is limited and the current collector ribs are included. A similar model has been published in [2], however, the 2D modeling results of this work showed that the ambient air zone must large compared to the size of the cell and it is probable that this model overestimates the efficiency of natural convection.

As can be seen from results for current density, temperature and mass fractions illustrated in Fig. 3, there are significant differences between the two models. The current collector ribs affect the results in two ways: they hinder mass transfer as the gas flow cannot pass the solid ribs and improve the heat removal from the GDL. The latter is a consequence of the good thermal conductivity of the current collector which conducts the heat on to the current collector surface which is larger than the GDL surface and thus has better heat removal by natural convection.

The mass fractions on the catalyst layer do not differ much between the two models. The weaker mass transfer in the 3D model decreases the oxygen fraction and increases the water fraction in comparison to the 2D model. With oxygen, the change is negligible, in the order of 1 %, but with water vapor, the difference is above 10 %, which is large enough to strongly affect whether the cell is flooding or not. However, the most important differences are observed with the temperature and current density values. The ribs improve heat transfer and thus the temperature of the cell is 6 - 8 K lower in the 3D model. This is also reflected in current density according to Equations (12 and 13), which increases the current density for the 3D model. Thus a 2D model predicts higher temperatures and lower current densities than realistic since the ribs are excluded. It should also be noted that the lower temperature and higher water mass fraction in the 3D model both suggest that the 2D model can not be reliably used to predict flooding.

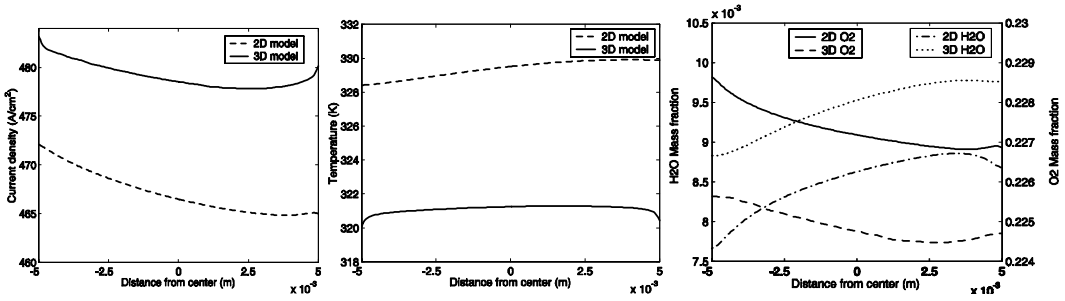

Figure 3. The a) current density, b) temperature, c) water and oxygen mass fractions on the catalyst layer. In the 2D model, the values are taken on the catalyst layer boundary and in the 3D model on the symmetry edge of the GDL catalyst layer surface (corresponding to a vertical middle line on the boundary). The left side corresponds to the bottom of the cell and the right side to the top.

The 3D model was also used for preliminary tests on the effect of cell size and tilt angle to the cell performance. Doubling the cell dimensions, i.e. quadrupling the area did not have a significant effect on the cell performance. This indicates that the cell size is small enough that free convection can provide sufficient reactants to the whole cell area.

4 Summary and Conclusions

Modeling is one approach to understanding the complex phenomena associated with free-breathing fuel cells. In this work, a model of a free-breathing fuel cell was developed in both two and three dimensions. The 2D model was used to optimize boundary settings and its results were used for building the 3D model. This model was used to study the natural convection phenomenon in the cathode of a free-breathing fuel cell and air surrounding the cell.

Comparing the results of the 2D and 3D models shows that 2D free-breathing fuel cell models can not, in general, be expected to give reliable data since heat and mass transfer efficiency is overestimated. This error is largely due to the fact that in 2D models the current collector ribs and any other support structures must be excluded and thus the 2D models give overly optimistic results for mass transfer while heat transfer is underestimated as the heat conduction through the ribs is absent.

Testing the boundary conditions with the 2D model showed that the two boundary condition settings gave similar results but one, the “closed” boundary conditions approach, required much more computing capacity. The similarity of the results suggested that both were applicable for modeling purposes, and thus the computationally less demanding “open” boundary settings were used in 3D modeling. It should be noted that other models of free-breathing fuel cells have typically used closed boundary settings, which makes them unnecessarily heavy.

The 3D model created in this work is computationally relatively light and can be used to study the effects of tilt angle, size and geometry to the cell performance. This is a subject for future work along with adding two-phase equations to the model.

References

[1] Tibor Fabian, Jonathan D. Posner, Ryan O'Hayre, Suk-Won Cha, John K. Eaton, Fritz B. Prinz and Juan G. Santiago: The role of ambient conditions on the performance of a planar, air-breathing hydrogen PEM fuel cell, J. Power Sources Volume 161, Issue 1 , (2006), Pages 168-182

[2] J. J. Hwang, W. R. Chang, C. H. Chao, F. B. Weng, and A. Su, Mass Transports in an Air-Breathing Cathode of a Proton Exchange Membrane Fuel Cell, J. Fuel Cell Sci. Technol. 6, 041003 (2009)

[3] S. Litster, J.G. Pharoah, G. McLeana and N. Djilali: Computational analysis of heat and mass transfer in micro-structured PEMFC cathode, Journal of Power Sources Volume 156, Issue 2, Pages 334-344 (2006)

[4] P. Manoj Kumar and Ajit Kumar Kolar**,** Effect of cathode design on the performance of an air-breathing PEM fuel cell, International Journal of Hydrogen Energy, Article in Press (2009)

[5] Taylor, Ross and Krishna, R.: Multicomponent Mass Transfer, John Wiley & Sons, Inc. (1993)

[6] C. F. Curtiss and R. Byron Bird: Multicomponent Diffusion, Ind. Eng. Chem. Res 38, 2525-2522, (1999)

[7] E. Birgersson, M. Noponen and M. Vynnycky: Analysis of a Two-Phase Non-Isothermal Model for a PEFC, J. Electrochem. Soc., Vol. 152, No. 5, pp. A1021–A1034 (2005).

[8] Wei Sun, Brant A. Peppley and Kunal Karana: An improved two-dimensional agglomerate cathode model to study the influence of catalyst layer structural parameters, Electrochimica Acta, Volume 50, Issues 16-17, Pages 3359-3374 (2005)

[9] S. Pretot, B. Zeghmati and G. Le Palec: Theoretical and experimental study of natural convection on a horizontal plate, Applied Thermal Engineering Volume 20, Issue 10, Pages 873-891 (2000)

[10] M. Havet and D. Blay: Natural convection over a non-isothermal vertical plate Int. J. Heat and Mass Transfer Volume 42, Issue 16, Pages 3103-3112 (1999)

Appendix

List of various constant and modeling parameters

Name	Symbol	Value
Dynamic viscosity	η	$1.81034 \cdot 10^{-5}$ Pa·s
Gravitational acceleration	g	9.81 m/s^2
Specific heat capacity of air	c_p	1005.38007 J/kg K
Ambient temperature	T_0	298 K
Universal gas constant	R	8.314 J/mol K
Ambient pressure	p_0	10^5 Pa
Heat conductivity of air	k	0.026044 J/m^2
Oxygen concentration in ambient air	$c_{O2,0}$	8.39128 mol/m^3
Water concentration in ambient air	c_{H2O0}	0.403621 mol/m^3
Faraday's constant	F	96485 C/mol
Molar mass of nitrogen	M_{N2}	0.0282 kg/mol
Molar mass of oxygen	M_{O2}	0.032 kg/mol
Molar mass of water	M_{H2O}	0.018 kg/mol
Effective heat conductivity of the GDL	k_{GDL}	0.3 W/m^2
GDL permeability	κ	$2.06 \cdot 10^{-12}$ m^2
Exchange current density	$i_0(T_0)$	0.01 A/m^2
Activation overpotential	η_c	0.6 V
GDL porosity	ep	0.5
Water transfer coefficient	α	0.5
Heat conductivity of the current collector	k_{cc}	14 J/m^2
Specific heat capacity of the current collector	c_{cc}	1000 J/kg K
Diffusion coefficient constant	C	$3.16 \cdot 10^{-8}$
Diffusion volume for oxygen	v_{O2}	$16.6 \cdot 10^{-6}$ m^3/mol
Diffusion volume for nitrogen	v_{N2}	$12.7 \cdot 10^{-6}$ m^3/mol
Diffusion volume for water	v_{H2O}	$17.9 \cdot 10^{-6}$ m^3/mol

Series title, number and
report code of publication

VTT Publications 772
VTT-PUBS-772

Author(s)
Suvi Karvonen

Title

Modelling approaches to mass transfer and compression effects in polymer electrolyte fuel cells

Abstract

The subject of the thesis is modelling polymer electrolyte membrane fuel cells (PEMFCs) locally and on a cell scale. The modelling was done using software based on the finite element method and focused on mass transfer issues and compression pressure distribution and its effects on local phenomena.

Mass transfer, more specifically the flow distribution in the flow field system, was studied on the cathode. The velocity distribution was improved by changing the geometry of the channel system. This improvement was also observed experimentally. Mass transport problems of free-breathing fuel cells were also studied. These cells rely on free convection to provide reactants and remove reaction products. In this thesis, the aim was to develop an accurate model that is also computationally light.

The compression distribution in a stack was modelled based on an existing stack design. The results showed poor internal pressure distribution, with most of the cell experiencing insufficient compression. The modelling was then used to find a better end plate structure and suitable torques for the nut and bolt assemblies. The results were validated experimentally.

The effect of compression was studied on a local scale on which compression variations caused by the channel structure had been seen to affect the gas diffusion layer properties and contact resistances between components. According to the modelling results, there are strong local transversal electric currents in the cell. This phenomenon can affect the cell performance and lifetime negatively.

ISBN
978-951-38-7754-5 (soft back ed.)
978-951-38-7755-2 (URL: http://www.vtt.fi/publications/index.jsp)

Series title and ISSN	Project number
VTT Publications 1235-0621 (soft back ed.) 1455-0849 (URL: http://www.vtt.fi/publications/index.jsp)	

Date	Language	Pages
October 2011	English, Finnish abstr.	73 p. + app. 66 p.

Name of project	Commissioned by

Keywords	Publisher
PEMFC, fuel cell, modelling	VTT Technical Research Centre of Finland P.O. Box 1000, FI-02044 VTT, Finland Phone internat. +358 20 722 4520 Fax +358 20 722 4374

Julkaisun sarja, numero ja raporttikoodi

VTT Publications 772
VTT-PUBS-772

Tekijä(t)
Suvi Karvonen

Nimeke

Polymeerielektrolyyttipolttokennojen massansiirron ja puristuspaineen vaikutusten mallintaminen

Tiivistelmä

Väitöskirja käsittelee polymeerielektrolyyttipolttokennon (PEMFC) toiminnan mallinnusta paikallisesti ja kennotasolla. Tutkimuksen työkaluna on käytetty mallinnusta elementtimenetelmään perustuvalla ohjelmistolla. Mallinnuksen painopisteinä ovat erityisesti aineensiirron ongelmat ja puristuspaineen jakautuminen ja vaikutus kennon paikalliseen toimintaan.

Aineensiirtoa eli virtauskanaviston toimintaa tarkasteltiin kennon katodilla mallintamalla kanavistoon syntyvää virtausprofiilia. Kanaviston geometriaa muuttamalla pystyttiin parantamaan virtausprofiilia, ja tämä mallinnuksen avulla suoritettu optimointi havaittiin myös kokeellisesti. Aineensiirron kysymyksiä tutkittiin myös vapaasti hengittävien polttokennojen kohdalla. Näissä kennoissa aineensiirto perustuu vapaaseen konvektioon. Työssä pyrittiin kehittämään yhtä aikaa luotettava ja laskennallisesti kevyt malli. Lopputuloksena syntyi kolmiulotteinen malli vapaasti hengittävästä kennosta, jolla tutkittiin kennon koon ja asennon vaikutusta toimintaan.

Kennostossa vallitsevaa puristuspainetta mallinnettiin olemassa olevaan kennostoon perustuvan mekaanisen mallin avulla. Tuloksena saatiin epätasainen painejakauma. Mallinnuksen avulla etsittiin parempi rakenne kennoston päätylevyille sekä muutettiin pulttien vääntömomentteja, jolloin kennolla vallitseva painejakauma saatiin pysymään toivotuissa rajoissa. Samalla päätylevyn painoa saatiin vähennettyä. Tulokset verifioitiin kokeellisesti.

Puristuspaineen vaikutusta tutkittiin paikallisella tasolla, jossa virtauskanaviston rakenteen aiheuttamien painevaihteluiden oli todettu vaikuttavan merkittävästi kaasudiffuusiokerrosten ominaisuuksiin ja komponenttien välisiin resistansseihin. Mallinnuksen tulosten mukaan kennossa syntyy paikallisesti merkittävästi poikittaissuuntaista sähkövirtaa, joka aiheuttaa virrantiheyteen vaihteluja. Ilmiö voi vaikuttaa negatiivisesti kennon toimintaan ja elinikään.

ISBN
978-951-38-7754-5 (nid.)
978-951-38-7755-2 (URL: http://www.vtt.fi/publications/index.jsp)

Avainnimeke ja ISSN	Projektinumero
VTT Publications 1235-0621 (nid.) 1455-0849 (URL: http://www.vtt.fi/publications/index.jsp)	

Julkaisuaika	Kieli	Sivuja
Lokakuu 2011	Suomi, engl. tiiv.	73 s. + liitt. 66 s.

Projektin nimi	Toimeksiantaja(t)

Avainsanat	Julkaisija
PEMFC, fuel cell, modelling	VTT PL 1000, 02044 VTT Puh. 020 722 4520 Faksi 020 722 4374

The subject of this thesis is modelling polymer electrolyte membrane fuel cells (PEMFCs), with the focus on mass transfer and compression pressure distribution issues. Good understanding of these subjects is necessary for improving PEMFC lifetime and performance and eventually making them viable for wide scale commercial applications.

Mass transfer on the cathode was shown to be improved by certain changes to the geometry of the channel system and also studied in the case of a free-breathing fuel cell. A similar improvement was found concerning the compression distribution through making changes to geometry and torques. The effect of compression was also studied on a local scale, showing how the channel structure causing uneven contact resistances can lead to unexpected local current distributions.

ISBN 978-951-38-7754-5 (soft back ed.)
ISSN 1235-0621 (soft back ed.)

ISBN 978-951-38-7755-2 (URL: http://www.vtt.fi/publications/index.jsp)
ISSN 1455-0849 (URL: http://www.vtt.fi/publications/index.jsp)